

University of Warwick institutional repository: <http://go.warwick.ac.uk/wrap>

A Thesis Submitted for the Degree of PhD at the University of Warwick

<http://go.warwick.ac.uk/wrap/57508>

This thesis is made available online and is protected by original copyright.

Please scroll down to view the document itself.

Please refer to the repository record for this item for information to help you to cite it. Our policy information is available from the repository home page.

Theory of the Charge Recombination Reaction Rate in Dye Sensitised Solar Cells

Emanuele Maggio

*A thesis submitted in partial fulfilment of the requirements for the
Degree of Doctor of Philosophy in Theoretical Chemistry*

Department of Chemistry and Centre for Scientific Computing
The University of Warwick

September 2013

Contents

List of Figures.....	v
Acknowledgements.....	vii
Abstract.....	ix
List of abbreviations and symbols	x
Chapter 1: Introduction	1
1.1 Overview	1
1.2 Experimental techniques	7
1.3 Standard computational chemistry methods	9
1.4 Charge carrier dynamics simulations.....	10
1.5 Remarks on charge transfer	14
1.6 Thesis outline	16
Chapter 2: Theory of the charge recombination rate at the semiconductor- molecule interface.....	17
2.1 Introduction.....	17
2.2 General expression for the charge recombination reaction rate.....	18
2.3 The Franck-Condon term in the semiclassical limit at high T.....	23
2.4 Bridge mediated semiconductor-dye electronic coupling.....	27
2.5 Conclusions.....	34
2.6 Appendix.....	34
Chapter 3: Evaluating charge recombination rate to dye⁺ from DFT calculations.....	39
3.1 Introduction.....	39
3.2 Theoretical background	40
3.2.1 Outline of charge transfer theory used in this chapter	41
3.2.2 Limits of validity and relevance of the theoretical model	42
3.2.3 Computational evaluation of the relevant quantities	44
3.3 Results and discussion	56
3.3.1 NKX series of dyes	56
3.3.2 OH family of dyes.....	61
3.3.3 Effect of uncertainties in the computational parameters on recombination lifetimes	68
3.4 Conclusions.....	71
Chapter 4: Charge recombination at the TiO₂-electrolyte interface.....	75
4.1 Introduction.....	75
4.1.1 Review of experimental and theoretical studies	75
4.2 Methodology	78
4.2.1 Reorganisation energy	78
4.2.2 Spectral density	80
4.2.3 Driving force and Franck-Condon term.....	81
4.2.4 Computational details	83

4.2.5	Energy alignment between molecular adsorbate and TiO ₂ band structure	85
4.3	Results.....	86
4.3.1	Charge recombination in the dark	90
4.3.2	Charge recombination under illumination	93
4.4	Conclusions.....	97
Chapter 5: Impact of defects on the CRR at the semiconductor-adsorbate interface.....		99
5.1	Introduction.....	99
5.2	Methodology	102
5.2.1	Model system	102
5.2.2	Model parameters.....	105
5.3	Results.....	109
5.3.1	Effect of the redox potential and reorganisation energy	109
5.3.2	Defect characterisation.....	112
5.3.3	Charge recombination for a slab with a surface bias	116
5.4	Conclusions.....	119
Chapter 6: Using orbital symmetry to minimise charge recombination		121
6.1	Introduction.....	121
6.2	Symmetry analysis	123
6.3	Application to realistic dyes.....	126
6.4	Conclusions.....	131
Chapter 7: Exploiting Quantum Interference in DSSCs.....		133
7.1	Introduction.....	133
7.2	Bridge mediated charge recombination	136
7.3	Charge recombination through tight binding bridges	138
7.4	Atomistic DFT simulation of the dye-TiO ₂ interface	144
7.4.1	Linear Bridges.....	144
7.4.2	Cross-Conjugated Bridges	150
7.5	Conclusions.....	155
Chapter 8: Evaluation of the interfacial electrostatics effects through an effective one-body Schrödinger equation		157
8.1	Introduction.....	157
8.2	Description of the model.....	158
8.3	Results.....	163
8.4	Conclusions.....	166
8.5	Appendix: Evaluation of the potential energy	168
8.6	Appendix: Derivation of the matrix elements recursion relations	175
Conclusions		179
Bibliography		183

List of Figures

Figure 1. Schematics of a dye sensitised solar cell.	2
Figure 2. Energy diagram for a typical dye sensitised solar cell.....	4
Figure 3. (a) Schematic representation of the electronic initial and final states. (b) Representation of the vibronic levels.	20
Figure 4. Pictorial representation of the harmonic nuclear potential for the initial and final vibrational states	27
Figure 5. (Top panel) Schematic representation of the energy levels of the semiconductor, the bridge and the molecule and their coupling. (Bottom panel) physical partition of the systems into semiconductor, bridge and adsorbed molecule.	28
Figure 6. (a) Elementary processes taking place in a DSSC. (b) Alignment of energy levels defined in the text.	40
Figure 7. Chemical structures and experimental recombination times for the molecular systems considered.....	56
Figure 8. Calculated recombination properties of the NKX dyes.	59
Figure 9. Calculated recombination properties of the OH dyes.	62
Figure 10. Spectral density of the OH2 dye.	64
Figure 11. Spectral density of the OH4 dye.	65
Figure 12. The effect of uncertainty in the value of λ for the chromophores NKX2311 (left panel) and OH1 (right panel).	69
Figure 13. Uncertainty on ΔG and its impact for the chromophores NKX2311 (left) and OH1 (right).	70
Figure 14. Recombination lifetime using Marcus's and Jortner's expression.	70
Figure 15. Adsorption configurations for the anatase (101)-electrolyte system.	89
Figure 16. Spectral densities (left panel) and Franck-Condon terms (right panel) for the electrolytes considered	90
Figure 17. Recombination lifetimes as a function of the applied bias potential for I_2 and I_3^-	92
Figure 18. Recombination lifetime for I_2^-	95
Figure 19. Recombination lifetimes as a function of the conduction band edge.	96
Figure 20. Schematics of the system studied	104
Figure 21. Schematics of the energy levels present in the model	104
Figure 22. The local density of states for a simple cubic lattice evaluated at the adsorption site	108
Figure 23. Contour plot of the logarithm of the charge recombination lifetime as a function of E_m and λ	111
Figure 24. (a) Value of the smallest eigenvalue for the lattice energy spectrum relative to the CB minimum as the defect on-site energy α_d is varied. (b) CR lifetime as a function of the defect on-site energy.	113
Figure 25. Charge recombination lifetimes as a function of the defect position	115
Figure 26. CR lifetimes for different acceptors as a function of the conduction band shift.....	118

Figure 27. Sketch of the symmetry elements present in the molecular systems considered.....	125
Figure 28. The azulene, fluorene, pyrene molecules with an illustration of their symmetry plane	127
Figure 29. Chemical diagrams and HOMO and LUMO plots of three molecules substituted with a bridge	129
Figure 30. Schematics of the adsorption of three substituted pyrenes on anatase (101).....	131
Figure 31. Sketches of dye molecules featuring a cross-conjugated bridge (top) and a linearly conjugated one (bottom).	135
Figure 32. (a) Illustration of the energy levels for the electron transfer from the bottom of the conduction band of the semiconductor to the dye. (b) Spectral density for a bridge with antiresonance. (c) Spectral density for a bridge without antiresonances.	137
Figure 33. Sketches of the tight-binding systems considered	139
Figure 34. Green's function (in absolute value) for the linear tight-binding bridges L4 and L6.....	141
Figure 35. Green's functions for the XC5 bridge.....	142
Figure 36. Charge recombination lifetime for the XC5 bridge as a function of the cross-conjugated group site energy	144
Figure 37. Chemical structure of the dyes considered	145
Figure 38. Spectral density for the dyes considered.....	148
Figure 39. Charge recombination lifetime as a function of the bridge length.....	149
Figure 40. Chemical structures for the Pyrene derivatives	150
Figure 41. Bridge mediated semiconductor-dye coupling for electron withdrawing cross-conjugated groups (left panel) and for electron donating groups (right panel).....	151
Figure 42. Charge recombination lifetimes for cross-conjugated molecules as a function of the chemical substituent.....	153
Figure 43. (a) Dihedral angle θ studied in the $-\text{OH}$ and $-\text{H}$ substituted bridges. (b) Energy scan for the $-\text{OH}$ substituted molecule as a function of the dihedral angle. (c) Charge recombination lifetimes (τ_{CR}) for the $-\text{OH}$ ($-\text{H}$) substituted bridge.....	154
Figure 44. (a) Sketch of the model system and cylindrical coordinate system employed. (b) Section plane in which the electronic wavefunction will be evaluated.....	160
Figure 45. Real space representation for the electron density	163
Figure 46. Contour plot for the electronic wavefunction	164
Figure 47. Ground state energy for the exciton.	165
Figure 48. Sketch of the interface between the two media and position of the charge q relative to it.....	168
Figure 49. Image charge method to determine the field at point P	169
Figure 50. Charge distribution generating φ_2	170
Figure 51. Screened charge q'' and self-image interacting with an extra charge in the second medium.....	173

Acknowledgements

I am deeply in debt with my supervisor, prof. A. Troisi for the guidance and support given throughout the duration of my study period. I would like to express heartfelt gratitude for the many stimulating discussions and critical insights that have improved drastically the quality of the scientific output produced during this PhD.

It has been a pleasure to collaborate with Dr. Natalia Martsinovich during part of my PhD. Her dedication and exactness have set an example for me to follow in the years to come. I would also like to thank Dr. Héctor Vázquez for critically reading part of this manuscript and contributing to clarify it.

I am also glad to acknowledge the contribution from prof. G. Salomon and prof. T. Hansen for the useful discussions during my visit at the University of Copenhagen in November 2012.

I kindly acknowledge EPSRC for financial support.

Declaration

This thesis is submitted to the University of Warwick in support of my application for the degree of Doctor of Philosophy. It has been composed by myself and it has not been submitted in any previous application for any degree.

The work presented (including data generated and data analysis) was carried out by the author except in the cases outlined below:

Spectral densities for all the systems considered in chapters 3 and 6 have been generated by Dr. Martsinovich, as well as the analysis of these quantities in sections 3.3.1 and 3.3.2 including the dependence on nuclear conformations.

Parts of this thesis have been published by the author:

1. Maggio, E.; Martsinovich, N.; Troisi, A. Evaluating Charge Recombination Rate in Dye-Sensitized Solar Cells from Electronic Structure Calculations. *J. Phys. Chem. C* **2012**, *116*, 7638–7649.
2. Maggio, E.; Martsinovich, N.; Troisi, A. Theoretical study of charge recombination at the TiO₂-electrolyte interface in dye sensitised solar cells. *J. Chem. Phys.* **2012**, *137*, 22A508–8.
3. Maggio, E.; Martsinovich, N.; Troisi, A. Using Orbital Symmetry to Minimize Charge Recombination in Dye-Sensitized Solar Cells. *Angew. Chem. Int. Ed.* **2013**, *52*, 973–975.
4. Maggio, E.; Troisi, A. An expression for bridge mediated electron transfer rate in dye sensitised solar cells. *Phil. Trans. R. Soc. A* approved for publication.
5. Maggio, E.; Troisi, A. Theory of the charge recombination reaction at the semiconductor-adsorbate interface in the presence of defects. *J. Phys. Chem. C* **2013**, submitted.
6. Maggio, E.; Solomon, G. C.; Troisi, A. Exploiting Quantum Interference in Dye Sensitised Solar Cells, *ACS Nano*, submitted.

Abstract

In this thesis we present a theoretical approach to the study of the charge recombination reaction in dye sensitised solar cells. An expression for the charge transfer rate at the semiconductor-molecule interface has been derived in chapter 2, within the theoretical framework of the non-adiabatic electron transfer. Computational procedures are presented in chapters 3 and 4 for realistic systems and the comparison with experimental data is reported. In chapter 5 we explore some strategies to impede the charge recombination reaction and we assess the impact of lattice defects on these strategies. In chapters 6 and 7 we present two innovative approaches to minimise the charge recombination rate, based on the partitioning scheme applied in chapter 2. We then suggest alternative designs for the molecular sensitiser and test the rationale of the strategies proposed with calculations of realistic systems at the Density Functional level of theory. A phenomenological model of the electron at the semiconductor-solvent interface is presented in chapter 8 to test one of the assumptions underpinning the theoretical scheme.

List of abbreviations and symbols

B3LYP Becke, 3-parameter, Lee-Yang-Parr (exchange and correlation functional)

CB Conduction Band

CBm Conduction Band minimum

CI Charge Injection

CRD Charge Recombination to Dye⁺

CRE Charge Recombination to Electrolyte

DFT Density Functional Theory

DoS Density of States

DPZ Double- ζ Polarised

DSSC Dye Sensitised Solar Cell

e Elementary charge ($1.60217657 \times 10^{-19}$ C)

E_C Conduction Band minimum energy level

E_F , E_f *quasi*-Fermi level

$E_{F,0}$ *quasi*-Fermi level in the dark

$E_{F,n}$ *quasi*-Fermi level under illumination

$E_{F,redox}$ Fermi level for the redox couple

$F(E)$ Franck-Condon thermally averaged density of nuclear states

$f_\mu(E)$, $f(E-E_F)$ Fermi-Dirac distribution

GGA Generalised Gradient Approximation

\hbar Reduced Planck's constant ($6.58211928 \times 10^{-16}$ eV·s)

k Pseudo-first order charge recombination rate

k_B Boltzmann constant ($8.617\,3324 \times 10^{-5}$ eV·K⁻¹)

m_e Electron mass ($9.10938291 \times 10^{-31}$ kg)

PBE Perdew-Burke-Ernzerhof (exchange and correlation functional)

PCM Polarisable Continuum Model

T Absolute temperature (298.15 K)

TAS Transient Absorption Spectroscopy

$\Gamma(E)$ Spectral density (also dye-semiconductor effective coupling)

$\Gamma_{mn}(E)$ Semiconductor's spectral density

ϵ_0 Vacuum permittivity ($8.854187817620 \times 10^{-12}$ C·V⁻¹·m⁻¹)

μ Electron chemical potential or electron effective mass

τ Charge Recombination Lifetime

Chapter 1: Introduction

1.1 Overview

The quest for sustainable energy sources is one of the most pressing problems that the industrialised society is currently facing and it is still lacking a satisfactory solution. A striking example is given by the gradual change in fuels employed to meet the ever-increasing electricity generation demand: from the 1970s to modern days fossil fuels usage has shrunk marginally (from 75% to 67%) in comparison with less polluting and more sustainable energy sources, such as wind, tidal, nuclear and solar power [1]. In this regard, solar energy represents the most attractive alternative, considering that the solar luminosity exceeds the current global energy consumption by more than ten orders of magnitude. The benefits of an efficient technology to harvest the solar power to meet our energy demand would be immense.

The device for converting solar power into electricity is a solar cell and many different architectures exist, including the more commercially widespread silicon based [2], and dye sensitised solar cells (DSSCs) that represent an emerging alternative. Designed by O'Regan and Grätzel [3], DSSCs' main attractive feature is the promising efficiency [4] and the relatively inexpensive fabrication process [5]. These new devices can be classified as photoelectrochemical cells, effectively combining in their mechanism the light harvesting process and redox reactions involving their molecular constituents. In the original formulation DSSCs are assembled from (i) a nanoporous semiconductor thin film which constitutes the photoactive electrode, (ii) molecular dyes capable of stable and irreversible binding to the semiconductor surface, (iii) an electrolyte solution that permeates the

nanoporous electrode, (iv) a counter electrode where the oxidised electrolyte species are regenerated. The working mechanism can be outlined as follows: upon light absorption the dye is promoted to an electronic excited state configuration and then, if the energy level alignment is favourable, injects an electron in the semiconductor's conduction band to generate an out-of-equilibrium charge density. This process occurs on a femtosecond timescale. This charge can then be collected across an external circuit to produce an electrical current. Electron donating species in the electrolyte present can regenerate the oxidised dye and then diffuse to the cathode, to close the circuit. This mechanism is pictorially represented in Figure 1.

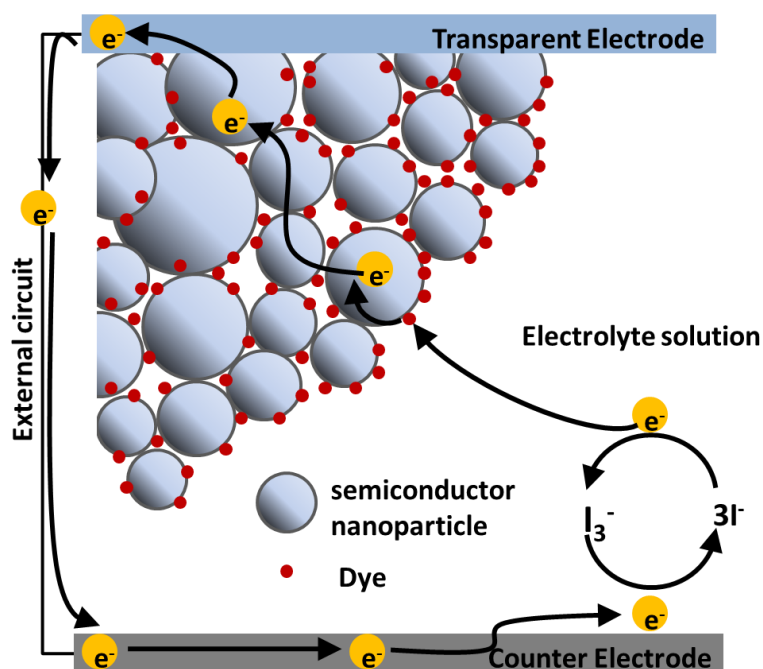


Figure 1. Schematics of a dye sensitised solar cell adapted from Ref. [6].

In Figure 2 we report the corresponding energy diagram for a typical DSSC [7], where we have indicated with green arrows the photoexcitation process and the charge injection (CI) process into the semiconductor's conduction band, as well as

the unwanted charge recombination steps in red. The recombination processes can be classified according to whether the acceptor species involved is the oxidised dye molecule (charge recombination to dye, CRD) or oxidised species of the electrolyte (CRE). Albeit these dissipative pathways are active over a timescale from 0.1 to 10 ms [7], they can nevertheless occur in a functioning device because of the slow electron diffusion in the nanostructured electrode. The theoretical study of these charge recombination reactions and the analysis of strategies to hinder them is the subject of this thesis.

Given the variety of materials required to assemble a DSSC, experimental studies (reviewed in Ref. [8]) have focused on the relationship between the separate components and device performances. In particular, the design of dyes and electrolyte shuttles can provide a virtually infinite palette of molecular components from which to choose to improve the device efficiency. This can be experimentally quantified by two parameters: the photocurrent obtained at short circuit and the maximum potential difference that the device can generate which is the potential difference at open-circuit conditions. A higher photocurrent is achieved by increasing the dye's light-harvesting power, its injection efficiency and the electron mobility in the semiconductor substrate, while it will be curbed by quenching of the dye's excited state, dissipative pathways for the electron population in the semiconductor's conduction band and electron trapping by defects states. The photovoltage, instead, is modulated exclusively by the energy level alignment at the photoelectrode, which may be dependent on the light intensity. The energy levels affecting the open-circuit potential are those of the charge carriers on either side of the interface, i.e. the

chemical potential of the electrons in the conduction band and of the redox couple in solution (indicated as $E_{F,redox}$ in Figure 2).

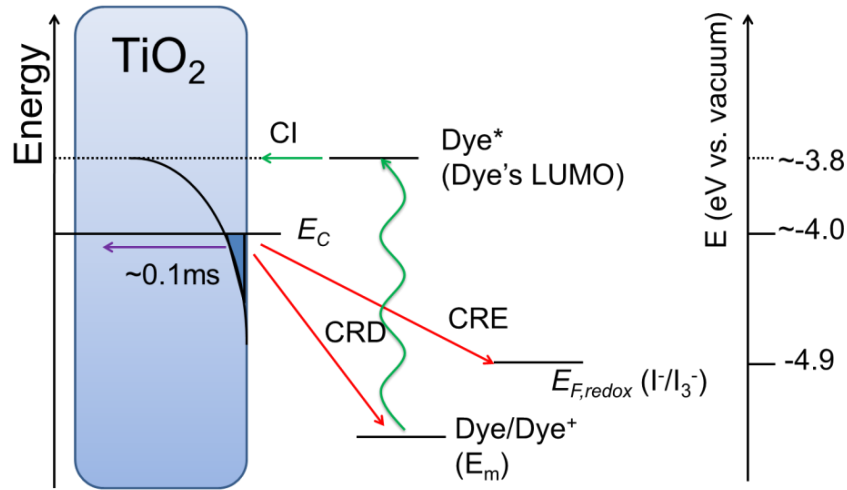


Figure 2. Energy diagram for a typical dye sensitised solar cell. The energy levels reported are the dye's HOMO (indicated with E_m) and LUMO orbitals, the semiconductor's conduction band minimum E_C and the redox couple Fermi level $E_{F,redox}$. Image adapted from Ref. [6].

The main breakthrough in the design of the photoactive electrode is the introduction of nanostructured substrate to guarantee a high surface/volume ratio to improve the sensitisation process and increase the device absorbance. TiO_2 (anatase) nanoparticles were first employed [3], although TiO_2 nanowires [9] have also been considered as well as different semiconductors such as ZnO [10], SnO_2 [11], Nb_2O_5 [12], SrTiO_3 [13]. The rationale underpinning these experimental investigations was the change in morphology of the nanostructured phase and/or the relative alignment of the energy levels involved in the interfacial charge transfer (shown for the typical TiO_2 -based device in Figure 2) to reduce the impact of dissipative pathways in the charge conversion mechanism either by increasing the electron mobility or by

making the unwanted charge recombination reactions less favourable. To improve the photocurrent generated, modifications in the sensitizer chemical structure have been extensively studied [14] both in metal-organic complexes [7] and organic dyes [6]. Without being exhaustive, we can mention the efforts aimed at increasing the fraction of solar radiation absorbed [15], the timescale of electron injection into the semiconductor's conduction band [16] and slowing down the charge recombination dynamics [17, 18]. Other structural changes were directed at modulating the interaction with electrolyte species in order to affect the other dissipative pathway – CRE [19, 20]. The strategies outlined either implied an increase in the number of electrons being injected into the semiconductor conduction band or were aimed at preserving that out-of-equilibrium electron population by curbing dissipative pathways. From Figure 2 we can see how the first strategy is practically implemented by moving the dye's HOMO level to higher energies [21], as the dye's excited state has to lie above the conduction band edge (E_C) for a fast and quantitative injection process [13]. The inherent limitation of this approach is that an offset between the oxidised dye's energy level and the position of the electrolyte Fermi level is required to drive the dye regeneration reaction; hence the dye's HOMO can't be indefinitely shifted at higher energies.

The redox couple is also integral to the device optimisation strategy, as the potential difference at open-circuit conditions is immediately related to the redox couple's Fermi level position. The I_3^-/I^- couple, originally introduced by O'Regan and Grätzel [3], has been progressively replaced over the years by cobalt-based [22, 23] or iron-based [24] electrolytes that show a simpler electrochemistry in solution in comparison with the prototypical iodine couple. Recent innovations include organic

redox couples [25] and solid state architectures [26] to reduce the diffusion-related limitations. All these redox couples are characterised by a Fermi level (i.e. the energy level of the hole migrating through the electrolyte) positioned at lower energy than in the I_3^-/I^- couple; this increases the maximum work that can be obtained from the device, which is given by the difference between this energy level and that of the charge carriers in the semiconductor collected by the external circuit. Although devices based on these redox mediators show improved efficiency, this situation is resonant with what was said previously on the dye's HOMO energy alignment: the electrolyte's Fermi level will have to lie at higher energies than the dye's HOMO, and if both energy levels are lowered, then a smaller fraction of the solar radiation will be harvested. Furthermore, as we show in chapter 5, a redox couple with a lower oxidation potential will give a faster CRE if its affinity for the TiO_2 surface remains unchanged. Many other experimental 'tricks of the trade' have been introduced in the literature on DSSCs, these include the use of additives (such as 4-tert-butyl pyridine to locally modify the nanoparticles' interfacial electronic properties [27] or deoxycholic acid to reduce the aggregation of dye molecules [28]). Chemical treatments that the semiconductor can undergo to reduce the impact of lattice defects on the charge recombination processes [29, 30] can also modify the relative energy alignment at the interface.

The experimental evidence therefore suggests that the main route for improving the device performances is increasing the number of collected electrons after injection in the semiconductor conduction band. This can be achieved by slowing down the charge recombination processes occurring at the semiconductor-molecule

interface; for this reason we believe that gaining a better theoretical insight of these processes could inform the design of more efficient dye sensitised solar cells.

1.2 Experimental techniques

Several experimental techniques are available to study the elementary processes in DSSCs, some of them designed specifically to probe the charge recombination reaction kinetics under different illumination regimes. Small perturbation kinetic techniques, including (electrochemical) impedance spectroscopy [31, 32] and intensity modulated photovoltage (or photocurrent) spectroscopy [33–35], can be used to fully characterise the device in terms of the resistance and timescales of the elementary steps under steady state conditions by applying an harmonically modulated variation to the light intensity and measuring the (linear) response of the system. To investigate electron lifetimes and their diffusion coefficient, time transient decays can be studied under illumination [36–38] or in the dark under applied bias [39–41]. The interpretation of the results is based on a circuit model of the device; the electron lifetimes for each process can then be obtained and used to characterise the kinetics of the charge conversion steps. Charge extraction measurements can be used to monitor (as a function of time) the charge depletion in the photoelectrode [42, 43] but, similarly to the techniques mentioned thus far, cannot track the molecular species involved in the charge transfer processes studied. To complement the information obtained, transient absorption spectroscopy [44–46] measurements can follow the time evolution of the species involved in the electron transfer process, if they have a distinctive absorption signature. Data from these

experimental set-ups will be considered in chapters 3 and 4 when benchmarking the electron transfer theory developed in this thesis.

The framework for the interpretation of kinetic measurements is given by the multiple-trapping model, which relies on a classical picture of the charge carriers reaction-diffusion dynamics. The resulting continuity equation for the electron density can be solved numerically given the appropriate boundary conditions [47]; interestingly, this approach outlines two different scenarios depending on the role played by the charge recombination reaction [48, 49]. If the mechanism is electron transport limited, i.e. the charge recombination is fast compared with the diffusion in the semiconductor film, consistently with the limit of strong dye-semiconductor electronic coupling, the dependence of the open-circuit voltage on the incident light intensity follows the one expected for an ideal diode. Whereas if the kinetics is dominated by the interfacial electron transfer, the open-circuit voltage behaviour will be non-ideal and will depend on the electrode characteristics such as the distribution of trap states present. Both scenarios have been explored by Monte Carlo simulations of the classical (continuous time random walk) electron dynamics [50]; however, experimental evidence [51, 52] points strongly towards a non-ideal behaviour for the vast majority of experimental systems. This is generally justified by assuming non-linear properties for the electron diffusion and recombination mechanism, which can lead to the electron diffusion length being dependent on the electron population in the conduction band [53]. The charge recombination represents the bottleneck in real devices, but since it is also dependent on the electron concentration, we have that slower recombination kinetics will result in higher energy states in the semiconductor's conduction band being occupied under open-circuit conditions to

offset the flux of electrons being injected. This translates immediately into a bigger open-circuit potential, provided that the electrolyte Fermi level remains constant.

1.3 Standard computational chemistry methods

Computational tools developed in the field of quantum chemistry can help in the search for optimal molecular constituents, in particular, dye molecules will have to (i) absorb a large fraction of the solar radiation, (ii) show a favourable energy alignment, with the dye's injecting orbital lying above the semiconductor's conduction band edge, and (iii) have this orbital localised near the semiconductor surface for increased photocurrent [54]. All of these features can be routinely checked with standard density-functional theory (DFT) techniques, which can then inform the design of new sensitisers [55, 56]. The calculation of absorption spectra is generally performed at the time-dependent DFT level of theory, which gives a satisfactory description of the molecules' excited states in agreement with more accurate *ab initio* techniques [57] and can include solvation effects almost routinely with the aid of continuum models for the solvent [58]. The DFT calculations can therefore be applied successfully in synergy with experiment to refine the molecular characteristics of the optimal sensitiser, but they also represent the first step for a theoretical description of the elementary charge transfer steps. To this end, more sophisticated (and computationally demanding) simulations of the semiconductor-dye interface are required to determine the adsorption configuration of the dye [59–61], which will affect the coupling between the two subsystems (which is a key ingredient for the quantum dynamics simulations described further on). Simulations have also been performed to assess the impact of solvent molecules on the dye's

adsorption geometry [62] and the variation induced on the semiconductor's energy levels [63]. The combined variation of energetic and structural parameters on either side of the interface makes this type of study relevant for understanding the details of the elementary electron transfer [34]. Hence, atomistic simulations of the electrode-redox species interface [64] can provide a fundamental insight into these effects. In the case of DSSCs, the main challenge for theoretical methods is the lack of a well-defined interface in the experimentally studied systems, at the same time an accurate simulation of the full interface (including not just the semiconductor and the dye but also solvent molecules and additives) is unfeasible due to computational constraints: for instance, the effect of Li^+ ions, typically present in experimental realisations [65], is seldom considered in DFT simulations of the interface, notwithstanding the well-known impact of these species on the energy level alignment across the interface [66]. Because of this fundamental aspect in conjunction with the limitations of DFT methods [67], we will rely on some input from experimental sources when the theory of electron transfer developed herein will be compared with experimental electron recombination times in chapters 3 and 4.

1.4 Charge carrier dynamics simulations

The microscopic picture of the charge carriers dynamics conveyed by the so-called multiple-trapping model can be extended to more sophisticated numerical simulations of the charge dynamics in the photoelectrode [45, 50]. These are classical simulations of an electron performing a random walk over an energetically disordered lattice, endowed with an exponential distribution of trap states below the conduction band minimum. According to the postulates of the multiple-trapping

model, these trap states do not contribute to the electron diffusion process; a thermal activation of the trapped electrons is necessary for them to access the conduction band and to show a non-trivial dynamics.

As mentioned earlier, these theoretical approaches lack a full quantum mechanical description of the electrons involved, although tunnelling can be introduced in an *ad hoc* fashion [68]. To fully assess the impact of structural changes to the dye molecule, a full quantum description has to be invoked. This can be achieved by several quantum dynamics schemes developed over the years that can describe accurately fast electron transfer processes. In many cases the time-dependent population of the initial state is obtained by wavepacket propagation under a model Hamiltonian [69], parameterised with computational data or with experimental input [70]. Nuclear vibrational modes can be treated [71], although only a low-order polynomial expansion of the coupling matrix elements of the acceptor's and donor's states around the equilibrium geometry has been implemented in practice. Other studies include the presence of the semi-infinite semiconductor surface through a Green's function formalism [70, 72], which operates on diabatic states pertaining to different partitions of the overall system. The (electronic) coupling between the semiconductor and molecule subsystems thus introduced quantifies the interaction between them and triggers the charge transfer process.

The model Hamiltonian has been extended by the May group to include the interaction with electromagnetic fields [73] and it has been shown that the electron injection dynamics can be modulated by a designed light pulse if two different injection channels coupling the semiconductor with the molecule are present [74]. This idea, although intriguing, can scarcely be implemented in real DSSCs where the

incident radiation is surely not monochromatic. On the other hand, we will show in chapters 6 and 7 how the CRD process can be impeded by chemical design of an inefficient recombination pathway without affecting the charge injection step.

Full atomistic electron dynamics simulations provide a complementary description of the system, particularly relevant, for example, when the role of crystalline lattice defects near the interface is to be evaluated [75]. The computational scheme for these simulations, devised by the Prezhdov group [76, 77], can be regarded as a time-dependent DFT evolution used to obtain the adiabatic potential energy of the nuclei coupled to a classical molecular dynamics treatment for the nuclear motion; the electronic transition probabilities from one state to the other depend on the atomic coordinates and this induces a correlation between electronic and nuclear modes. Since an adiabatic picture of the nuclear motions is being implemented, the non-adiabatic contribution to the dynamics is introduced through the quantum-classical mean field approach [78] or hopping between different adiabatic surfaces [76], this allows to break down the adiabatic and non-adiabatic contributions to the charge injection dynamics, and we will qualitatively discuss this point later on.

A different philosophy animates the simulation by the Batista group where classical molecular dynamics simulations of the interface are used to obtain thermalized nuclear configurations, then the electronic properties are computed over a vast sample of snapshots at the extended-Hückel level of theory. For charge injection studies [79, 80] the electron transfer was quantified by estimating the occupation probability of the injecting electronic state, while for charge

recombination processes [81] the rate of the electron transfer was estimated within classical transition state theory.

Although based on an idealised Hamiltonian, the approaches presented above can characterise the quantum dynamics of the system for a timespan that does not exceed the picoseconds timescale. Similarly, full atomistic electron dynamics simulations are limited by computational constraints: also for these studies the elementary processes that can be simulated occur within picoseconds, hence they can chiefly be applied to fast electron transfer processes, such as the charge injection step. Owing to the timescales accessible to the methods briefly summarised above, it is not surprising that very few attempts have been made to compute the charge recombination half-life, prevalently focussed on radical electrolyte species [76, 81]. Furthermore, these studies cannot dissect the contribution of specific molecular portions to the charge recombination process and, given the computational cost, it is very unlikely that new strategies for the design of innovative sensitisers will be tested with these methods. In chapter 2 we report an expression for the charge recombination rate that is not limited to short timescales and can easily integrate a partition of the system based on the chemical intuition, to assess the contribution of each fragment and to allow a quicker scan of the molecular systems considered. Therefore, the results presented in this thesis will hopefully fill a gap in the existing scientific literature, allowing the systematic theoretical study of the main loss mechanism in dye sensitised solar cells.

1.5 Remarks on charge transfer

As mentioned in the first section, the timescales for the two processes considered, charge injection and charge recombination, differ greatly with the first reaction occurring within femtoseconds, while the second reaction is much slower. The reason why it is necessary to treat the injection and the recombination processes differently lies in the different role of the nuclear rearrangements taking place with the electron transfer. In the case of the electron injection, we have the promotion of the system to a metastable state, with one electron in the molecular portion occupying, for instance, the dye's LUMO. The decay of this metastable state, assuming that the quenching of the excited state can be disregarded, takes place through the injection of the excited electron into the manifold of empty states represented by the semiconductor's conduction band. The manifold of accepting states is electronic not nuclear and the injection occurs in the timescale of femtosecond. To a good degree of approximation [71, 82] the nuclear motions cannot follow such a rapid change of electronic states and can be neglected.

Instead, for the charge recombination process the acceptor state belongs to the vibrational manifold associated with the oxidised dye's internal vibrations and with the solvent nuclear orientations around the dye molecule. Assuming that the probability to access the transition state configuration is controlled by the thermal motion, these fluctuations of the nuclear and environmental degrees of freedom provide a pathway for the charge transfer reaction to occur as they affect the energy landscape of the molecular subsystem. Hence, a particular configuration can arise such that the nuclear overlap between the initial and final vibrational state is maximised.

In turn, changes in the nuclear orientation of the solvent molecules are responsible for the dielectric response of the solvent to the electron transfer process. This is included in the model through the Marcus picture of the charge transfer reaction when the system is embedded within a continuum dielectric.

The presence of solvent modes, however, is not just important for the influence on the energetics of the charge transfer, but also at a more fundamental level. The underpinning assumption for the process to be described by a kinetic approach (and not by following explicitly the dynamics of the electron motion) is that once reached the nuclear configuration corresponding to the transition state the system evolves irreversibly into the final state. This is guaranteed by two equivalent statements [83]: (A) the density of accepting states is exceedingly large, so that the broadening of the electronic level interacting with the acceptor manifold is big compared with the spacing within the manifold itself or (B) the total width of each (vibronic) acceptor's level is large compared to the spacing between the acceptor's electronic levels. It is easy to see that condition (A) is fulfilled for the electron injection process, when a single electronic molecular level is interacting with a quasi-continuum of acceptor states in the semiconductor conduction band, but this is no longer the case if the injecting state is degenerate with the conduction band minimum, as in Refs [76, 77]. Therefore, the adiabatic component of the electron dynamics observed, for example, for alizarine on TiO_2 in Refs [76, 77] is consistent with the energy alignment peculiar to that molecular sensitizer considered, rather than a general feature of the charge injection process in DSSCs. Condition (B) translates into having "an effective continuum for the relaxation process" following the charge transfer; for the charge recombination reaction this is guaranteed by the presence of solvent modes, provided

that the coupling with the solvent bath modes is strong enough. This qualitative argument will possibly justify why for the charge recombination reaction we can surely assume that the electron transfer is well described by a single rate, rather than by the time-dependent state occupation, while for the charge injection some *caveat* [71] must be considered.

1.6 Thesis outline

The outline of this thesis goes as follows: in chapter 2 we introduce on a more substantial basis the model of charge recombination and we deduce an expression for the charge recombination rate. We then validate the model against the experimental evidence available for the CRD process (in chapter 3); the recombination to the I_3^-/I^- electrolyte couple is examined in chapter 4. In chapter 5 we consider the viable material optimisation strategies in a realistic device, which can be implemented by modifying the model's parameters, such as the relative alignment of the energy levels and the reorganisation energy. The electronic coupling is analysed in chapter 6, where a special class of molecules is introduced that shows a vanishingly small coupling with the TiO_2 surface thanks to a special symmetry requirement. In chapter 7 we show how it is possible to manipulate the semiconductor-molecule coupling by molecular design even further, in synergy with the design rules of chapter 6. Both strategies presented here selectively slow down the charge recombination process without affecting the charge injection properties of the dye. In chapter 8 we report a dielectric continuum model for the photoinjected electron at the semiconductor interface. This model allows us to estimate the electron localisation and sensitivity to the surrounding charges. Conclusions are reported in chapter 9.

Chapter 2: Theory of the charge recombination rate at the semiconductor-molecule interface

2.1 Introduction

In this chapter we derive an expression for the pseudo-first order rate of electron transfer taking place at the interface between a semiconductor and a molecular system. This quantity is accessible experimentally and it is the reciprocal of the electron lifetime for the charge recombination reaction [36]. The derivation relies on the well-established theory of non-adiabatic electron transfer, with each electronic state in the semiconductor's conduction band contributing to the overall rate with a transition probability given by the Fermi Golden Rule.

The role of molecular vibrations and solvent rearrangement is incorporated in our treatment thanks to the Franck-Condon density of nuclear states, whose classical limit at high temperatures is estimated in section 2.3. Finally, we turn to the semiconductor-molecule electronic coupling in section 2.4, with the aim of deriving an expression able to dissect the direct electronic coupling between the initial and final states from the contribution of states localised on a bridge moiety connecting the semiconductor with the chromophore unit.

The expressions derived in this chapter will be employed throughout the rest of the thesis and will be applied either to DFT simulations of the semiconductor-adsorbate interface (as in chapters 3 and 4) or to simplified tight binding models (when the role of the bridge will be analysed in chapter 7). The aim of this chapter, therefore, is to provide a general expression for the recombination rate, the

computational details of the specific implementation will vary from case to case and will be described where appropriate in the subsequent chapters.

2.2 General expression for the charge recombination reaction rate

In this section we derive an expression for the charge recombination rate based on the standard non-adiabatic electron transfer mechanism [84]; this will be later generalised to include the charge transfer mediated by a molecular bridge which is an extension to the current theory. The initial state of this electron transfer process is an electronic state where an electron is present in the semiconductor's conduction band manifold $\{l\}$ and the dye is positively charged. The manifold $\{v\}$ collects all vibrational states of the system. These vibrations are localized on the dye or the solvent and are not affected by the specific state l occupied in the semiconductor. The initial vibronic states can be therefore indicated as $\{|l, v\rangle\}$. We denote with m the final electronic state where there is no excess electron in the semiconductor's conduction band and a neutral dye present. When the system is in state m , the equilibrium position of the vibration on the dye/solvent is changed and this set of vibrational states after the CR is indicated with $\{w\}$, with the final vibronic states are indicated as $\{|m, w\rangle\}$. More formally, we can define the Hilbert space to which each electronic state $|l\rangle$ and $|m\rangle$ belong to as the direct sum of the Hilbert (sub-) spaces \mathcal{H}_{SC} and \mathcal{H}_{M} ; an arbitrary state in either of these spaces can be expressed as a linear combination of the eigenstates of the isolated semiconductor and molecule respectively (or any other complete basis set). The energy of each vibronic state can

be expressed as the sum of electronic and vibrational energy ($E_{l,v} = \varepsilon_l + E_v$, $E_{m,w} = \varepsilon_m + E_w$). A schematic of the energy diagram is shown in Figure 3, where, for simplicity we show only one normal vibrational mode.

The total Hamiltonian for the system is given by:

$$H = H_0 + \tilde{V} \quad (2.1)$$

$$H_0 = \sum_l (\varepsilon_l + E_v) |l, v\rangle \langle l, v| + (\varepsilon_m + E_w) |m, w\rangle \langle m, w| \quad (2.2)$$

$$\tilde{V} = \sum_l \tilde{V}_{lm} \langle v|w\rangle |l, v\rangle \langle m, w| + h.c. \quad (2.3)$$

H_0 represents the Hamiltonian where there is no interaction between initial and final states. The coupling \tilde{V} is the electronic coupling between states l and m and the form used in equation (2.3) implies that the Condon approximation has been used, i.e. $\langle l, v|\tilde{V}|m, w\rangle = \langle v|w\rangle \langle l|\tilde{V}|m\rangle$. The occurrence of an electron transfer reaction will modify the number of particles present in each sub-space \mathcal{H}_{SC} and \mathcal{H}_M , hence the relevant Hilbert space for the semiconductor will be a one-particle space (whose states with an abuse of language are indicated with $|l\rangle$) and the one-dimensional space \mathcal{H}_0 (whose only state is the *vacuum* $|0\rangle$). The Hilbert spaces on the molecular moiety, on the other hand, are $N-1$ (N) particle spaces before (after) the electron transfer has taken place. The coupling operator \tilde{V} acts between states belonging to all the Hilbert states listed above, however, the contribution of the *vacuum* state to the coupling is clearly null and also the action of \tilde{V} between different particle states on the same (molecular) moiety can be disregarded. The only contribution surviving

is then $\langle l|\tilde{V}|m\rangle$ with $|l\rangle$ one-particle state on the semiconductor and $|m\rangle$ is an N -particle state on the molecular system. The latter will be approximated in the following chapters with the highest molecular orbital occupied once the electron transfer has taken place. \tilde{V} may indicate a direct coupling between states l and m but also an *effective* coupling due to the coupling of states l and m to a bridge that connects them. The derivation in this section is indifferent to the origin of the coupling \tilde{V} which is discussed instead in section 2.4. Regardless of the electronic coupling microscopic interpretation, in its evaluation we are disregarding the effect of the electron-electron interaction within the molecular sub-system, as it is customary in similar models in the field of electrocatalysis [85, 86]. Instead, this effect will be taken into account when estimating the energy level position ε_m as specified in the following chapters 3 and 4, whereas we will not include the impact of the level shift due to the interaction with the semiconductor; this can be accounted for, in principle, by taking the Hilbert transform of the spectral density that is introduced below.

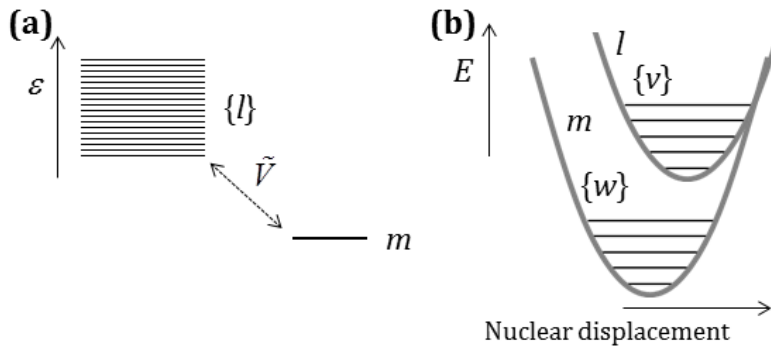


Figure 3. (a) Schematic representation of the electronic initial states ($\{l\}$), forming a continuum band and the final discrete state m . (b) Representation of the vibronic levels for one of the initial electronic states l and the final state m .

The total rate for the charge recombination, i.e. all transitions $\{l, v\} \rightarrow m\{w\}$, is the sum over the possible initial and final states weighted by the occupation on the initial states:

$$k_{\{l,v\} \rightarrow m,\{w\}} = \sum_{l,v} P_{\mu,T}(\varepsilon_l) P_T(E_v) \sum_w k_{l,v \rightarrow m,w} \quad (2.4)$$

$P_{\mu,T}(\varepsilon_l)$ is the probability of occupation of a state in the semiconductor with energy ε_l , function of the chemical potential μ in the semiconductor and the temperature T . $P_T(E_v)$ is the probability that the vibrational level with energy E_v is occupied. With the Hamiltonian defined above we have:

$$\begin{aligned} k_{l,v \rightarrow m,w} &= \frac{2\pi}{\hbar} \left| \langle l, v | \tilde{V} | m, w \rangle \right|^2 \delta(E_{m,w} - E_{l,v}) \\ &= \frac{2\pi}{\hbar} \left| \langle v | w \rangle \right|^2 \left| \tilde{V}_{lm} \right|^2 \delta(\varepsilon_m - \varepsilon_l + E_w - E_v) \end{aligned} \quad (2.5)$$

The total rate is:

$$k_{\{l,v\} \rightarrow m,\{w\}} = \frac{2\pi}{\hbar} \sum_l P_{\mu,T}(\varepsilon_l) \left| \tilde{V}_{lm} \right|^2 \sum_{v,w} P_T(E_v) \left| \langle v | w \rangle \right|^2 \delta(\varepsilon_m - \varepsilon_l + E_w - E_v) \quad (2.6)$$

The second summation in equation (2.6) is known as the thermally and Franck-Condon averaged density of nuclear states and indicated with:

$$F(\varepsilon_m - \varepsilon_l) = \sum_{v,w} P_T(E_v) \left| \langle v | w \rangle \right|^2 \delta(\varepsilon_m - \varepsilon_l + E_w - E_v) \quad (2.7)$$

Taking this into account, the expression for the total rate can be rewritten as [84]:

$$\begin{aligned}
 k_{\{l,v\} \rightarrow m, \{w\}} &= \frac{2\pi}{\hbar} \sum_l P_{\mu,T}(\varepsilon_l) |\tilde{V}_{lm}|^2 F(\varepsilon_m - \varepsilon_l) = \\
 &= \frac{2\pi}{\hbar} \sum_l \int dE P_{\mu,T}(E) |\tilde{V}_{lm}|^2 F(\varepsilon_m - E) \delta(E - \varepsilon_l) = \\
 &= \int dE f_\mu(E) \left[\frac{2\pi}{\hbar} \sum_l |\tilde{V}_{lm}|^2 \delta(E - \varepsilon_l) \right] F(\varepsilon_m - E) = \\
 &= \int dE f_\mu(E) \tilde{\Gamma}(E) F(\varepsilon_m - E)
 \end{aligned} \tag{2.8}$$

The quantity is $P_{\mu,T}(E)$ coincides with the Fermi-Dirac distribution and so it was rewritten as:

$$f_\mu(E) = \left(1 + e^{(E-\mu)/k_B T} \right)^{-1} \tag{2.9}$$

The spectral density $\tilde{\Gamma}(E)$ has been defined as:

$$\tilde{\Gamma}(E) = \frac{2\pi}{\hbar} \sum_l |\tilde{V}_{lm}|^2 \delta(E - \varepsilon_l) \tag{2.10}$$

This quantity can be considered a measure of the facility of electron transfer between state l and state m at energy E and in the absence of nuclear modes. In this limit it corresponds exactly to the lifetime of a state prepared initially in m and degenerate with the levels $\{l\}$. This latter situation was investigated in Ref. [56]. This term is equal (up to a dimensionality factor) to the imaginary part of the self-energy operator that is typically introduced in models for adsorption on a substrate, which can be either a metal (leading to the Newns-Anderson model [87]) or a semiconductor (as in the Haldane-Anderson model [88]). The real component of this complex-valued operator relates to the shift of the adsorbate's level position owing to

the interaction with the solid substrate; while this contribution is typically disregarded in the Newns-Anderson formulation (since the wide-band approximation is well justified for metals), it can be non-negligible when ε_m approaches the band edge [89]. We will disregard in general this contribution and will provide a justification when considering the specific molecular systems in the following chapters.

The Franck-Condon term F can be evaluated analytically if the vibrational wavefunctions are assumed to be displaced harmonic oscillators. In the limit of high temperature, when these oscillators can be treated classically, the Franck-Condon term [90] takes a particularly simple form:

$$F(\Delta\varepsilon) = \frac{1}{\sqrt{4\pi\lambda k_B T}} \exp\left[-\frac{(\Delta\varepsilon + \lambda)^2}{4\lambda k_B T}\right] \quad (2.11)$$

where λ represents the reorganisation energy (a measure of the geometry change between states l and m) and $k_B T$ the thermal energy. Explicit expressions for the spectral density (2.10) will be provided in section 2.4 and they will depend on the physical details of the interaction between the states considered (i.e. direct coupling vs. bridge mediated interaction). The derivation of the Franck-Condon term is reported next.

2.3 The Franck-Condon term in the semiclassical limit at high temperatures

In this section we derive the well-known analytical expression for the Franck-Condon term [83] introduced in equation (2.11) and discuss the approximations

required. As a starting point we assume that the change in the nuclear configuration between the initial and final state for each normal coordinate in the system doesn't affect the frequency of the molecular vibrational modes. The Hamiltonian associated with the molecular vibrations can then be written as:

$$\begin{aligned}\hat{H}_v &= \frac{\hat{p}^2}{2M} + \frac{1}{2}M\omega^2\hat{x}^2 \\ \hat{H}_w &= \frac{\hat{p}^2}{2M} + \frac{1}{2}M\omega^2(\hat{x} - \hat{\xi})^2 + \Delta\varepsilon\end{aligned}\quad (2.12)$$

where M represents the reduced mass of the system and ω its frequency; the energy displacement in energy $\Delta\varepsilon$ and along the normal coordinate ξ due to the change in oxidation state of the molecule are shown in Figure 4. The subscripts v and w refer to the vibrational quantum numbers associated with the Hamiltonian eigenfunctions [91]:

$$\chi_v(x) = \langle x|v\rangle = \frac{1}{\sqrt{v!2^n}} \left(\frac{M\omega}{\pi\hbar} \right)^{1/4} e^{-\frac{M\omega x^2}{2\hbar}} H_v \left(\sqrt{\frac{M\omega}{\hbar}} x \right) \quad (2.13)$$

where the Hermite polynomials H_v have been introduced. If more than one normal coordinate is present the derivation can be straightforwardly generalised to include them by letting v and w represent arrays of quantum vibrational numbers. Introducing the dimensionless change in the normal coordinate $\eta = \sqrt{\frac{M\omega}{\hbar}}\xi$ and $y = \sqrt{\frac{M\omega}{\hbar}}x$ we have:

$$\langle v|w\rangle = \frac{1}{\sqrt{\pi v!w!2^{v+w}}} e^{-\frac{1}{4}\eta^2} \int_{-\infty}^{+\infty} e^{-(y-\frac{1}{2}\eta)^2} H_v(y) H_w(y-\eta) dy \quad (2.14)$$

The explicit evaluation of equation (2.14) can be carried out [92], giving:

$$\langle v|w\rangle = \sqrt{2^{w-v} \frac{v!}{w!}} \left(-\frac{1}{2}\eta\right)^{w-v} e^{-\frac{1}{4}\eta^2} L_v^{w-v}\left(\frac{1}{2}\eta^2\right) \quad \text{for } w \geq v \quad (2.15)$$

where $L_v^\alpha(X)$ is the generalised Laguerre polynomial of order v . For the case $v \geq w$ the relation (2.15) holds for v and w swapped and with $-\eta$ replaced by η for the term in brackets. Expression (2.15) can be evaluated for each normal mode in the molecular system, and would retain the full quantum features of the description. However, in the high temperature limit the semiclassical approximation is more commonly used, and we report the derivation by Siders and Marcus [90].

By taking the Fourier transform of the Dirac's delta function in equation (2.7), the Franck-Condon term can be written as:

$$F(E_{mw} - E_{lv}) = \frac{1}{Q_l} \sum_{v=0}^{\infty} e^{-\beta\hbar\omega(v+\frac{1}{2})} \sum_{w=0}^{\infty} |\langle v|w\rangle|^2 \int_{-\infty}^{+\infty} \exp\left[\frac{i}{\hbar}(E_{m,w} - E_{l,v})t\right] \frac{dt}{\hbar} \quad (2.16)$$

By carrying the summation under the integral sign and inserting the exponential in the coordinate integral, one obtains:

$$F = \frac{1}{Q_l} \sum_{v=0}^{\infty} e^{-\beta\hbar\omega(v+\frac{1}{2})} \int_{-\infty}^{+\infty} dt \frac{1}{\hbar} \sum_{w=0}^{\infty} \langle v|w\rangle \langle w| e^{i\hat{H}_w t/\hbar} e^{-i\hat{H}_v t/\hbar} |v\rangle \quad (2.17)$$

where the eigenvalues of the vibrational states have been replaced by the Hamiltonian operators given in equation (2.12). The Lie-Trotter formula [93] can then be applied by replacing the (matrix-valued) exponentials with the expansion $\exp\left[\frac{i\hat{H}_t}{\hbar}\right] = \lim_{n \rightarrow \infty} \left(1 + \frac{i\hat{H}_t}{n\hbar}\right)^n$; if we disregard the commutators of the different Hamiltonian operators and consider the classical variables instead of the quantum operators (which is the semiclassical approximation) we obtain:

$$e^{i\hat{H}_w t/\hbar} e^{-i\hat{H}_v t/\hbar} \approx e^{i(\hat{H}_w - \hat{H}_v)t/\hbar} = \exp\left[-\frac{iM\omega^2\xi}{\hbar} t \left(x - \frac{1}{2}\xi - \frac{\Delta\varepsilon}{M\omega^2\xi}\right)\right] \quad (2.18)$$

Inserting expression (2.18) into (2.17) and taking its Fourier transform, the Franck-Condon term becomes:

$$\begin{aligned} F(\Delta\varepsilon) &= \frac{1}{Q_l} \sum_{v=0}^{\infty} \frac{1}{\hbar} e^{-\beta\hbar\omega(v+\frac{1}{2})} \left(\frac{M\omega^2\xi}{\hbar}\right)^{-1} \langle v | \delta\left(x - \frac{1}{2}\xi - \frac{1}{M\omega^2\xi}\Delta\varepsilon\right) | v \rangle = \\ &= \left(M\omega^2\xi Q_l\right)^{-1} \sum_{v=0}^{\infty} e^{-\beta\hbar\omega(v+\frac{1}{2})} \left|\chi_v\left(-\frac{1}{2}\xi - \frac{1}{M\omega^2\xi}\Delta\varepsilon\right)\right|^2 \end{aligned} \quad (2.19)$$

The harmonic oscillator eigenfunction in equation (2.19) is evaluated at the crossing point of the two potential energy curves. Recalling that for the partition function $Q_l = [2\sinh(\frac{1}{2}\beta\hbar\omega)]^{-1}$ and applying the Mehler's formula for the Hermite polynomials [94], equation (2.19) can be recast as:

$$F(\Delta\varepsilon) = \frac{1}{\sqrt{2\pi\lambda\hbar\omega\coth(\frac{1}{2}\beta\hbar\omega)}} \exp\left[-\frac{(\lambda + \Delta\varepsilon)^2}{2\lambda\hbar\omega\coth(\frac{1}{2}\beta\hbar\omega)}\right] \quad (2.20)$$

Where the reorganisation energy $\lambda = \frac{1}{2}M\omega^2\xi^2$ has been introduced; the proof is reported in the appendix. If we finally take the high temperature limit of equation (2.20), equivalent to retaining the lowest order term in the Taylor expansion for

$\coth(z) = \frac{1}{z} + \frac{z}{3} - \frac{z^3}{45} + \dots$, the classical result (2.11) is recovered.

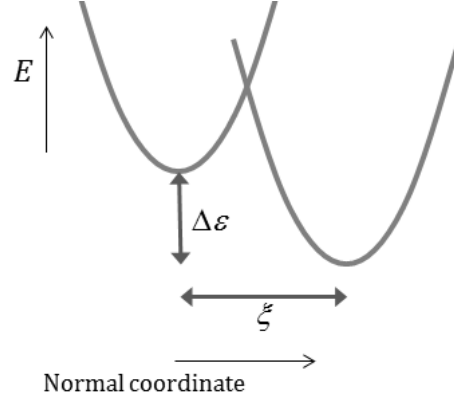


Figure 4. Pictorial representation of the harmonic nuclear potential for the initial and final vibrational states, which have been identified by their quantum numbers v and w respectively.

2.4 Bridge mediated semiconductor-dye electronic coupling

In the previous section we have considered the states $\{l\}$ and m as coupled by an effective coupling \tilde{V} . In this section we consider more specifically the situation of semiconductor states coupled with the dye directly or through states localized on the bridge. The total electronic Hamiltonian can be therefore written as the sum of the electronic Hamiltonian on the semiconductor (H_S^{el}), the bridge (H_B^{el}) and the molecule (H_M^{el}) plus the interactions between these three subsystems ($V^{el} = V_{SB}^{el} + V_{SM}^{el} + V_{BM}^{el}$), i.e.

$$H^{el} = H_S^{el} + H_B^{el} + H_M^{el} + V_{SB}^{el} + V_{SM}^{el} + V_{BM}^{el} \quad (2.21)$$

$$H_S^{el} = \sum_{l \in L} \varepsilon_l |l\rangle\langle l|; \quad H_B^{el} = \sum_{b \in B} \varepsilon_b |b\rangle\langle b| + \sum_{\substack{b' \in B \\ b' \neq b}} V_{bb'} |b\rangle\langle b'|; \quad H_M^{el} = \varepsilon_m |m\rangle\langle m| \quad (2.22)$$

$$V_{SM}^{el} = \sum_{\substack{l \in L \\ m \in M}} \gamma_{lm} |l\rangle\langle m| + h.c.; \quad V_{SB}^{el} = \sum_{\substack{l \in L \\ b \in B}} \tau_{lb} |l\rangle\langle b| + h.c.; \quad V_{BM}^{el} = \sum_{\substack{b \in B \\ m \in M}} \kappa_{bm} |b\rangle\langle m| + h.c. \quad (2.23)$$

A graphical representation of this system is given in Figure 5.

A number of techniques (perturbation theory [95], scattering theory [96], partitioning methods [97], Green's function methods [98–100]) have been used to express the effective coupling between subsystem S and M in an effective Hamiltonian that does not contain the bridge states explicitly, i.e.

$$H^{el} = H_S^{el} + H_M^{el} + \tilde{V}_{SM}^{el} \quad (2.24)$$

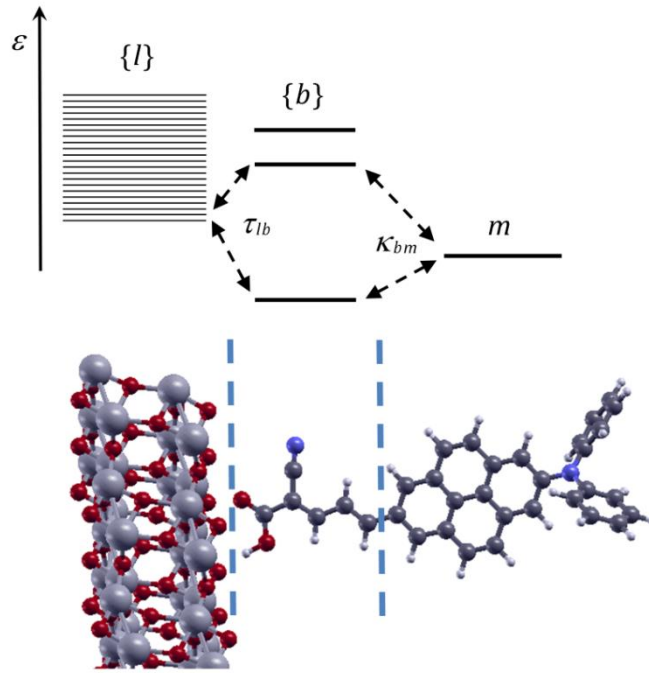


Figure 5. (Top panel) Schematic representation of the energy levels of the semiconductor, the bridge and the molecule and their coupling. (Bottom panel) physical partition of the systems into semiconductor, bridge and adsorbed molecule which approximately corresponds to the partition of the Hamiltonian.

Here we consider the effective coupling operator expressed from scattering theory as:

$$\tilde{V} = V^{el} + V^{el} G V^{el} \quad (2.25)$$

where the retarded Green's function operator can be defined as $G = ((E + i\eta)I - H^{el})^{-1}$, with I being the identity operator, E an independent variable and η a real positive infinitesimal. The effective coupling between states l and m is:

$$\langle l | \tilde{V} | m \rangle = \langle l | V^{el} | m \rangle + \sum_{b, b' \in B} \langle l | V^{el} | b \rangle \langle b | G | b' \rangle \langle b' | V^{el} | m \rangle \quad (2.26)$$

The first term in the right hand side of equation (2.26) takes care of the direct coupling between the initial and final electronic states. The second term accounts for the bridge mediated contribution to the electron transfer process, with the tunnelling probability across the bridge being given by the Green's function matrix elements. The only assumption made in the derivation of equation (2.26) is related to the completeness of the bridge states, which are not necessarily orthogonal to each other.

The Green's function operator for a bridge interacting with the semiconductor slab and the molecular fragment attached to it can be recast in terms of the Green's function for the non-interacting bridge plus a self-energy contribution that collects the perturbative effects on the bridge subsystem due to the interaction with the substrate [101]. The expression for the self-energy has been reported elsewhere [102] and for the energy range relevant to the charge recombination process only the interaction with the electrode plays a role, which has been evaluated as a test. Since the introduction of the self-energy in the calculation of bridge's Green's function would further complicate the theory without impacting on the results that will be presented in chapter 7 (as expected from the weak semiconductor-bridge coupling regime), we approximate it as $G_B(E) \approx G_B^0(E)$ where G_B is the matrix whose

elements appear in (2.26). For the case of a non-orthogonal basis set the Green's function for the non-interacting bridge can be computed as [103]:

$$G_B^0 = \left((E + i\eta) S_B^{-1} - S_B^{-1} H_B^{el} S_B^{-1} \right)^{-1} \quad (2.27)$$

where S_B is the overlap matrix over the bridge states and H_B^{el} includes the matrix elements $V_{bb'}$ and it is obtained by direct partitioning of the Hamiltonian matrix for the overall system semiconductor + adsorbate. We can then compute the effective coupling as:

$$\tilde{V}_{lm} = \gamma_{lm} + \sum_{a,b,c,d} \tau_{la} S_{ab}^{-1} G_{bc}^0 S_{cd}^{-1} \kappa_{dm} \equiv \gamma_{lm} + \sum_{b,b'} \tau_{lb} g_{bb'} \kappa_{b'm} \quad (2.28)$$

where the indexes run over the bridge states and the Green's function weighted by the overlap matrices has been indicated with the symbol $g_{bb'}$ to lighten the notation. The next step is to compute the spectral density $\tilde{\Gamma}(E)$ using the effective coupling expression above.

In the absence of a bridge (of if we assume that all the states of the bridge as part of the dye) we have $\tilde{V}_{lm} = \gamma_{lm}$ and the spectral density $\tilde{\Gamma}(E)$ can be expressed as [104]:

$$\tilde{\Gamma}(E) = \frac{2\pi}{\hbar} \sum_l |\gamma_{ml}|^2 \delta(E - \varepsilon_l) \quad (2.29)$$

In chapter 6 we will report a strategy for the design of the chromophore unit that will systematically reduce the contribution of this term to the charge recombination rate.

In the presence of the bridge the direct coupling is very small (because it decreases exponentially with the distance) and so it is reasonable to neglect the direct coupling γ_{lm} , i.e.

$$\tilde{V}_{lm} = \sum_{b,b' \in B} \tau_{lb} g_{bb'}(E) \kappa_{b'm} \quad (2.30)$$

for an orthonormal basis set. The modulus square of the coupling is given by:

$$\tilde{V}_{lm} \tilde{V}_{ml}^\dagger = \sum_{b,b' \in B} \tau_{lb} g_{bb'}(E) \kappa_{b'm} \sum_{a,a' \in B} \kappa_{a'm}^\dagger g_{a'a}^\dagger(E) \tau_{al}^\dagger \quad (2.31)$$

The spectral density reads:

$$\begin{aligned} \tilde{\Gamma}(E) &= \frac{2\pi}{\hbar} \sum_l \sum_{b,b' \in B} \tau_{lb} g_{bb'}(E) \kappa_{b'm} \sum_{a,a' \in B} \kappa_{a'm}^\dagger g_{a'a}^\dagger(E) \tau_{al}^\dagger \delta(E - \varepsilon_l) \\ &= \sum_{a,a' \in B} \sum_{b,b' \in B} \Gamma_{ab} g_{bb'}(E) \kappa_{b'm} \kappa_{a'm}^\dagger g_{a'a}^\dagger(E) \end{aligned} \quad (2.32)$$

where, for the last equality, we have introduced the semiconductor's spectral density

$$\Gamma_{ab}(E) = \frac{2\pi}{\hbar} \sum_l \tau_{al}^\dagger \tau_{lb} \delta(E - \varepsilon_l) \quad (2.33)$$

By further defining $K_{a'b'} = \kappa_{b'm} \kappa_{a'm}^\dagger$, we get:

$$\tilde{\Gamma}(E) = \sum_{a,a' \in B} \sum_{b,b' \in B} \Gamma_{ab} g_{bb'}(E) K_{b'a'} g_{a'a}^\dagger(E) = \text{tr} \{ \mathbf{\Gamma} \mathbf{g} \mathbf{K} \mathbf{g}^\dagger \} \quad (2.34)$$

where $\text{tr}\{\cdot\}$ denotes the trace operator over the bridge states and the bold type has been used for the matrices involved (of size of the total number of bridge states present).

Equation (2.34) is one of the main results of this thesis. This is the form of the spectral density that should be used in the expression of the rate (2.8) when the coupling between semiconductor and dye is mediated by a bridge. The spectral density $\tilde{\Gamma}(E)$ includes a matrix Γ that quantifies the coupling between semiconductor and bridge, a matrix \mathbf{K} (that quantifies the coupling between bridge and dye), and the Green's function matrix \mathbf{g} (which express the propagation across the bridge). As we mentioned in the previous section $\tilde{\Gamma}(E)$ would also be the rate of charge injection (tunnelling) of a state initially prepared in m and degenerate with the manifold $\{l\}$. It is therefore particularly appealing that the form obtained for $\tilde{\Gamma}(E)$ is very similar to the standard Landauer formula for the transmittance across a molecular system connected to two electrodes [105]. In the Landauer formula, instead of the matrix \mathbf{K} , there is another term like Γ , describing the coupling with a second electrode.

The aim of this chapter is to produce a formalism that can be applied in conjunction with electronic structure computations of the system of interest. The semiconductor-molecule interface can be routinely simulated, and, for typical chemical applications, the Hamiltonian and overlap matrices are expressed in terms of a localised, non-orthogonal basis set, such as a linear combination of atomic orbitals. Employing localised basis functions the expression for the spectral density (2.34) retains its validity if the propagator across the bridge is replaced by the overlap Green's operator introduced in equation (2.28). Finally, if we consider the chromophore unit, we can identify the state $|m\rangle$ with the isolated molecule's HOMO

which can be expanded in terms of the localised basis set as: $|m\rangle = \sum_j c_j^m |\phi_j\rangle$. The coupling between bridge states and state $|m\rangle$ can be expressed in terms of these localized states:

$$\kappa_{bm} = \langle b | V_{BM}^{el} | m \rangle = \sum_j c_j^m \langle b | V_{BM}^{el} | \phi_j \rangle \quad (2.35)$$

The theory developed in this section will be applied in chapter 7 where the role of the bridge length and its chemical connectivity will be analysed both at the DFT and at the tight binding level of theory, and we will point out how these two descriptions can complement each other. Indeed, phenomenological studies, such as those based on model Hamiltonians, are best suited to characterise the physics of a particular system, since the impact of different parameters and approximations on the results can be easily evaluated. For instance, specific limits of the model can be explored that could not be singled out in realistic systems, thus helping in the rationalisation of the experimental observation or in the interpretation of first principle calculations. Moreover, thanks to the limited computational demand, a more thorough investigation of the ‘chemical space’ can be carried out, allowing new physical phenomena to be identified; this task would be clearly impossible if the investigation was limited to selected few realistic examples. *Ab initio* methods, on the other hand, lie on the opposite side of the theoretical spectrum, with virtually no parameters required as input: these studies can bridge the gap between experimental outcome and microscopic description of the phenomenon, hence stimulating the interplay between theory and experiment.

2.5 Conclusions

In this chapter we have derived an expression for the charge recombination rate in dye sensitised solar cells. This expression will be validated against the experimental data available in the following chapters. The partitioning scheme employed for the interface will convey molecular insight into the mechanism of the main reactions in DSSCs, allowing the separate optimisation of the different molecular fragments that constitute the dye.

The connection between the theory of electron transfer and the bridge mediated transmission in molecular wires (that can be described within a scattering formalism similar to that used in this chapter) has been highlighted since the early day of the theoretical approach to these systems (see Ref. [106]). However, one of the main advantages of the formalism presented here is the seamless applicability to state of the art electronic structure calculations of the systems studied. The theory presented will be successfully validated against the experimental data for CRD (in the next chapter) and for CRE (in chapter 4). In both cases we apply equation (2.29) to the study of those molecular systems; hence proving the versatility of the proposed methodology; while equation (2.34), specifically designed to capture the contribution of the bridge fragment to the charge recombination, will be applied in chapter 7, where the design of an innovative type of bridge will be discussed.

2.6 Appendix

In this appendix we report the proof of equation (2.20) given in Ref. [94]. In the proof of the Mehler formula for the Hermite polynomials we will use the following

identity that can be proven using the saddle point approximation for complex integrands:

$$\frac{\sqrt{\pi}}{a} e^{-\frac{b^2}{4a^2}} = \int_{-\infty}^{+\infty} du \exp[-a^2 u^2 + ibu] \quad (2.36)$$

Setting $a=1$ and $b^2=4x^2$ in the previous expression the n -th order derivative of $\exp[-x^2]$ reads:

$$\frac{d^n}{dx^n} e^{-x^2} = \frac{(2i)^n}{\sqrt{\pi}} \int_{-\infty}^{+\infty} du u^n e^{-u^2 + 2iux} \quad (2.37)$$

This expression can then be employed to express the Hermite polynomial of order n :

$$H_n(x) \equiv (-1)^n e^{x^2} \frac{d^n}{dx^n} e^{-x^2} = \frac{(2i)^n e^{x^2}}{\sqrt{\pi}} \int_{-\infty}^{+\infty} du u^n e^{-u^2 + 2iux} \quad (2.38)$$

The Franck-Condon term as it is given in equation (2.19) can be evaluated by estimating the series:

$$S(x, y) = \sum_{n=0}^{\infty} t^n \chi_n(x) \chi_n(y) = \frac{\alpha}{\sqrt{\pi}} \sum_n \frac{t^n}{n! 2^n} e^{-\frac{\alpha^2}{2}(x^2+y^2)} H_n(\alpha x) H_n(\alpha y) \quad (2.39)$$

where the harmonic oscillator eigenfunctions have been expressed explicitly and $\alpha = \sqrt{\frac{M\omega}{\hbar}}$ is a scaling factor. Substituting equation (2.38) into the series $S(x, y)$ we obtain:

$$S(x, y) = \frac{\alpha}{\pi^{\frac{3}{2}}} \sum_{n=0}^{\infty} e^{-\frac{\alpha^2}{2}(x^2+y^2)} \int_{-\infty}^{+\infty} \int_{-\infty}^{+\infty} du dv \frac{(-2tuv)^n}{n!} e^{-u^2 + 2iaux} e^{-v^2 + 2iavy} \quad (2.40)$$

Carrying the summation under the integral sign and recognising the series expansion for the exponential function we can then exploit the identity (2.36) as follows:

$$\begin{aligned}
 S(x, y) &= \frac{\alpha}{\pi^{\frac{3}{2}}} e^{\frac{\alpha^2}{2}(x^2+y^2)} \int_{-\infty}^{+\infty} dv e^{-v^2+2i\alpha v y} \int_{-\infty}^{+\infty} du e^{-u^2+2iu(\alpha x+ivt)} \\
 &= \frac{\alpha}{\pi} e^{\frac{\alpha^2}{2}(x^2+y^2)} e^{-\alpha^2 x^2} \int_{-\infty}^{+\infty} dv e^{-v^2(1-t^2)+2iv(\alpha y-\alpha x t)}
 \end{aligned} \tag{2.41}$$

The second line in equation (2.41) can be further integrated with the change of variables: $v^2(1-t^2) = w^2 \Rightarrow dv = \frac{1}{\sqrt{1-t^2}} dw$:

$$\begin{aligned}
 S(x, y) &= \frac{\alpha}{\pi} e^{\frac{\alpha^2}{2}(x^2-y^2)} \frac{1}{\sqrt{1-t^2}} \int_{-\infty}^{+\infty} dw e^{-w^2+2iw\tilde{y}} = \\
 &= \frac{\alpha}{\sqrt{\pi(1-t^2)}} e^{\frac{\alpha^2}{2}(x^2-y^2)} e^{-\tilde{y}^2}
 \end{aligned} \tag{2.42}$$

With $\tilde{y} = \frac{\alpha}{\sqrt{1-t^2}}(y-xt)$ and where expression (2.36) has been employed again.

With some rearrangements the series reads:

$$S(x, y) = \frac{\alpha}{\sqrt{\pi(1-t^2)}} \exp \left\{ -\alpha^2 \left[\frac{x^2+y^2}{2} \left(\frac{1+t^2}{1-t^2} \right) - xy \frac{2t}{1-t^2} \right] \right\} \tag{2.43}$$

If we set $t = e^{-\beta\hbar\omega} = e^{-\theta}$ we can recast the Franck-Condon term in equation (2.19) as:

$$\begin{aligned}
F &= (M\omega^2\xi Q_l)^{-1} \sqrt{t} S(z, z) = \\
&= (M\omega^2\xi)^{-1} \frac{\alpha}{\sqrt{\pi}} \frac{2 \sinh(\frac{1}{2}\theta)}{\sqrt{2 \sinh(\theta)}} \exp \left\{ -\alpha^2 z^2 \left[\coth(\theta) - \frac{1}{\sinh(\theta)} \right] \right\} = \\
&= (M\omega^2\xi)^{-1} \frac{\alpha}{\sqrt{\pi}} \sqrt{\frac{\sinh(\frac{1}{2}\theta)}{\cosh(\frac{1}{2}\theta)}} \exp \left\{ -\alpha^2 z^2 \left[\frac{\cosh(\theta) - 1}{\sinh(\theta)} \right] \right\} = \\
&= (M\omega^2\xi)^{-1} \frac{\alpha}{\sqrt{\pi}} \frac{1}{\sqrt{\coth(\frac{1}{2}\theta)}} \exp \left[-\frac{\alpha^2 z^2}{\coth(\frac{1}{2}\theta)} \right]
\end{aligned} \tag{2.44}$$

where $z = -\frac{1}{2}\xi - \frac{1}{M\omega^2\xi}\Delta\mathcal{E}$ with individual quantities ξ and $\Delta\mathcal{E}$ previously defined in

Figure 4; basic properties of the hyperbolic functions have been used. Recalling the definition of reorganisation energy $\lambda \equiv \frac{1}{2}M\omega^2\xi^2$, the following quantities can be evaluated:

$$\begin{aligned}
\alpha^2 z^2 &= \frac{1}{\hbar\omega} \left(\frac{M\omega^2}{4} \xi^2 + \Delta\mathcal{E} + \frac{\Delta\mathcal{E}^2}{M\omega^2\xi^2} \right) = \frac{1}{2\lambda\hbar\omega} (\lambda + \Delta\mathcal{E})^2 \\
\frac{\alpha}{M\omega^2\xi\sqrt{\pi}} &= \frac{1}{\sqrt{2\pi\lambda\hbar\omega}}
\end{aligned} \tag{2.45}$$

By replacing these quantities into (2.44) one obtains the Franck-Condon term as expressed in equation (2.20).

Chapter 3: Evaluating charge recombination rate to dye⁺ from DFT calculations

3.1 Introduction

In this chapter and in the next we will validate the model developed in chapter 2 for the charge recombination reaction against the available experimental evidence. The computational procedure followed for the calculation of the parameters introduced in the previous chapter is reported. In particular, the reorganisation energy will be defined to include the changes in polarisation of the solvent following the electron transfer and the role of quantised molecular vibration will also be considered. Another important aspect, discussed in section 3.2.3.5, concerns the experimental input that will be employed in our model, which will affect the relative energy alignment of the levels shown in Figure 6 for a typical DSSC. We will show that the quantities required to estimate the charge recombination lifetime are rather diverse and this can possibly justify the lack of previous theoretical approaches to the study of the charge recombination kinetics, notwithstanding its practical importance.

This chapter is organised as follows: we give the theoretical background in section 3.2, where a more general expression for the Franck-Condon term is introduced to take into account an effective quantum vibration of the molecular system. The computational procedure adopted for the various quantities is reported in section 3.2.3. The comparison of the recombination lifetime (defined as the inverse of the charge recombination rate in equation (2.8)) with its experimental counterpart will be carried out in section 3.3 for the two families of dyes considered; the impact of the inaccuracies related to the parameters employed is also discussed.

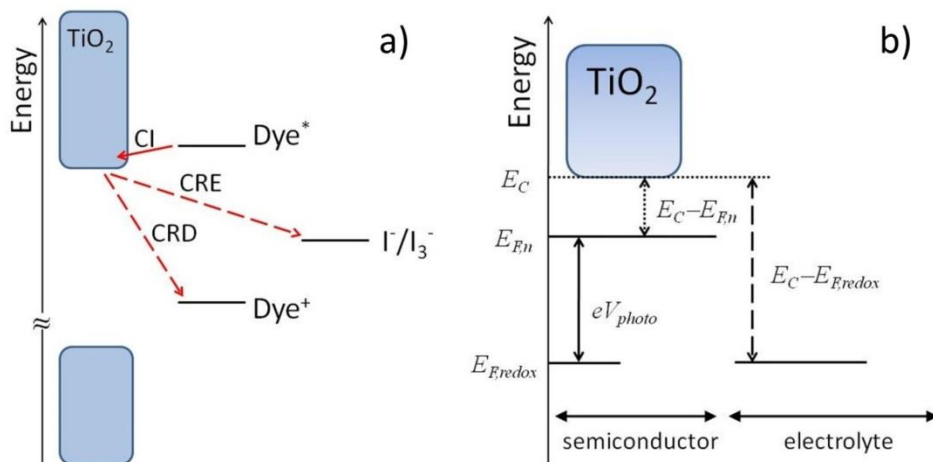


Figure 6. (a) Elementary processes taking place in a DSSC: charge injection (CI), charge recombination to electrolyte (CRE), charge recombination to oxidised dye (CRD). The horizontal lines represent effective one-electron energy levels. The coloured boxes represent the valence and conduction band of TiO_2 . (b) Alignment of energy levels E_C , $E_{F,n}$, $E_{F,redox}$ defined in the text. The energy differences eV_{photo} and $E_C - E_{F,redox}$ are affected by the experimental conditions and can be measured experimentally. The energy difference $E_C - E_{F,n}$ determines the concentration of electrons in the conduction band.

3.2 Theoretical background

In this section we recap for completeness the electron transfer theory previously exposed in chapter 2. The expression for the spectral density is adapted to the case of a non-orthogonal basis set and modifies equation (2.29), i.e. we will not partition the bridge contribution out of the semiconductor-molecule coupling. This treatment is consistent with the wide range of molecular structures considered that would make the partition between bridge and chromophore in the dye molecule somewhat arbitrary. Furthermore, we introduce in the Franck-Condon term the dependence on an effective quantum mode to evaluate the shortcomings of a purely classical

treatment of the molecular vibrations. The computational procedure for the quantities introduced is summarised in section 3.2.3.

3.2.1 Outline of charge transfer theory used in this chapter

The rate for charge recombination can be written as an integral over the possible energies of the electron in the semiconductor's conduction band [84]:

$$k = \int_{\text{conduction band}} \tilde{\Gamma}(E) f(E - E_F) F(\Delta G) dE \quad (3.1)$$

Since the charge recombination occurs under illumination the chemical potential in the Fermi-Dirac distribution (2.9) has been replaced by the *quasi*-Fermi level E_F , to highlight its dependence on the experimental conditions. The spectral density has been defined in equation (2.29) and it is reported here for convenience:

$$\tilde{\Gamma}(E) = \frac{2\pi}{\hbar} \sum_i |V_{if}|^2 \delta(E_i - E) \quad (3.2)$$

The Franck-Condon term in equation (3.1) has been reported in equation (2.11) and the approximations involved in its derivation have been discussed in section 2.3. Alternatively to the classical limit we will also employ a more general expression that accounts explicitly for nuclear changes involving modes with characteristic energy bigger than the thermal energy. An effective quantum mode with energy $\hbar\omega^{eff}$ is introduced that collects the quantum effect of all modes, and its energy, for organic conjugated molecules, is often taken to be $\hbar\omega^{eff} = 1400 \text{ cm}^{-1}$ [107, 108]. In this limit the Franck-Condon term reads:

$$F(\Delta G, \omega^{eff}) = \frac{1}{\sqrt{4\pi\lambda k_B T}} \sum_{\nu} e^{-S^{eff}} \frac{(S^{eff})^{\nu}}{\nu!} \exp\left[-\frac{(\Delta G - E + \lambda + \nu\hbar\omega^{eff})^2}{4\lambda k_B T}\right] \quad (3.3)$$

where S^{eff} is the effective Huang-Rhys factor for the effective quantum mode. The classical limit is appropriate if the dominant geometry changes during the electron transfer are due to the solvent reorganization (typically at very low frequency) while equation (3.3) has to be used if the intramolecular component of the reorganization energy is important (see section on reorganisation energy below).

Equation (3.1) is therefore a minor adaptation of the classical Marcus theory for interface electron transfer for the case of the semiconductor. This theory is normally used to rationalize the experimental results using an approximate evaluation of λ , experimental information on ΔG , and leaving $\tilde{\Gamma}(E)$ as a fitting parameter [109, 110]. The difference between dyes is, however, all in the detailed structure of $\tilde{\Gamma}(E)$ (describing the dye-semiconductor electronic coupling) and the Franck-Condon term F , so that it should be possible to compute the charge recombination rate from first principles and to rationalize the observed differences between dyes on the basis of their electronic and vibrational structure.

3.2.2 Limits of validity and relevance of the theoretical model

Any electron transfer theory is characterized by specific validity limits, and the expression described above was originally developed for cases when the electrons in the conduction band of the semiconductor are fully delocalized. This is not necessarily the case for DSSC where the potential importance of surface states [111], traps [68, 112] and excitonic interface states [113] has been suggested. It should be

noted that the formalism above can still be used *in principle* also for these cases: simply the $\tilde{\Gamma}(E)$ function is computed by extending the summation of equation (3.1) to these “special” states and the same expression of the rate will apply.

However, there is an important limitation. A key requirement for using non-adiabatic charge transfer theory is that the electronic coupling between initial and final state is sufficiently small (typically smaller than thermal energy). This condition is always satisfied for delocalized states (bulk or surface states), which have a vanishingly small coupling with the dye, also the use of a non-adiabatic picture for electron transfer is deemed acceptable given the smaller spatial extension of semiconductors’ surface orbitals in comparison with metals’ [114], which require a non-adiabatic description [87]. Furthermore, it is satisfied if the semiconductor hosts localized states few unit cells away from the dye (the effective coupling between the states localized on the dye and the traps decreases exponentially with the distance between them [115]).

A clear situation when the formalism above cannot be used is when there is a trap state in the immediate vicinity of the dye (e.g. every 1-2 TiO_2 unit cells). This is certainly possible but it may only involve a minority of dyes. Another source of localization at the interface is the formation of an interface exciton [113], i.e. a state where the electron is held close to the dye by the Coulomb interaction with its positive charge. This initial state can be incorporated in the formalism above only if the negative charge distribution is sufficiently large, so that the coupling with the dye becomes very small, a situation that is not modelled in this chapter. In chapter 8 the

role of the Coulomb interaction between the electron and a point-like charge across an interface will be examined and the induced electron localisation will be estimated.

In summary, the formalism reported herein is able to describe correctly the majority of the charge recombination events, even though in the application proposed in this chapter we will not consider the presence of traps, whose impact on the charge recombination is assessed in chapter 5; furthermore the specific model we considered does not include the presence of surface states. The modelling of charge transfer events in the case of strongly coupled initial and final states (adiabatic process) is, to some extent, simpler, as one could attempt studying it with standard transition state theory.

3.2.3 *Computational evaluation of the relevant quantities*

One of the often confusing aspects of the study of electro-chemical electron transfer rates using computational approaches is the unavoidable mixture between single electron (orbital) energy and wavefunction and multi-electron (state) energy and wavefunction, appearing in the same model. The theory in section 3.2.1 was formulated in terms of states, but it was implicitly assumed that the contribution to the total multi-electron energy given by an electron in a conduction band orbital with energy E was simply the orbital energy E , as it can be done only in the solid state. The total energy of a molecule is, of course, not the sum of the occupied orbital energies (because of Coulomb and exchange effects) so that the energy parameters related to the molecule are computed from a multi-electron wavefunction. Finally, as we are using a single electron picture for the semiconductor and a multi-electron picture for the molecular state, the coupling between them must be approximated with a single electron picture. If we assume that initial and final states can be

represented as Slater determinants differing only in the occupation of one electron, we can approximate:

$$V_{if} = \langle i | \hat{H} | f \rangle \approx \langle \varphi_i^S | \hat{F} | \varphi_{HOMO}^M \rangle \quad (3.4)$$

i.e. we assume that the only difference in the electronic configuration of the initial and final state is the transfer of an electron from the conduction band, occupying orbital φ_i^S in the initial state, to the HOMO orbital of the dye (φ_{HOMO}^M) in the final state. This approximation has been anticipated in section 2.2 and, as we point out therein, we are approximating the N -particle state on the molecular sensitizer in its final electronic configuration (i.e. after the electron transfer has occurred) with a single particle orbital. The \hat{F} operator is the relevant one-electron operator for the computational method adopted, typically the Kohn-Sham-Fock operator corresponding to the adopted density functional.

3.2.3.1 Dye-Semiconductor Coupling ($\tilde{\Gamma}(E)$)

To calculate $\tilde{\Gamma}(E)$, equation (2.29) must be expressed in a localised basis set, for example, as a linear combination of atomic orbitals: $\varphi_{HOMO}^M = \sum_m c_m \chi_m$ and $\varphi_i^S = \sum_k C_{ki} \phi_k$. Here, $\{\phi_k\}$ is the basis set for the semiconductor and $\{\chi_m\}$ is the basis set for the molecule, and indices k (or k') and m (or n) refer to the semiconductor's and the molecule's basis functions, respectively. Then, the coupling V_{if} , following equation (3.4), can be expressed via the coupling between localised basis functions of the molecule and localised basis functions of the semiconductor, $\{V_{mk}\}$, so that the expression for $\tilde{\Gamma}(E)$ becomes [56, 116]:

$$\tilde{\Gamma}(E) = \sum_{m,n} \Gamma_{mn}(E) c_m c_n^* \quad (3.5)$$

$$\Gamma_{mn}(E) = \frac{2\pi}{\hbar} \sum_i \sum_{k,k'} V_{mk} V_{nk}^* C_{ki} C_{k'i}^* \delta(E_i - E) \quad (3.6)$$

In equation (3.6), we can separate the terms that describe the semiconductor surface alone (basis set coefficients C_{ki}) and the terms that describe the interface between the semiconductor and the molecule (couplings V_{mk}). The former terms can be grouped together as the energy-dependent local density of states:

$$\rho_{kk'} = \sum_i C_{ki} C_{k'i}^* \delta(E - E_i) \quad (3.7)$$

Then, equation (3.6) becomes

$$\Gamma_{mn}(E) = \frac{2\pi}{\hbar} \sum_{k,k'} V_{mk} V_{nk}^* \rho_{kk'}(E) \quad (3.8)$$

If the basis set is non-orthogonal, equation (3.6) should be modified as follows [117]:

$$\Gamma_{mn}(E) = \frac{2\pi}{\hbar} \sum_{k,k'} (ES_{mk} - V_{mk})(ES_{nk'} - V_{nk'})^* \rho_{kk'}(E) \quad (3.9)$$

As discussed in Refs. [56, 116], the semiconductor-chromophore molecule system can be partitioned into three separate fragments: (i) the semiconductor surface, (ii) interface between the surface and the molecule's anchoring group, and (iii) the isolated chromophore molecule. Therefore, instead of calculating the whole semiconductor-chromophore system, the terms that describe the properties of the semiconductor surface (density of states matrix $\rho_{kk'}(E)$), the interface (couplings V_{mk})

and chromophore molecule (coefficients c_m) can be obtained from calculations of these fragments.

3.2.3.2 Electronic structure calculations of the dye-semiconductor interface

Density-functional theory calculations (using the SIESTA code [118]) of chromophores and the semiconductor surface were performed to obtain the input data for equations (3.5) and (3.9): the energies of Kohn-Sham states E_i , basis set coefficients C_{ki} and c_m , and matrix elements V_{mk} and S_{mk} . Generalized gradient approximation (GGA) and Perdew-Burke-Ernzerhof (PBE) exchange-correlation functional [119] were used, with Troullier-Martins norm-conserving pseudopotentials and a double- ζ polarized (DZP) basis set for all atoms (except for Ti semicore states, where a minimal basis set was used).

The TiO_2 semiconductor surface was modelled using anatase slabs exposing the (101) surface, the most commonly occurring surface in TiO_2 nanoparticles used in DSSC [7]. Four-layer anatase (101) slabs with the (1x3) surface unit cell were used, with the atoms in the bottom layer fixed at their bulk positions (a layer denotes a $(\text{TiO}_2)_2$ layer defined as in Ref. [61]). Benzoic acid was used as an anchoring group for all molecules considered, in its dissociated (bridging bidentate) adsorption configuration; this approximation has been tested previously [56]. Thinner anatase (101) slabs were also tested, and both three- and four-layer slabs produced very similar values of $\tilde{\Gamma}(E)$, showing that this slab thickness is sufficient to model the anatase (101) surface. The couplings V_{mk} , i.e. the elements of the Kohn-Sham matrix, were calculated at the Γ \mathbf{k} -point. This choice of \mathbf{k} -points reflects the situation where

a single adsorbed molecule is interacting with a semiconductor, rather than a periodic array of molecules, as explained in [56].

To calculate the energy-dependent density of states $\rho_{kk'}(E)$, we sampled the Brillouin zone using a range of **k**-point densities. The density of the **k**-point grid was controlled by the **k**-grid cutoff parameter in SIESTA (equal to half the length of the smallest lattice vector of the supercell required to obtain the same sampling precision with a single **k**-point [120], which varied between 0 (only the Γ point) and 30 Å (132 **k**-points). We found that the **k**-point grid cutoff of 10 Å (which gives 4 **k**-points per cell) gives converged plots of $\tilde{\Gamma}(E)$ and converged values of recombination times. Equation (3.7) therefore has been adjusted to include averaging over **k**-points:

$$\rho_{kk'}(E) = \frac{1}{N_p} \sum_p \sum_i C_{ki}(p) C_{k'i}^*(p) \delta(E - E_i) \quad (3.10)$$

Where the index p refers to different **k**-points and N_p is the total number of **k**-points. A Gaussian broadening of 0.05 eV was used to approximate the Dirac delta function $\delta(E - E_i)$. A plot of $\tilde{\Gamma}(E)$ for several dyes, compared with the density of states for the TiO₂ slab with the benzoic acid adsorbate, is presented in section 3.3.

Isolated chromophore molecules (oriented in the same way as the adsorbed anchoring group in the TiO₂-anchoring group system) were simulated separately, also using the PBE functional. The coefficients c_m obtained in these calculations were then used in equation (3.5). Further details can be found in Refs. [56, 61].

3.2.3.3 Dye's free energy change

Part of the driving force for the charge recombination is related to the energy difference between the oxidized and neutral configurations of the dye. Also, since the molecular system is surrounded by a polar solvent which is highly responsive to the chromophore oxidation state, the energy difference between the two states will be affected by the solvent rearrangement; hence it is necessary to include this effect in the computational scheme. To this end, *ab initio* quantum mechanical calculations were performed within the polarisable continuum model (PCM) framework [121]. This implicit solvation model has been extensively used to study electronic properties of organic molecules, including DSSC chromophores, e.g. [122, 123]. In this model the solvent is considered as an isotropic continuum characterized by a value of the dielectric constant and the molecule is placed in a cavity within this continuum.

The *ab initio* calculations were performed with Gaussian 03 [124] at the DFT 6-31G (d, p) level of theory with the hybrid B3LYP exchange-correlation functional. The default PCM [121] model has been adopted, with the solvent parameters of acetonitrile (the solvent of most DSSC) and solvent cavity defined by the UAKS model [125]. The energies of the dyes optimized in their neutral and positively charged states were used to compute the free energy difference ΔG between the two states, which is identical to the internal energy difference in the harmonic approximation implicit in equations (2.11) and (3.3).

3.2.3.4 Reorganisation energy

The reorganisation energy for a charge transfer process has been defined by Marcus in one of his seminal papers [126]. In order to take into account the presence

of non-classical vibrational modes, the reorganisation energy is partitioned into two additive contributions, namely the external component (λ_{ext}) arising from solvent rearrangement upon electron transfer and the internal component (λ_{int}) due to internal molecular vibrations. The computational scheme followed for the latter component is based on the definition [107]:

$$\lambda_{int} = \sum_j \hbar \omega_j S_j \quad (3.11)$$

where the summation runs over the internal vibrations of frequency ω_j , and S_j is the corresponding Huang-Rhys factor that is computed from the equilibrium displacement between the optimized geometry for the neutral and charged species as described in Ref [127]. For the chromophores considered in this chapter the frequencies have been calculated using Gaussian 03 at the 6-31G (d,p)/B3LYP level of theory for the neutral geometry optimized within the PCM framework (see above). The external component of the reorganization energy is evaluated as:

$$\lambda_{ext} = \frac{1}{2} \left(E^{(1)}(M^{+\bullet}) - E^{(0)}(M^{+\bullet}) \right) + \frac{1}{2} \left(E^{(1)}(M) - E^{(0)}(M) \right) \quad (3.12)$$

where E indicates the total electronic energy of the particular electronic configuration: neutral molecule (M) or charged molecule ($M^{+\bullet}$). The optimized geometry of the neutral molecule is used in the calculations of all these energies. The superscript refers to the polarization of the continuum dielectric used to model the surrounding solvent. $E^{(0)}(M)$ and $E^{(0)}(M^{+\bullet})$ indicate that the energy has been evaluated with the solvent polarization that stabilizes the neutral and positively charged molecule respectively, i.e. a routine electronic structure calculation with

PCM. $E^{(1)}(M)$ and $E^{(1)}(M^{+\bullet})$ indicate that the energy has been evaluated with the solvent polarization that stabilizes positively charged and neutral molecule respectively, i.e. not the state for which the energy is computed. This is done by employing a vertical solvation version of the PCM framework which will account for the Pekar factor $c_0 = 1/\varepsilon_\infty - 1/\varepsilon_s$, where ε_∞ and ε_s are the high-frequency and static dielectric constants respectively (for acetonitrile $c_0 = 0.526$). This procedure has been tested in Refs [128–130].

When the classical limit expression is used, the appropriate reorganization energy to include in the formula is the sum of the internal and external components. When one uses the expression with an effective quantum mode (equation (3.3)), known as Jortner equation, only the external component λ_{ext} should be used in place of λ . The internal component enters in equation (3.3) through the effective Huang-Rhys factor computed as $S^{eff} = \lambda_{int}/\hbar\omega^{eff}$. This partitioning scheme for the reorganisation energy plays a role in the evaluation of the Franck-Condon term. In particular, when the quantum modes are explicitly taken into account, only the external component of λ ought to be considered, whereas in the classical expression (2.11) the sum of the two is typically employed.

Furthermore, the Marcus analysis for the electron transfer was derived for acceptor/donor couples completely surrounded by solvent, similarly the PCM scheme assumes the presence of a uniform dielectric continuum outside the molecular cavity; this is clearly not the case for the recombination process at the dye-semiconductor interface, where only part of the dye molecule is exposed to the solvent. Following a theoretical study of electron transfer at metal-solution interfaces

[131], we set the value of λ_{ext} equal to one-half of the value computed as described above, while assuming that the internal component is not affected by the presence of the nanostructured electrode. The numerical values for the systems considered are reported in Table 1. The effect of the uncertainty of the reorganization energy on the computed rate is discussed in the next section.

Table 1. Reorganisation energies (calculated as a sum of the internal reorganisation energy and the external reorganisation energy multiplied by a factor of 0.5: $\lambda = \lambda_{int} + \lambda_{ext} \times 0.5$) and free energy differences for the dyes in Figure 7.

Dye	λ/eV	λ_{int}/eV	$\Delta G/\text{eV}$
OH1	0.436	0.1026	-4.79
OH2	0.406	0.0782	-4.80
OH4	0.426	0.0911	-4.87
OH17	0.408	0.0798	-4.78
NKX2311	0.424	0.0788	-5.20
NKX2587	0.415	0.0845	-5.10
NKX2677	0.404	0.0979	-4.91
NKX2697	0.397	0.1106	-4.78

Note that two different electronic structure methods (SIESTA and Gaussian 03 calculations) were used to obtain the electronic properties of TiO₂ surfaces (with chromophore anchoring groups) and isolated dyes and dye cations. The reason for using two different methods was that these methods offer different necessary functionalities: periodic boundary conditions in SIESTA are needed for an accurate description of the TiO₂ surface, while the implicit solvent model present in Gaussian 03 is essential for incorporating solvent effects in the calculations of ΔG and λ . The two calculations made using these two methods are effectively decoupled, i.e. one is used only to obtain the values of $\tilde{\Gamma}(E)$ and the other to obtain terms for calculating the Franck-Condon term.

3.2.3.5 Alignment of molecular and solid state levels and (*quasi*) Fermi level

To evaluate the integral in equation (3.1) we need the absolute value of the energy of the conduction band minimum (CBm), E_C , for the TiO_2 electrode in contact with the electrolyte. This property cannot be obtained using quantum-chemistry calculations, because the semiconductor's energy levels are shifted as a result of its interaction with the electrolyte [66]. Very few experimental estimates of E_C exist for a limited number of experimental set-ups, e.g. for a TiO_2 electrode immersed in a water solution at pH 1 [132]. Another important characteristic of this system, which is also controlled by the semiconductor-electrolyte interaction, is the difference between E_C and the Fermi level of TiO_2 , E_F , which determines the concentration of electrons in the conduction band (via the Fermi-Dirac term in equation (3.1)). Below we discuss the electrochemical properties of the cell and our choice of the values for E_C and $E_C - E_F$.

Because a DSSC is a photoelectrochemical cell, its electrochemical parameters depend on the flux of incoming photons. Charge recombination, in particular, is significantly large only at high light intensities near open circuit potentials [133].

Under the conditions of no illumination, the energy alignment in a DSSC is straightforward: the Fermi levels of the electrolyte in solution ($E_{F,redox}$) and of the electrons ($E_{F,0}$) in the TiO_2 electrode equilibrate to a common value. The conduction band minimum in the dark was measured to be 0.1 eV above the Fermi level [134]. Upon illumination, the presence of photoinjected electrons modifies the electron population in the semiconductors, creating a photopotential (V_{photo}), which represents

the maximum energy attainable from the device. The energy levels diagram for the semiconductor-electrolyte interface under illumination is shown in Figure 6b. The steady-state electron distribution in these conditions is characterized by a value of the *quasi*-Fermi level ($E_{F,n}$) which is immediately related to the photopotential via $eV_{photo} = E_{F,n} - E_{F,redox}$. This energy difference can be measured experimentally [39, 135].

The offset between the conduction band minimum and the *quasi*-Fermi level, $E_C - E_{F,n}$, is a function of the operating conditions at which the particular experiment is carried out. The factors that control $E_C - E_{F,n}$ and therefore E_C include the solvent viscosity, electrolyte concentration and presence of additives [136]. These factors are not included in the quantum-chemical modelling of the surface, which also suffers from the known inaccuracy of the DFT method in the determination of the virtual orbitals' energy levels. Therefore, we decided to use the experimental value of E_C instead of the DFT calculated one, as this allows a better evaluation of how all other parameters affects the computation of the recombination rate and because the accurate determination of value of E_C is a somewhat separate computational problem.

The experimental quantities that are known with the greater accuracy are $E_{F,redox}$ and eV_{photo} , which allow us to obtain $E_{F,n}$. The Fermi level for the redox couple, for instance, can be determined by $E_{F,redox}[eV] = (-4.6 \pm 0.1) - eV_{redox}[V]$ [7] where V_{redox} is the potential of the redox couple. Using the Nernst equation for the redox couple as in Ref. [7] and the typical concentrations of iodide and triiodide in DSSC electrolytes given in Ref. [31] ($[I^-] = 450 \text{ mol dm}^{-3}$, $[I_3^-] = 50 \text{ mol dm}^{-3}$), we

calculate $E_{F,redox}$ to be -4.77 eV. For the operating conditions used in Ref. [137] (applied potential = 0.6 eV), the corresponding value of $eV_{photo} = 0.63$ eV can be obtained from the data in the review [133]. Therefore, $E_{F,n}$ can also be obtained. We consider $E_{F,redox}$, eV_{photo} and $E_{F,n}$ as fixed at their experimental values and we allow E_C to vary between -4.1 eV to -3.7 eV, compatibly with the experimental range of $E_C - E_{F,redox}$ presented in Ref. [136].

We use this range of E_C values and the corresponding difference $E_C - E_{F,n}$ is used to calculate the Fermi-Dirac distribution $f(E - E_{F,n})$. To calculate $\tilde{\Gamma}(E)$, which is evaluated over a set of energy levels in and just below the conduction band, we shift the computed conduction band edge to align it with the adjustable parameter E_C . As a result, we obtain recombination rate k (and its inverse, recombination time τ_{rec} , which can be compared with experiment) for a range of realistic E_C values.

3.2.3.6 Molecular systems considered in this chapter

The dyes considered are a set of coumarin derived chromophores (the NKX family NKX2311, NKX2587, NKX2677 and NKX2697, shown in Figure 7), whose recombination times were studied in Refs. [138, 139]. NKX2677 has been a subject of intense research because of the particularly high efficiency shown (8% [140]) which is very close to the maximum efficiency attained with an organic sensitizer (9% [109]). This class of compounds is very well suited to explore the role of the oligothiophene moiety, which has been identified as the molecular portion which localizes the positive charge density (hole) once the electron transfer has taken place [138]. At the same time, the newly synthesized benzofuro-oxazolo-carbazolo type of

dyes introduced by Ooyama et al. [137] (the OH family, OH1, OH2, OH4, OH17 in Figure 7) provides an interesting set of recombination lifetimes, spanning almost three orders of magnitude (μs to ms) for molecules with similar structures.

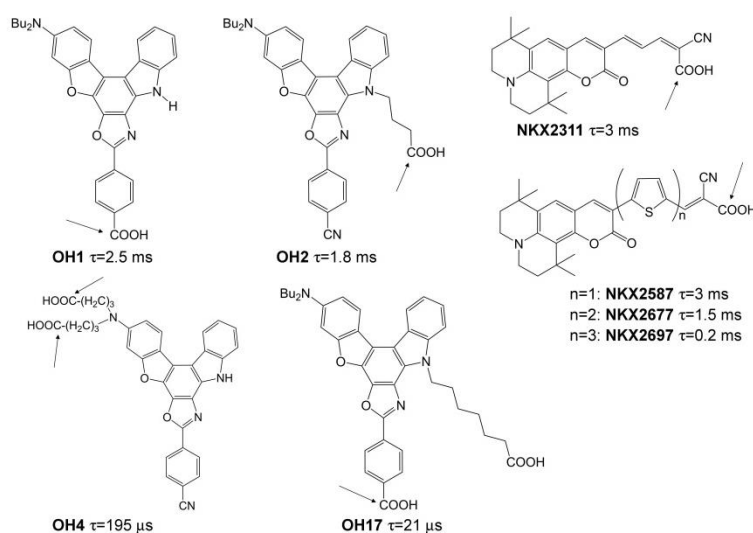


Figure 7. Chemical structures and experimental recombination times for the molecular systems considered. Arrows indicate the anchoring group attached to the semiconductor surface.

3.3 Results and discussion

In this section we calculate the recombination lifetimes as given by our model for the NKX and OH families of dyes, and their dependence on the position of the conduction band minimum and on the calculated values of ΔG and λ .

3.3.1 NKX series of dyes

Figure 8 shows recombination times for the NKX dyes, together with the terms that contribute to equation (3.1) for the recombination rate: the substrate-dye

coupling weighted by the density of states, $\tilde{\Gamma}(E)$, and the Franck-Condon term, $F(\Delta G - E)$.

We start by discussing the dyes' $\tilde{\Gamma}(E)$, plotted in the top panel of Figure 8: the relative ordering of the dyes' $\tilde{\Gamma}(E)$ is $\text{NKX2311} > \text{NKX2587} > \text{NKX2677} > \text{NKX2697}$ (which is opposite to the ordering of the dyes' recombination rates). This ordering of $\tilde{\Gamma}(E)$ can be understood by analysing the different terms that enter the equation for $\tilde{\Gamma}(E)$. According to equations (3.5) – (3.9), $\tilde{\Gamma}(E)$ is proportional to the semiconductor density of states $\rho_{kk}(E)$, the semiconductor-dye coupling V_{mk} and the dye's HOMO coefficients c_m ; note that only the c_m coefficients belonging to the anchoring (carboxylic) group contribute significantly to $\tilde{\Gamma}(E)$, because the V_{mk} values are large only for the dye atoms that belong to the anchoring group. This is also confirmed by the insert in the top panel of Figure 8, where the state contributing to the spectral density near the conduction band minimum is localised on the semiconductor's surface in proximity of the anchoring group. Because of the structural rigidity of the NKX molecules, we can reasonably assume that all four of these molecules are adsorbed on TiO_2 in the same configuration: via their carboxylic group and oriented perpendicular to the surface. For dye adsorbates with a similar chemical nature and similar adsorption chemistry, the density of states and semiconductor-dye coupling terms in equation (3.9) will be the same or similar for all the dyes, and only the HOMO coefficients will differ depending on the details of the dyes' structure. The HOMO of the NKX dyes is mainly localised on the molecules' coumarin core, therefore, in the NKX series, the dye with the longest

polythiophene chain (NKX2697) has the lowest weight of the HOMO on the carboxylic group and hence the lowest $\tilde{\Gamma}(E)$. As the length of the polythiophene chain decreases in the order NKX2697 > NKX2677 > NKX2587 > NKX2311 and the distance between the anchoring group and the coumarin core decreases, the weight of the HOMO on the anchoring group increases. This explains the increase of the calculated $\tilde{\Gamma}(E)$ in the order NKX2311 > NKX2587 > NKX2677 > NKX2697.

At the same time, this sequence of $\tilde{\Gamma}(E)$ does not reproduce the correct ordering of the recombination rates as given by the experiment (NKX2311 \approx NKX2587 \leq NKX2677 < NKX2697). The nuclear motion factor and the relative energies of the neutral dye and its cation (described by the Franck-Condon term $F(\Delta G-E)$) need to be taken into account.

The NKX dyes' Franck-Condon terms $F(\Delta G-E)$, defined in equation (2.11), are shown in the middle panel of Figure 8. The dye with the $F(\Delta G-E)$ maximum occurring at the highest energy (closest to CBm) is the largest molecule, NKX2697, and the dye with the $F(\Delta G-E)$ maximum at the lowest energy is the smallest molecule, NKX2311. This ordering agrees with the systematic variation in free energy change ΔG for these dyes, as reported in Table 1. The value of ΔG is the energy of the dye cation relative to the neutral dye; the cation form is most effectively stabilized in the largest NKX2697 dye, therefore ΔG is the smallest for this dye and the $F(\Delta G-E)$ maximum for this dye occurs closest to the CBm. Therefore, at the energies close to the conduction band edge (i.e. the energies in the conduction band with the largest electron population), the NKX2697 dye and the

smallest NKX2311 dye have the highest and lowest values of $F(\Delta G-E)$ respectively.

This ordering of the $F(\Delta G-E)$ curves' maxima agrees with the measured recombination times [138, 139] presented in Figure 7.

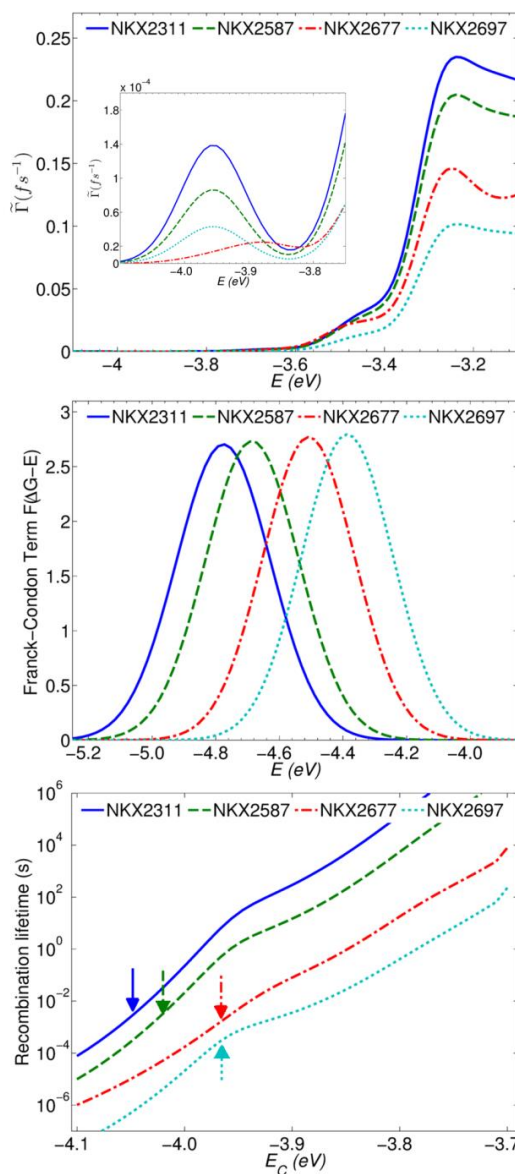


Figure 8. Calculated recombination properties of the NKX dyes. Top panel: spectral density for the dyes, conduction band edge has been set equal to -4.0 eV. Middle panel: Franck-Condon terms. Lower panel: calculated recombination lifetimes for the NKX dyes as a function of the CBm energy. Arrows indicate the data points where the calculated recombination times match experimental recombination times for the corresponding dyes.

The differences between the dyes' $F(\Delta G-E)$ are much larger than the differences between their $\tilde{\Gamma}(E)$ in the energy interval of interest. For example, the ratio of the $\tilde{\Gamma}(E)$ values for the NKX2697 and NKX2311 dyes is 0.38 at the energy 0.2 eV above the CBm, while the ratio of these dyes' $F(\Delta G-E)$ at this energy is $\approx 6 \times 10^5$. At the energy 0.1 eV above the CBm, the ratio of these dyes' $\tilde{\Gamma}(E)$ values is 0.31 and the ratio of their $F(\Delta G-E)$ values is 1×10^5 . Thus, the Franck-Condon term is the dominant term determining the ordering of these dyes' recombination rates, and is more important than the relative $\tilde{\Gamma}(E)$ values for this family of dyes.

The recombination lifetimes, $1/k$, calculated for a range of possible values of E_C , the energy of the conduction band minimum, and using the temperature $T = 298$ K for the Fermi-Dirac distribution, are shown in the lower panel of Figure 8 for the NKX family. The dyes display a strong dependence of recombination times on the value of E_C (approximately two orders of magnitude change in recombination times for a 0.1 eV variation in E_C). The ordering observed for the NKX family is in agreement with the experimental ranking reported in the literature (Figure 7 and Refs. [138, 139]): recombination times decrease in the order NKX2311 > NKX2587 > NKX2677 > NKX2697. The comparison with the experimental window of recombination lifetimes (0.2-3.0 ms; the experimental values of recombination times are shown by arrows in Figure 8) allows us to identify the range for the CBm that gives calculated lifetimes in agreement with the experimental data: this spans an energy range of approximately 0.1 eV, between -4.05 and -3.95 eV, well within the range of values attainable in experiment [136]. In summary, our model gives a

reliable description of recombination times of the NKX series of dyes: the fast-to-slow ordering of recombination times is the same as in experiment, and the absolute values of recombination times also agree with experiment in a realistic range of conduction band energies.

3.3.2 *OH family of dyes*

The three panels of Figure 9 show the energy dependence of the $\tilde{\Gamma}(E)$ term, the Franck-Condon term $F(\Delta G-E)$ and the recombination times for the OH series of dyes. These dyes have a complex chemical structure, with non-systematic variations between the molecules belonging to this series, and their measured recombination rates [137] do not show an intuitively understandable pattern. Below, we analyse the different factors that affect the OH dyes' recombination efficiency.

First, we consider the coupling term $\tilde{\Gamma}(E)$, plotted in the upper panel in Figure 9 (in case of the flexible OH2 and OH4 dyes, we plot the curves for one selected conformation for each of the dyes – the conformation labelled (1) in Figure 10 for OH2, and the conformation labelled (1) in Figure 11 for OH4). We find no clear and systematic ordering of the OH dyes' $\tilde{\Gamma}(E)$.

It is difficult to explain these molecules' ordering, although we can attribute some features shown in Figure 9 to the dyes' chemical structure. The OH1 dye can be considered as a reference because it has the simplest structure in this series, with a rigid geometry and only one anchoring group for binding to the surface. Several of the remaining OH dyes have more than one functional group near the TiO_2 surface, and either or both of these groups may be bonded to the surface (e.g. dyes OH4 and OH17).

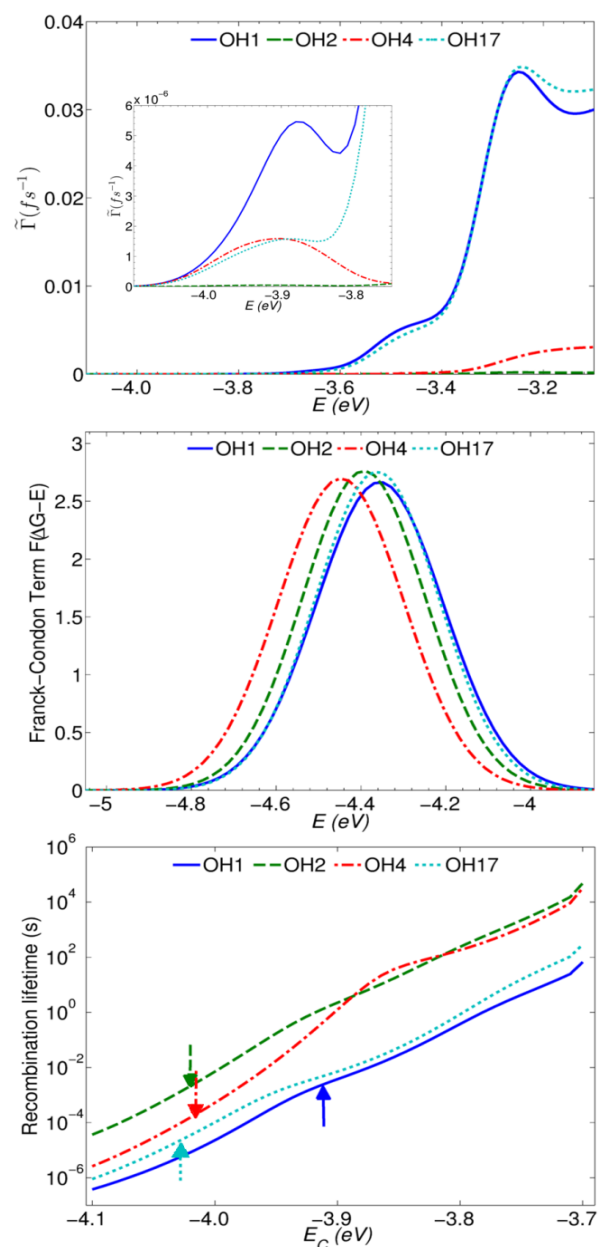


Figure 9. Calculated recombination properties of the OH dyes. Top panel: spectral density; conduction band edge has been set equal to -4.0 eV. Middle panel: Franck-Condon terms. Lower panel: calculated recombination lifetimes for the OH dyes as a function of the CBm energy. Arrows indicate the data points where the calculated recombination times match experimental recombination times for the corresponding dyes.

In the OH dyes, we can also see several competing factors that affect the coupling of their HOMO to the semiconductor states in opposite ways: proximity of the anchoring group to the aromatic core vs. the conjugation in the linker group

connecting the anchoring group to the core. For example, in the OH2 and OH4 chromophores, the carboxylic anchoring groups are close to the location of the dye's HOMO (see Figures in Ref. [137]), where the cation's positive charge is localised. Therefore, the weight of the HOMO on the anchoring groups is rather large and provides relatively large $\tilde{\Gamma}(E)$ (as seen for the OH4 dye in the part of the curve close to the conduction band edge). On the other hand, in the OH1 and OH17 dyes, the anchoring group is connected to the aromatic core via an aromatic linker, rather than via a saturated alkyl linker; this aromatic linker provides stronger conjugation and therefore stronger coupling of the anchoring group with the HOMO than the alkyl linker in the OH2 and OH4 dyes. This factor explains consistently large $\tilde{\Gamma}(E)$ values for OH1 and OH17 in the whole interval of energies considered here.

An additional complication for the OH2 and OH4 dyes is that the flexible alkyl linkers between the anchoring groups and the aromatic part of these molecules give rise to many possible co-existing conformations. We found that different conformations of the alkyl chains can produce very different $\tilde{\Gamma}(E)$, and the difference between the $\tilde{\Gamma}(E)$ curves for different conformations of the same molecule can be comparable with the difference between the $\tilde{\Gamma}(E)$ curves for different molecules. The OH2 dye is the most dramatic example: depending on the conformation, its $\tilde{\Gamma}(E)$ in the low-energy region, shown in the insert in Figure 9, can be either largest or the smallest among all the OH dyes.

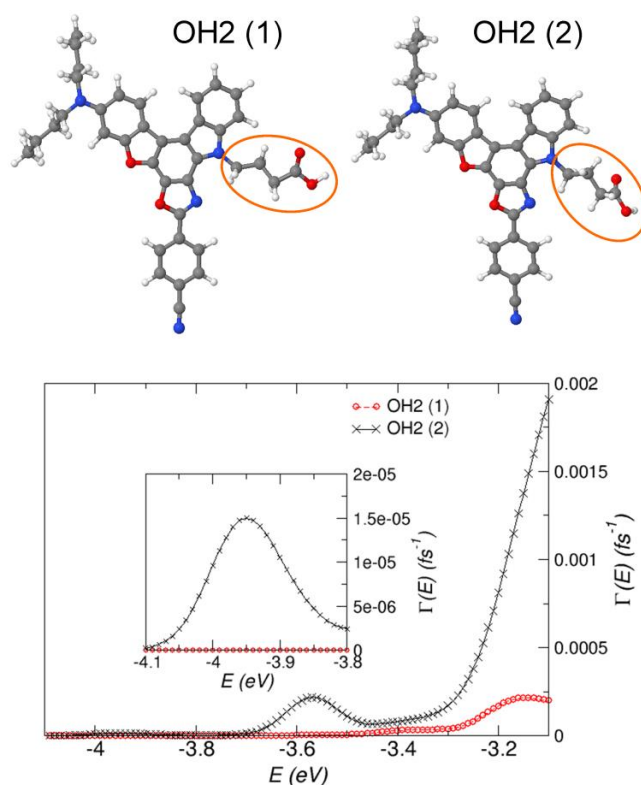


Figure 10. Spectral density of the OH2 dye, using two different conformations of the alkyl chains connecting the two anchoring groups to the dye's aromatic core.

Figure 10 shows two possible conformations of the OH2 dye, which differ by the torsional angles of the alkyl chain (more conformations can be constructed in a similar way, with the only restriction that the conformations should be compatible with the anchoring group adsorption on a surface). We found that the $\tilde{\Gamma}(E)$ values correlate with the magnitude of the coefficients c_m of the dye's HOMO: e.g. conformation (1) has small values of c_m coefficients for basis functions localized on the carboxylic O and C atoms, and it has low $\tilde{\Gamma}(E)$ values; conformation (2) has large c_m values and large $\tilde{\Gamma}(E)$ values. Taking into account that the chemical structure of both conformations is the same, we attribute this difference in c_m

coefficients to the different strength of through-space (rather than through-bond) coupling between the anchoring group and the molecule's HOMO region.

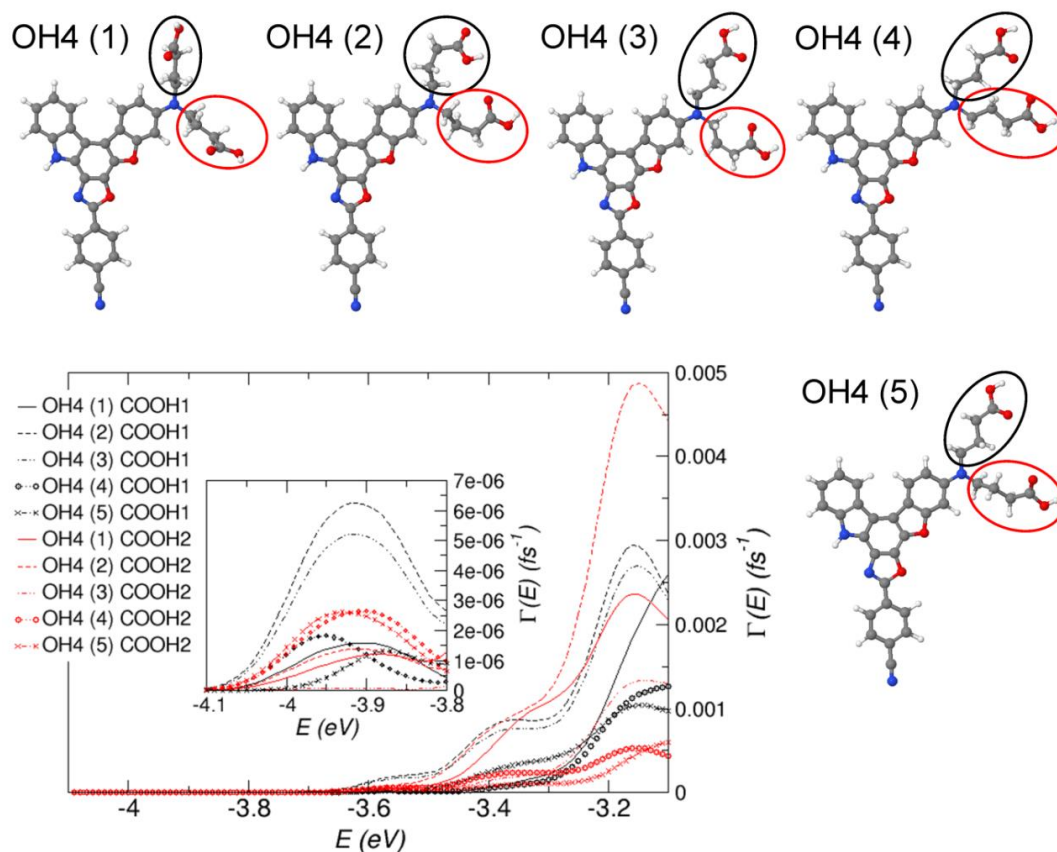


Figure 11. Spectral density of the OH4 dye, using five different conformations of the alkyl chains connecting the two anchoring groups (COOH1 and COOH2, circled in black and red respectively) to the dye's aromatic core. Conformation (1) and anchoring group COOH1 were used for the calculations of recombination times.

Five different conformations of the OH4 dye and the corresponding $\tilde{\Gamma}(E)$ curves are shown in Figure 11. For this dye as well, $\tilde{\Gamma}(E)$ depends on the conformation and is strongly correlated with the magnitude of the c_m coefficients of the carboxylic O and C atoms. As a summary, there is not a single $\tilde{\Gamma}(E)$ function for dyes with a flexible structure, such as OH2 and OH4. Because of the flexibility of the alkyl

chains, many conformations for such dyes, with different c_m coefficients and different $\tilde{\Gamma}(E)$ values, are likely to co-exist in a real DSSC system. The success of a computational prediction of such molecules' recombination times will depend on the ability to predict the conformation (or the distribution of conformations) in a densely packed monolayer, i.e. including the inter-molecular interaction. Finally, we note that the $\tilde{\Gamma}(E)$ values for the OH dyes are almost an order of magnitude smaller than the values for the NKX dyes.

The $F(\Delta G-E)$ curves for the OH family are presented in the middle panel of Figure 9. In contrast to the situation for the NKX family, the $F(\Delta G-E)$ curves for the OH dyes lie fairly close to each other (the OH1 curve has its maximum closest to the CBm), and the difference in these dyes' recombination rates arising from the difference in their $F(\Delta G-E)$ values is likely to be small. Thus, unlike the NKX family, recombination rates in the OH family are controlled by the dyes' spectral densities. The molecular orbital localisation provides an immediate explanation of this fact: the HOMO orbital (and therefore the ionization energy and the recombination free energy change ΔG) is heavily modified along the NKX series, while it remains almost unchanged for the OH series. This analysis illustrates how theory can disentangle the different contributions to the recombination rate and that, unfortunately, for different systems the rate is modulated by different system parameters.

Finally, we consider the OH dyes' recombination times, presented in the lower panel of Figure 9. For the OH family, the experimental sequence of recombination times (slowest to fastest) is OH1 > OH2 > OH4 > OH17. By comparison, in our

calculation, we obtain the sequence $\text{OH2} > \text{OH4} > \text{OH17} \geq \text{OH1}$ for low values of the conduction band edge; this ordering is partially modified for $E_C \approx -3.85$ eV where the values of $\tilde{\Gamma}(E)$ for OH2 and OH4 practically coincide (as shown in the insert in Figure 9, top panel). Noticeably, chromophores OH1 and OH17, which are reported in the experiment [139] as the extrema of the series (slowest and fastest, respectively), in our calculations show recombination lifetimes almost identical to each other, in disagreement with experiment. The theoretical result is not unexpected: these two molecules are so similar in chemical and electronic structure that their electron recombination properties are bound to come out similar in a calculation that has electronic structure calculation as input. To explain the observed difference between OH1 and OH17, we need to invoke a mechanism that goes beyond the electronic structure results.

An explanation for the very different recombination rates of OH1 and OH17 can be suggested on the basis of the results in the lower panel of Figure 9. The calculated recombination times for three dyes, OH2, OH4 and OH17, agree with the experimental recombination times when the CBm energy is in a very narrow interval, -4.03 - -4.01 eV. On the other hand, to achieve the experimental recombination time for the OH1 dye (2.5 ms), we should assume that the CBm is higher in this case by about 0.1 eV. The assumption that the CBm take a single value for a family of dyes is justified only if the structure of the monolayer for the family of dyes is similar, because the semiconductor's conduction band shifts up or down depending on the magnitude and direction of the adsorbate's dipole moment and density of coverage [141]. For example, dye OH1, which has only one anchoring group and does not

contain any bulky alkyl chains, will likely form dense monolayers of upright-oriented molecules. The other three dyes, OH2, OH4 and OH17, are more likely to adsorb on the surface in non-upright configurations, with their bulky alkyl groups preventing close packing between molecules. This may be sufficient to alter the surface dipole and to cause a small shift of CBm for OH1 which would explain the anomaly. A rigorous demonstration of this mechanism cannot be reached here as it would require a different set of modelling tools, but a simple conclusion that can be agreed simply by inspecting OH1 and OH17 is that their very different recombination time is neither due to their different electronic structure nor to their different coupling to the electrode.

This result points to a limitation of our scheme: when we compare recombination times in a range of CBm energies, we imply that the CBm position is the same for all the adsorbed dyes. The CBm energy in an electrochemical system depends on many variables, as discussed at the end of the Method section, and is taken as a parameter in our computational scheme. Thus, our method is reliable only if the dyes' adsorption characteristics (density, orientation) are fairly similar. The existence of different conformations for the OH2 and OH4 dye further complicates the prediction in the absence of a detailed model for the monolayer.

3.3.3 Effect of uncertainties in the computational parameters on recombination lifetimes

The impact of uncertainty in the reorganisation energy on the calculated recombination times is shown in Figure 12. We can see that an increase of 0.1 eV in the total reorganisation energy (which corresponds to roughly $\pm 25\%$ of the total value) causes a two orders of magnitude variation (one order of magnitude for the

OH1 dye) in the calculated recombination lifetimes, but the values of recombination lifetimes are still consistent with the experiment within the window of allowed values for the conduction band edge. On the other hand, a similar decrease in the reorganisation energy produces a bigger variation for the recombination lifetimes (four and two orders of magnitude respectively); hence we can conclude that minor variations in the reorganisation energy will not affect the computational output.

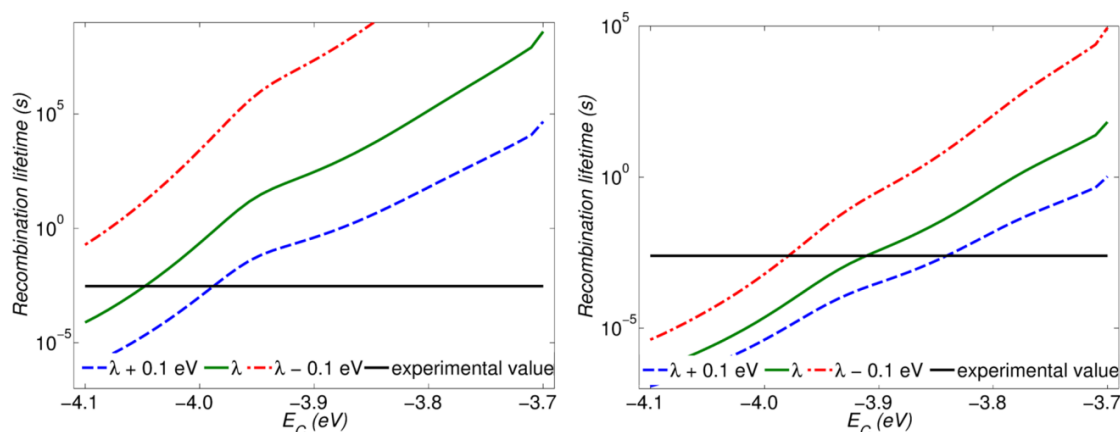


Figure 12. The effect of uncertainty in the value of λ on the recombination lifetime (plotted as a function of the conduction band minimum position): the broken lines correspond to $\lambda + 0.1$ eV and $\lambda - 0.1$ eV, for the chromophores NKX2311 (left panel) and OH1 (right panel).

The relevance of an accurate evaluation of the reaction driving force ΔG has been examined in Figure 13: the introduction of an uncertainty on ΔG of ± 0.1 eV produces a variation in the recombination lifetime of roughly one order of magnitude with respect to the recombination lifetime computed using the driving force in Table 1. We observe that by making the driving force more negative (i.e. by further reducing the stability of the cation with respect to the neutral molecule) the reaction is slowed down, consistent with the inverted Marcus region behaviour.

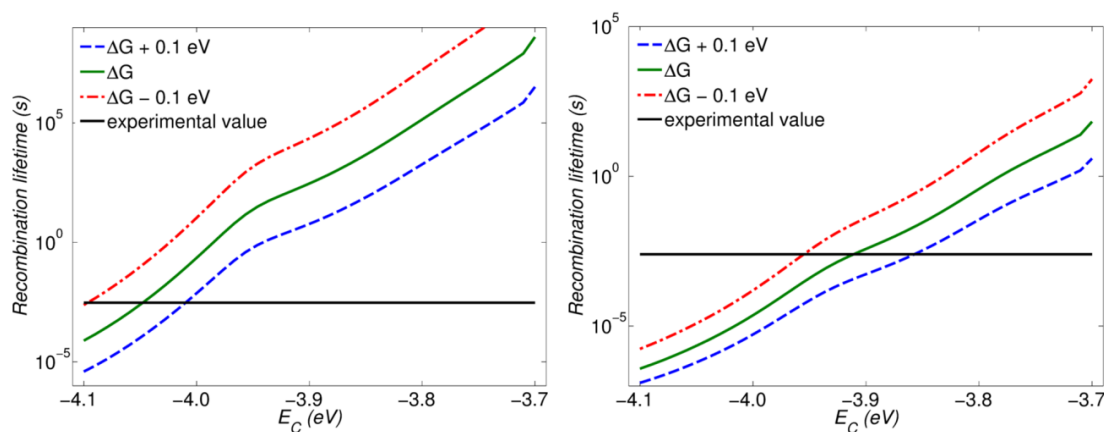


Figure 13. Uncertainty on ΔG and its impact on the recombination lifetime for the chromophores NKX-2311 (left) and OH1 (right).

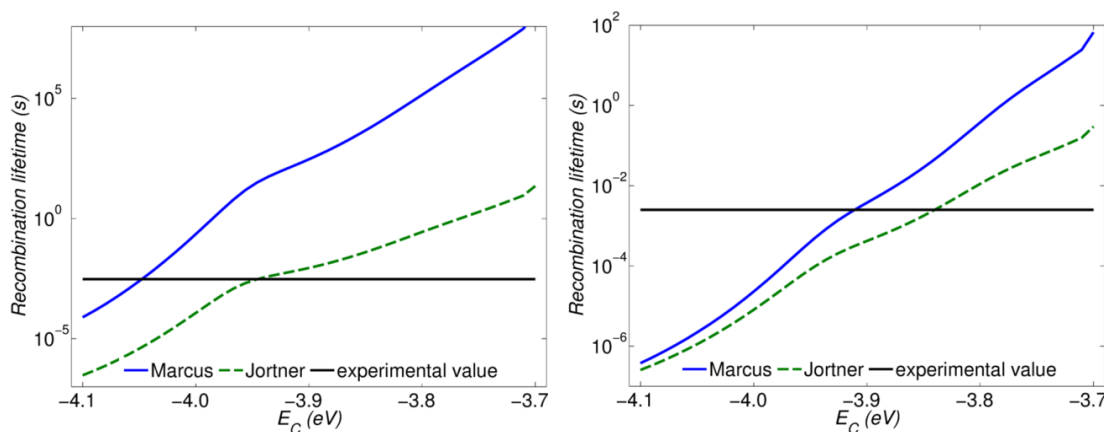


Figure 14. Recombination lifetime as a function of the conduction band minimum position: prediction using Marcus's expression and Jortner's expression. Left panel refers to NKX2311, right panel to OH1.

On the other hand, if we include an effective quantum vibrational mode by using equation (3.3), i.e. if we apply the Jortner equation, this produces a larger change in the recombination lifetimes, especially for the NKX dye (Figure 14), as can be expected for reactions in the Marcus inverted region [142], especially for the higher range of CBm energies. Nevertheless, both for the NKX2311 and the OH1 dye, both Marcus and Jortner equations predict the recombination times consistent with the

experimental recombination times within the realistic window for the conduction band edge.

In a very recent phenomenological study [143] charge recombination to two metal-organic redox shuttles was modeled using a scheme in a similar spirit to this one, based on Marcus theory of electron transfer. In Ref. [143], recombination from surface states was considered in addition to the states in the conduction band (the latter only at the energy of the conduction band minimum); an experimental value for ΔG , defined as $\Delta G = E_C - qE_{redox}$, was used, and an analytical expression for the reorganization energy, instead of the quantum-chemical values used here; recombination times were calculated and measured for a broad range (1 eV) of applied bias. Similar to our results, the experimental and modelled lifetimes showed pronounced energy dependence; the presence of surface states was necessary to describe experimental results for a ruthenium complex but not for a cobalt complex. We employed the experimental parameters provided therein to estimate the trap distribution, in order to test our assumption on the relative trap abundance in the system considered. For the range of CBm values considered here we obtain absolute densities of occupied traps from $4.6 \times 10^{-5} \text{ nm}^{-3}$ up to a maximum of $1.1 \times 10^{-2} \text{ nm}^{-3}$, thus confirming our initial argument on the small likelihood for CRD to be mediated by a trap state near the chromophore.

3.4 Conclusions

In this chapter we have compared the proposed expression for the charge recombination rate against the experimental data available for two families of chromophores. The model developed employing non-adiabatic theory for electron

transfer in inhomogeneous media contains three terms that control the electron recombination rate: (i) semiconductor-dye coupling, which determines the rate of electron transfer in the absence of nuclear motion, (ii) concentration of electrons in the TiO₂ conduction band, described by the Fermi-Dirac distribution, and (iii) the Franck-Condon term, dependent on the nuclear motion of the dye and of the surrounding solvent. We identify a limited number of parameters which determine completely the system's behaviour for the electron recombination process. Some of the parameters involved (reorganisation energy, free energy variation and electronic coupling between acceptor and donor species) can be determined with the aid of *ab initio* calculations, while others (conduction band minimum and *quasi*-Fermi level) cannot be computed for the realistic semiconductor-electrolyte interface, and experimental range of values need to be used. These parameters and the resulting recombination rates are related to one another in a non-trivial way. In particular, the position of the Fermi level under non-equilibrium conditions is affected by the number of photoinjected electrons, which, in turn, depends on the recombination rate (and on the electronic coupling) to the dye cation and/or to electrolyte species. Hence, the overall DSSC kinetics affects the rate of the particular recombination process.

As examples, we have considered two groups of chromophores: molecules containing a coumarin moiety connected to a cyanoacrylic group via alkene or (poly)thiophene spacer (the NKX family [138]) and benzofuro-oxazolo-carbazol dyes with various positions of anchoring groups (the OH family proposed in Ref. [137]). We have demonstrated that for the first group of chromophores, which meet the requirements of simple adsorption chemistry and the chemical structure varying

in a systematic way, and for which the partitioning scheme outlined in section 3.2.3 is reasonably accurate, the proposed method can reproduce the experimental ordering and give the correct order of magnitude for the recombination lifetime (within the experimental uncertainties on the parameters involved). The ordering is more reliable than absolute values of recombination lifetime, because of the uncertainty in both calculated and adopted experimental parameters. On the other hand, in the case of OH-type molecules, whose structure is more complex, with the flexible alkyl chains giving rise to many possible conformations, and with a more ambiguous adsorption chemistry, it is more problematic for the proposed computational scheme to convey an accurate picture of the processes taking place without a more detailed investigation of the dye monolayer adsorption configurations. Thus, the proposed scheme enables us to make qualitative predictions of relative recombination efficiencies, at least for families of dyes with systematic variation in the structure and with simple adsorption chemistry, although experimental input is needed if we want to make quantitative predictions of recombination rates. A possible area of application of this methodology is the prediction of the relative charge recombination rates between dyes with a rigid structure, which differ by small chemical modifications. The adsorption mode in these cases can be assumed to be constant and the theoretical methodology can predict the impact of the chemical change on the rate and whether this rate change is due to different electronic coupling or different Franck-Condon terms.

Chapter 4: Charge recombination at the TiO_2 -Electrolyte interface

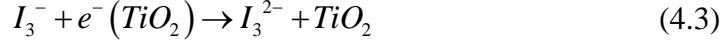
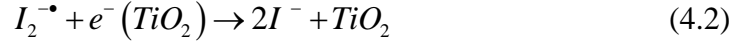
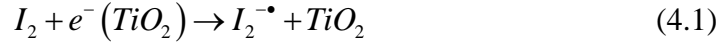
4.1 Introduction

In this chapter we will consider the other charge recombination process which operates in dye sensitised solar cells (DSSCs), namely the charge recombination to electrolyte. If the study of the CRD in the previous chapter has proved difficult for some molecules because of the complexity of their adsorption geometry, this is even more the case for electrolyte species, since they are not designed to adsorb onto the semiconductor substrate (and obviously do not feature an anchoring group).

The redox shuttle studied here is the I^-/I_3^- couple originally proposed by Grätzel and O'Regan [3]. The chemistry shown by this redox mediator is rather complex and, in contrast with the study of CRD, different species can be reduced at the interface with the TiO_2 nanoparticle depending on the experimental conditions. For these species a detailed characterisation of their adsorption geometry has been carried out in section 4.3, as no previous theoretical investigation addresses this aspect. Furthermore, in section 4.3.2 we will be able to narrow down considerably the range of permissible values for the conduction band minimum introduced in chapter 3, thanks to the wealth of experimental data available, which is reviewed in section 4.1.1.

4.1.1 *Review of experimental and theoretical studies*

Different electrolytes present in solution can capture an electron from the semiconductor (TiO_2) conduction band according to the following reactions [144]:



Reactions (4.1) and (4.3) involve acceptors which are always present in a DSSC and whose concentration ratio depends on the thermodynamic of these species in solution, whereas the acceptor species in reaction (4.2), $I_2^{\bullet-}$, is generated after the oxidised dye has been reduced by iodide [144]; as such this acceptor is not going to be available for CRE in dark conditions.

The experimental information on the rates of these processes can be summarized as follows:

- (i) The ratio between different charge recombination rates involving I_3^- and I_2 has been evaluated using transient absorption spectroscopy (TAS) [44]. The experimental set up did not feature any adsorbed dye on TiO₂ nanoparticles in order to specifically determine CRE lifetimes under illumination and it was found that recombination to I_2 is two orders of magnitude faster than charge recombination to I_3^- .
- (ii) Dynamic voltage decay measurements in the dark [42, 145] (where the overall charge density in the photoelectrode, previously generated by applying a potential bias, V_{app} , is measured after relaxation) provide the range 10^{-2} - 10^0 s for CRE lifetime. This technique cannot identify the

molecular acceptor responsible [7], although I_3^- is the only species present in sizeable quantities in a DSSC under no illumination [146].

- (iii) The rate of reaction (4.2) has been probed with TAS measurements in different regimes: in working conditions this species is long-lived (~ 0.5 s) [45], whereas, if a higher electron concentration is present in the photoelectrode, then charge recombination to I_2^- takes place with a lifetime in the region of 10^{-7} s [46].

Theoretical modelling of processes (4.1)-(4.3) at an atomic level may clarify the different observations providing additional microscopic insight on the CRE and it is somewhat surprising that the TiO_2 /electrolyte system has been studied theoretically only in a limited number of works. Da Silva and co-workers [81] have modelled with the aid of molecular mechanics techniques a realistic semiconductor/electrolyte solution interface: the main information extracted concerns the solvent structure near the surface defects. The density of states (DoS) for the whole system (electrolyte/solvent/ TiO_2) has been determined and compared with the position of the molecular orbitals for electrolytes in the solution bulk; this energy alignment analysis allows them to conclude whether a CRE can take place or not, but clearly doesn't establish the lifetime for the electron transfer, which is the object of this chapter. Asaduzzaman and Schreckenbach have studied the system electrolyte/ TiO_2 at the DFT level of theory with and without periodic boundary conditions [147, 148]. The analysis concentrates mainly on the energetic of the adsorption onto the semiconductor surface and on the relative alignment of the adsorbate molecular orbitals but no rate was computed. Radically different is the approach by Prezhdo

and co-workers [76], who have evaluated the electron dynamics during the electron transfer process thanks to an hybrid quantum/classical simulation scheme. Unfortunately, because of the high computational cost, their analysis is constrained to only one electrolyte species and to timescales of the order of picoseconds, while the experimental estimate for the reaction studied is many orders of magnitude slower.

4.2 Methodology

In this section we present the computational scheme employed. The electron transfer theory presented in chapter 2 is adapted to the study of small inorganic adsorbates, lacking an anchoring group, to circumvent this problem a Green's function formalism has been employed in section 4.2.2 to derive the spectral density. The reorganisation energy's external component has been evaluated within a dielectric continuum picture, while the contribution of the internal (quantum) degrees of freedom has been evaluated explicitly as done in chapter 3. Energy alignment of the relevant levels and free energy variation of the electrolyte upon charge transfer are estimated from the existing experimental literature. These quantities will then be employed in the evaluation of the charge recombination rate previously given in equation (2.8).

4.2.1 Reorganisation energy, λ

For the evaluation of the reorganisation energy we maintain the partition into internal and external contribution, according to Marcus's theory. The external reorganisation energy is defined as a function of the transverse component of the nuclear polarisation and is related to the motion of solvent molecules, while the

internal component is due to molecular vibrations. Given the small size of the adsorbates the cavity introduced for the evaluation of the external component can be approximated by a sphere of radius r_A and the resulting reorganisation energy can be computed following Marcus [149]:

$$\lambda_{ext} = \frac{q^2}{4\pi\epsilon_0} \left[\frac{1}{2r_A} \left(\frac{1}{\epsilon_\infty^{(1)}} - \frac{1}{\epsilon_0^{(1)}} \right) - \frac{1}{2d_A} \left(\frac{1}{\epsilon_\infty^{(1)}} \frac{\epsilon_\infty^{(2)} - \epsilon_\infty^{(1)}}{\epsilon_\infty^{(2)} + \epsilon_\infty^{(1)}} - \frac{1}{\epsilon_0^{(1)}} \frac{\epsilon_0^{(2)} - \epsilon_0^{(1)}}{\epsilon_0^{(2)} + \epsilon_0^{(1)}} \right) \right] \quad (4.4)$$

Symbols in the expression above have an immediate physical meaning: q is the charge being transferred in the reaction, ϵ_0 is the vacuum permittivity, r_A is the ion radius and d_A indicates its distance from the semiconductor surface. Static dielectric constants for each dielectric have been labelled $\epsilon_0^{(n)}$, with $n = 1$ for the solvent (acetonitrile) and $n = 2$ for the semiconductor (TiO_2 , anatase); $\epsilon_\infty^{(n)}$ refers to the dielectric constants at infinite frequency of radiation. In the expression above the experimental values for the dielectric constants for the two media are required ($\epsilon_0^{(1)} = 36.64$ [150], $\epsilon_\infty^{(1)} = 1.806$ [151], $\epsilon_0^{(2)} = 48.0$ [152], and $\epsilon_\infty^{(2)} = 6.45$ [143]) as well as the radius for the acceptor species. The radius is estimated from the total volume of the actual electron acceptor which is in turn evaluated from electronic structure calculation and defined as the volume with electron density larger than 0.001 e/bohr^3 . We note that the original Marcus formulation [149] involves the presence of 2 species (acceptor and donor) equidistant from the interface between the two dielectric media. When heterogeneous electron transfer is studied instead, with one of the ‘species’ being completely delocalised over the second dielectric, the appropriate distance to consider is the distance from the semiconductor surface d_A

and not twice this value as in the original theory. d_A , consistently with other phenomenological studies of electron transfer [143], has been set equal to the radii of the molecular adsorbate.

If the acceptor species undergoes barrierless dissociation upon electron capture as in reaction (4.2), then the total reorganisation energy is given by $\lambda = \lambda_d + 0.5 \times \lambda_{ext}$ where λ_d is the dissociation energy [153] and a prefactor multiplies the external component since we are interested in the solvent reorganisation energy only. For the other species we compute the internal reorganisation energy as specified in section 3.2.3.4.

4.2.2 Spectral density

The calculation of the spectral density follows a different (but formally equivalent) route to that reported in section 2.4: instead of estimating the eigenenergies of the semiconductor ε_i and then approximate numerically the Dirac's delta function appearing in equation (2.29) we can resort to the Green's function formalism. The Hamiltonian matrix of the overall system can be factorised into submatrices each describing respectively the TiO₂ slab (H_L), the molecular adsorbate (H_d) and the interaction between the two (γ). Following Thygesen [103] we define the retarded Green's function (G^r) for the reservoir L as the inverse of the matrix $(S_L^{-1}\varepsilon^+ - S_L^{-1}H_LS_L^{-1})$, where ε^+ is a complex variable: $\varepsilon^+ = \varepsilon + i\eta$, with ε real, i being the imaginary unit and η a real infinitesimal; with S we indicate the overlap matrix. The same definition holds for the advanced Green's function (G^a) by replacing $\varepsilon^+ \rightarrow \varepsilon^- = \varepsilon - i\eta$. The spectral density for the reservoir (A) is given by the

Green's function discontinuity across the real axis, we compute this quantity as [154]: $A(\varepsilon) = i(G^r - G^a)$; the density of states (DoS) is readily obtained from the spectral density by taking its trace and dividing it by 2π . The broadening matrix is then defined as the product between the spectral density, the coupling sub-matrix γ and its hermitian conjugate γ^\dagger :

$$\Gamma_{m,n} = \gamma A \gamma^\dagger \quad (4.5)$$

Finally, the spectral density is obtained [116]:

$$\tilde{\Gamma}(\varepsilon) = \frac{1}{\hbar} \sum_{m,n} |m\rangle \Gamma_{m,n} \langle n| \quad (4.6)$$

where $|m\rangle$ and $|n\rangle$ indicate the LUMO coefficients in the atomic orbitals basis set for the isolated molecule considered.

4.2.3 Driving force ΔE and Franck-Condon term

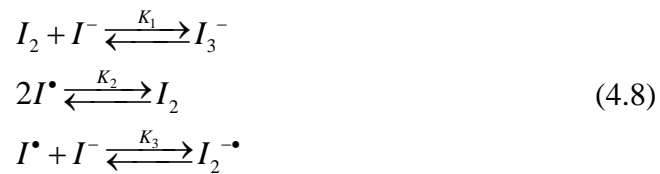
The energy difference ΔE between the initial (oxidised) and final (reduced) state for the molecular adsorbate is a key parameter for the evaluation of the Franck-Condon term in equation (2.11). Although it is possible to estimate this quantity with the aid of *ab initio* calculations within an implicit solvent scheme [155], we employ instead the extensive experimental data available to reduce the sources of inaccuracies on the final result. Following Hagfeldt and Boschloo [144] we can obtain the electrochemical potential for the reactions (4.1)-(4.3) relative to the position of the electrolyte Fermi level $E_{f,redox}$, then, using our estimate in Ref. [155] for the latter, we can quantify ΔE . We exploit the relative position of the

electrochemical potentials given in Ref. [144] (thanks to the Q factor reported below) rather than the standard reduction potentials given therein because in a working device unitary concentrations are generally not attained. Instead we derive $E_{f,redox}$ from the Nernst equation for the overall reaction $I_3^- + 2e^- = 3I^-$. The standard potential for this reaction in acetonitrile has been estimated as +0.354 V [144], whereas the equilibrium concentration for I_3^- (typically not provided in experimental reports, see for instance Ref. [42]) has been estimated thanks to its equilibrium formation constant in acetonitrile [156].

The driving force for reactants in equations (4.2) and (4.3) can be obtained from $E_{f,redox}$ by respectively subtracting and adding the quantity Q :

$$Q = \frac{RTe}{F} \ln \left(\frac{K_1^{\frac{1}{2}} K_2^{\frac{1}{2}}}{K_3} \right) \quad (4.7)$$

where the formation constants in equation (4.7) refer to the reactions below:



Experimental values for the formation constants are available for reactions involving charged species in equation (4.8). We have $\log(K_1) = 6.76$ and $\log(K_3) = 3.4$ [146, 157]. For the iodine formation reaction (middle equation in (4.8)) we estimate the free energy variation in acetonitrile and then obtained

$$\log(K_2) = \frac{\Delta G^0}{RT \ln 10} = 14.88 \text{ for } T = 298.15\text{K. Results are summarised in Table 2.}$$

The set of experimental values used above refers to reactions taking place in the solvent bulk, while the system under investigation here clearly features an interface where the redox reaction is occurring; this asymmetry in the medium surrounding the reactants is bound to impact on the ΔE evaluated above, via a change in standard reduction potential of the reactants. The only experimental study we are aware of that touches on the electrochemistry in nanostructured media is Ref. [158], which relates the experimental outcome to either a variation of the reactants' standard potential or to a change of their activity coefficients at the interface. We note that these two hypothesis, albeit being equally able to explain the experimental data, are not equivalent in our model, with the first producing a change in the reactant's ΔE (hence modifying the Franck-Condon term) the second impacting on the electrolytes' activity coefficients, hence changing the Fermi level position for the redox couple. Therefore, we believe it would be unwise to speculate on the possible interfacial effects on the electrolytes' redox potential in absence of clear experimental data to compare against.

The quantities introduced thus far are required for the evaluation of the charge recombination reaction rate as it was given in equation (2.8) in chapter 2.

4.2.4 Computational details

Density Functional Theory electronic structure calculations were performed as reported in chapter 3 (section 3.2.3.2), but different slab sizes were used: (2×3) and (2×4) surface unit cells were employed respectively for diatomic or triatomic adsorbates in order to avoid interaction between adjacent molecules under periodic boundary conditions. Double- ζ polarised basis was employed for I atoms, in

conjunction with Troullier-Martins norm-conserving pseudopotential; the spin-orbit coupling has been neglected.

In order to describe the interaction with charged electrolytes a net charge was imposed on the system slab/adsorbate system when I₂⁻ and I₃⁻ were analysed [148]. This charge is compensated by a non-uniform background charge distribution generated by the simulated doping option available in the Siesta code. In order to test the computational procedure for systems featuring negatively charged adsorbates, we have considered, following Schreckenbach and Asaduzzaman [147], an overall neutral replica of the I₂⁻/TiO₂ system including a caesium counter ion; the resulting adsorption geometries and Mulliken populations are in very good agreement with the same results in charged cells.

Geometry optimisation calculations for the anatase-adsorbate interface have been performed with an energy cut-off of 150 Rydberg and sampling the Brillouin zone at 9 **k**-points (corresponding to a **k**-grid cut-off parameter in SIESTA of 15 Å), while keeping atoms in the bottom layer fixed to their corresponding bulk positions. Basis set superposition error (BSSE)[159] was taken into account for each adsorption mode considered.

Ab initio calculations of molecular species in the presence of the solvent (acetonitrile), such as dissociation energy for I₂⁻ or the iodine formation reaction in equation (4.8), have been carried out within the polarisable continuum model [121] framework, as implemented in Gaussian03 [124] at the B3LYP/LanLDZ level of theory.

4.2.5 Energy alignment between molecular adsorbate and TiO_2 band structure

The kinetics of CRE depends critically on the position of few energy levels, which are substantially affected by the experimental set-up of the system; these are the conduction band edge (E_C) for the semiconductor and the *quasi*-Fermi level ($E_{f,n}$). For devices under illumination we have shown in the previous chapter that the experimental variability due to solvent viscosity, electrolyte counterions and additives can be reduced to the uncertainty on the position of the conduction band edge in the range between -4.24 and -3.84 eV vs. the vacuum level for typical equilibrium electrolyte concentrations ($[\text{I}_3^-] = 0.05 \text{ mol dm}^{-3}$, $[\text{I}^-] = 0.75 \text{ mol dm}^{-3}$). The position of the electrolyte Fermi level ($E_{f,redox}$) has been taken as -4.9 eV following the experiment in Ref. [155]. The computed rates under illumination are therefore presented as a function of E_C which is varied in the plausible range between -4.24 and -3.84 eV.

The situation is different under dark when the position of $E_{f,n}$ is determined by the external potential V_{app} (which can be time dependent). In Ref. [31] it was shown that for a large range of values for $E_{f,n}$ the simple relation $E_{f,n} = E_{f,redox} + V_{app}$ holds in the steady state. In this case $E_{f,redox}$ and V_{app} are controlled experimentally. The computed rates under dark are presented as a function of the applied bias V_{app} (for simplicity E_C is fixed to -4.24 eV in these cases).

Experimental factors which cannot be included in a quantum-chemical model of the interface affect the absolute position of E_C . The computed value of E_C is also affected by the known DFT inaccuracies in the determination of virtual orbitals' energies. To conjugate molecular-level insight deriving from DFT calculations and

modelling of a realistic device we therefore align the computed DoS for the slab-adsorbate system to the conduction band edge value obtained for the particular electrolyte concentrations reported above.

It is convenient to summarize at this point the procedure used to compute the charge recombination rate. Electronic structure calculations are used to compute the adsorption geometry, the electrolyte-electrode coupling ($\tilde{\Gamma}(E)$ in equation (4.6)) and the internal reorganization energy. A continuum model is used to compute the external reorganization energy. Experimental data are used for the ΔE of the redox reactions and to adjust the conduction band edge (a range is used for recombination under illumination).

4.3 Results

The molecular energy parameters necessary to evaluate the Franck-Condon term defined in equation (2.11) for the three reactions (4.1)-(4.3) under investigation are reported in Table 2. Following Ref. [153], the internal reorganisation energy for I_2^- , which dissociates after accepting an electron, has been set equal to its dissociation energy and for this reason is slightly lower than the other values.

Table 2. Molecular parameters for the electrolytes considered. The internal reorganisation energy for I_2^- is set equal to its dissociation energy. The total reorganisation energy has been calculated as $\lambda = \lambda_{int} + 0.5 \times \lambda_{ext}$.

Adsorbate	r_A (Å)	λ_{ext} (eV)	λ_{int} (eV)	λ (eV)	ΔE (eV)
I_2	2.75	0.60	1.20	1.50	-4.54
I_2^-	2.99	0.55	0.89	1.17	-5.20
I_3^-	3.46	0.48	1.49	1.73	-4.34

The most stable adsorption modes for the molecular systems have been selected by comparing their adsorption energies $E_{ads} = E(\text{TiO}_2 + \text{electrolyte}) - E(\text{TiO}_2) - E(\text{electrolyte})$ after counterpoise correction for the basis set superposition error [159]; three different initial configurations were optimised with SIESTA for each electrolyte species: in two of them the adsorbate was perpendicular to the slab with the iodine atom closest to the surface being near to either the bridging oxygen or the titanium atom; in the third configuration the adsorbate was flat on the slab surface. The optimised structures not selected were at least 0.3 eV less stable than the selected configurations or had positive adsorption energy. We note that the particular value of adsorption energy is not used in the evaluation of the rate, but it is rather employed as a criterion to select the most likely adsorption geometry and hence the relative spectral density. The spatial dependence for this parameter has been explored for the (adiabatic) electron transfer at the metal-molecule interface for a Hückel-Hubbard model solved at the mean-field level of theory [160]. Albeit this approach is very relevant also for the type of systems studied here, it would be difficult to integrate with an atomistic simulation of the interface at the DFT level of theory. We therefore select the most stable attachment configuration for the electrolytes considered. This choice is reminiscent of the experimental evidence collected for the O_2 photochemical reduction at TiO_2 interfaces: TAS studies highlight the presence of specific binding sites on the nanostructured TiO_2 surface [161]. It is reasonable to assume that the CRE reactions reported here proceed through a similar mechanism, as it can be inferred from experimental studies on DSSCs [162] where the use of additives was shown to impact on the CRE reaction by preventing the electrolytes to

get close to the semiconductor interface. Furthermore, E_{ads} is certainly going to be modulated by the presence of solvent in the real device; however we assume that this effect will not alter the relative energetics between different adsorption modes of the same species. The resulting adsorption geometries are shown in Figure 15: I_2 and I_2^- show a similar equilibrium distance from the closest oxygen atom (2.7 Å), while for I_3^- the shortest distance Ti-I is 3.0 Å; the corresponding values for adsorption energy are reported. To the best of our knowledge, the computational studies published in the literature only allow for a comparison with I_3^- : this species has been modelled on different sized anatase clusters and on periodic rutile (110) slabs (where no adsorption energies were provided). Our adsorption energy for I_3^- compares favourably with the value given [148] on 84 atom anatase cluster; although a rather large spread in adsorption energy was presented depending on the cluster size. The adsorption geometry obtained in both these studies is similar to the lowest energy structure we obtained, with the adsorbate molecule lying flat on the surface, Figure 15 (bottom). Our Ti-I distances (≥ 3.0 Å) are also in agreement with the literature values on anatase clusters (2.7-3.0 Å) [148] and rutile (110) surface 2.6 Å [147].

Mulliken electron population analysis has been carried out on the structures obtained: the electron population on iodine atoms for I_2 remains unchanged in comparison with the isolated molecule, partial delocalisation occurs when I_3^- is interacting with the surface, with a fraction ($\sim 0.6 e^-$) of the original negative charge retained by the adsorbate; complete delocalisation over the slab occurs when the I_2^- radical is considered. This behaviour is largely expected and follows the electron affinity trend for the molecular species involved [163, 164].

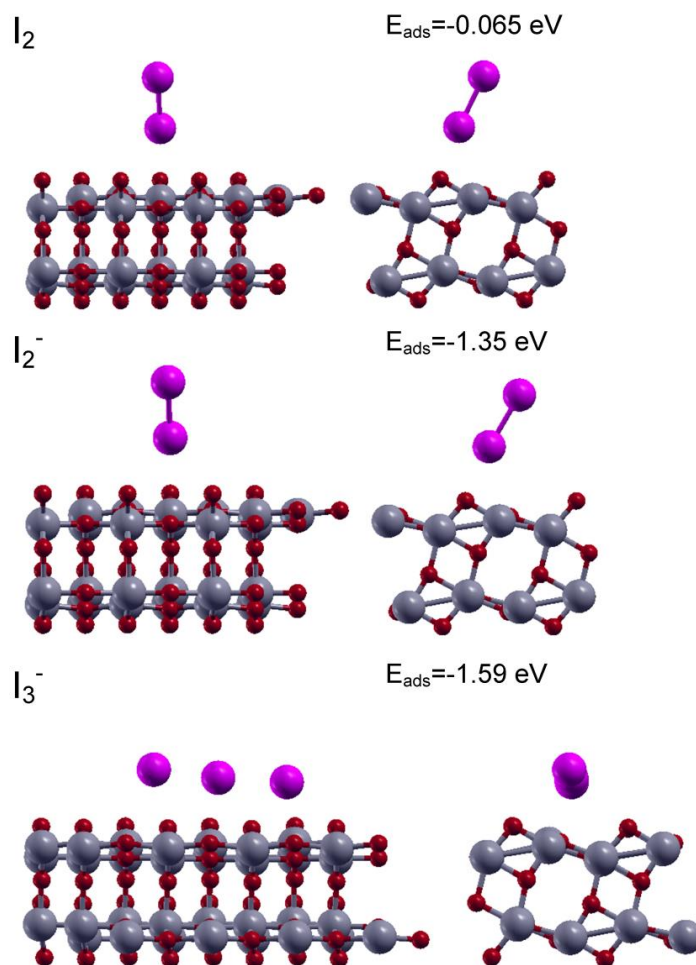


Figure 15. Adsorption configurations (along the [10-1] direction on the left, on the right along the [010] direction) for the anatase (101)-electrolyte system; iodine atoms are shown in purple, titanium atoms in grey and oxygen atoms in red.

The spectral densities and the Franck-Condon terms are shown in Figure 16 on the left and right panel respectively. From the Franck-Condon term position we can conclude that the energy level shift for the adsorbates' attachment level would impact only on the recombination to I_2^- . For the other electrolytes a wide-band approximation (typically employed for metallic substrates) could be applied, since the adsorbate's level overlaps with the *quasi*-continuum of band states and is located far from the band edge [89]; this would lead to a vanishing energy level shift and to

the spectral density assuming a constant value. In order to treat all the electrolytes considered on the same footing, in what follows we will disregard the contribution of these self-energy effects on the energy levels alignment. Particularly relevant for the alignment of the Franck-Condon term is the internal component of the reorganisation energy; the totally symmetric vibrational modes (for I_3^- and I_2) are those contributing more substantially because of the bigger relative atomic displacement, and hence bigger Huang-Rhys factor.

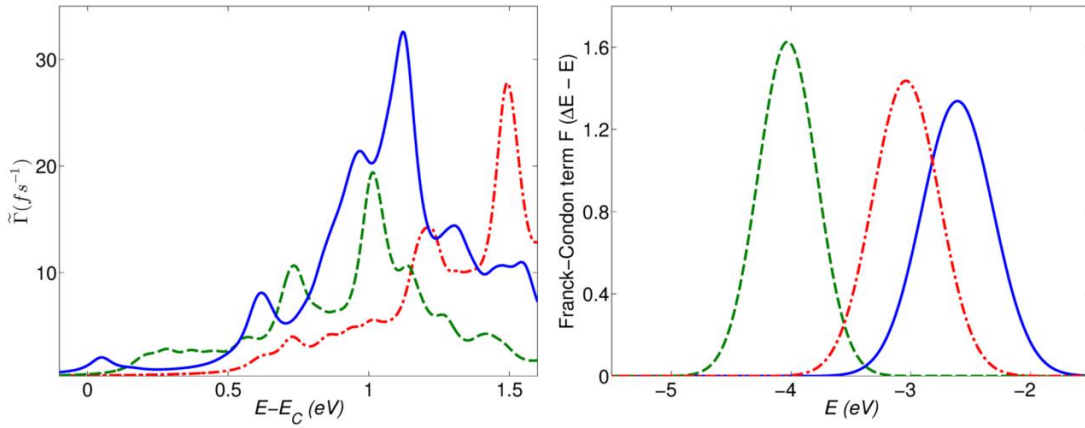


Figure 16. Spectral densities (left panel) and Franck-Condon terms (right panel) for the electrolytes considered: I_3^- (blue solid line), I_2 (red broken line) and I_2^- (green dashed line).

4.3.1 Charge recombination in the dark

We start by considering the charge recombination lifetime, $\tau_{CRE} = 1/k_{CRE}$, for I_3^- and I_2 in the dark (I_2^- is not present in these conditions). Figure 17a shows the CRE rate for I_3^- (blue lines) and I_2 (red lines) as a function of applied bias for two representative values of E_C . The ratio between recombination rates ranges from 10 to 30 depending on the applied potential, while a value of ~ 100 was reported by Green [44]; in this experiment the charge recombination process from dye-free TiO₂ was

studied first in the presence of molecular iodine only and then with an excess of iodide to generate quantitatively I_3^- .

The values of E_C considered in panel a) are -4.24 eV (empty symbols) and -4.13 eV (full symbols); in the first case we obtain values of recombination times consistent with the experimental estimate from dynamic voltage decay measurements which provide the range 10^{-2} s - 20 s, as given in Refs. [165] and [40] respectively. For the second E_C value we observe recombination kinetics for I_3^- which is too slow in the low V_{app} range by a factor ≈ 25 , not a very large variation in the context of interface electron transfer reaction (for example an increase in reorganization energy by 0.2 eV can produce a similar variation in τ_{CRE} to that observed by moving upwards the conduction band edge position as done in panel (a)).

In the bottom panel we explore the impact of the electrolyte concentration (which affects the position of $E_{f,redox}$): the electrolyte concentrations considered are then increased up to $[I_3^-] = 50 \text{ mol dm}^{-3}$ and $[I^-] = 450 \text{ mol dm}^{-3}$ (and shown with empty symbols in Figure 17b) resulting in faster recombination, while with the more dilute concentration than in panel (a) ($[I_3^-] = 0.05 \text{ mol dm}^{-3}$ and $[I^-] = 0.3 \text{ mol dm}^{-3}$) we obtain the slower kinetics ('+' symbol for I_3^- and 'x' symbols for I_2). As expected, increasing the acceptors' concentration makes the overall kinetics faster, although to a different extent for the different electrolytes; while the CRE process is faster for I_2 by a factor 1.5 across the whole range of applied potentials, I_3^- shows also a change in the slope of the curve giving faster recombination at higher values of V_{app} .

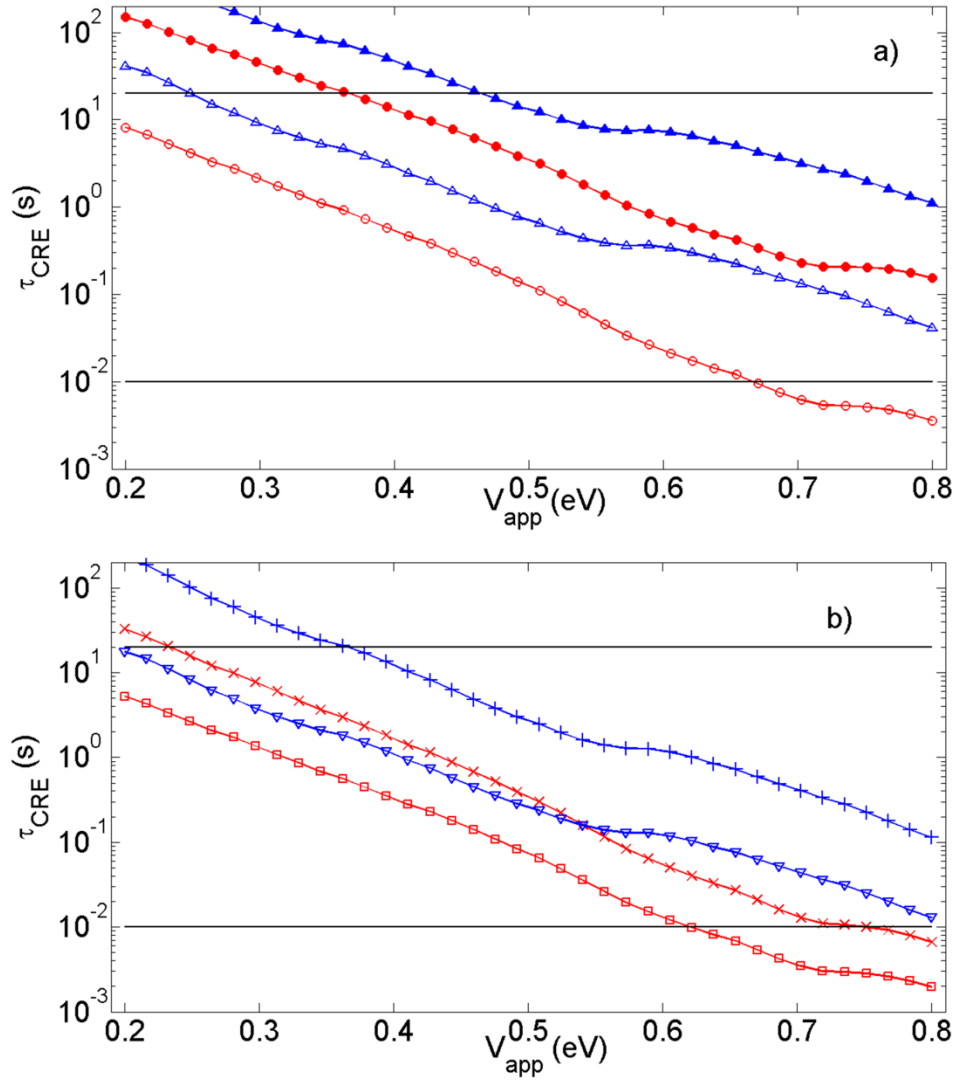


Figure 17. Recombination lifetimes as a function of the applied bias potential for I₂ (red lines) and I₃[−] (blue lines). The experimental range is between the horizontal lines. Panel a) shows the dependence on the parameter E_C ($= -4.24$ eV, empty symbols, $= -4.13$ eV, full symbols) with electrolyte concentration $[I_3^-] = 0.05$ mol dm^{−3} and $[I^-] = 0.75$ mol dm^{−3}. Panel b) reports the dependence on the electrolyte concentration keeping $E_C = -4.24$ eV; + symbols and × symbols indicate CRE to I₃[−] and I₂ respectively with concentrations $[I_3^-] = 0.05$ mol dm^{−3} and $[I^-] = 0.3$ mol dm^{−3}. Empty symbols are obtained for $[I_3^-] = 50$ mol dm^{−3} and $[I^-] = 450$ mol dm^{−3}.

The value of -4.24 eV chosen for the conduction band edge is only coincidentally equal to the value for a TiO₂/water interface [166]. In our case this value is the

bottom of the range provided experimentally by Bisquert *et al.* [136] for a selection of experimental set-ups in organic solution.

4.3.2 Charge recombination under illumination

A rather accurate characterisation of the absolute rate of charge recombination process to I_2^- is available, and this can be used to evaluate the best value of the only unknown parameter E_C before computing the charge recombination rate for the other electrolytes. Under illumination the *quasi*-Fermi level is no longer experimentally controllable but it is fixed by the balance between photoinjected electrons and electrons leaving the semiconductor. A characteristic feature of the electron transfer reactions involving I_2^- is the dependence on the number of photoinjected electrons in the conduction band: at low electron densities the charge recombination is so slow that other reactive pathways become available (namely the dismutation reaction $2 I_2^- \rightarrow I_3^- + I^-$, $\tau_{dis} \sim 1 \mu s$) while at high electron concentration reaction (4.2) takes place with a measured lifetime $\tau \sim 100$ ns. The threshold between the two regimes has been experimentally determined to be 1 injected electron per TiO_2 nanoparticle [46], i.e. $1.1 \cdot 10^{18} e^-/cm^3$ or $E_{f,n} = -4.41$ eV assuming a nanoparticle diameter of 12 nm (*quasi*-Fermi level and electron density are related by the Fermi-Dirac distribution). As a test for the model considered, we then evaluate the recombination lifetime for reaction (4.2) under this limiting electron concentration $E_{f,n} = -4.41$ eV, at a lower concentration $E_{f,n} = -4.50$ eV (where the dismutation should be faster) and at higher electron concentration $E_{f,n} = -4.32$ eV where CRE should be faster.

The recombination lifetimes for the selected values of quasi-Fermi are shown in Figure 18 as a function of E_C . From the computed values we can establish a range of values for E_C compatible with the experimental knowledge of this system, i.e. if we consider the low electron density regime, then only values more positive than -4.07 eV are consistent with CRE process being slower than the dismutation reaction, while in the high electron density case $E_C \approx -3.95$ eV gives a CRE time constant of the correct magnitude. In summary the experiment are reproduced if E_C takes values in the narrow range between -4.07 eV and ≈ -3.95 eV.

The conduction band edge position has been considered as an adjustable parameter in this analysis while the best value E_C has been identified to match different experimental settings. It is reassuring that the “best” E_C are within a very limited range of 0.12 eV in the middle of the permissible range; it is then possible to narrow down the plausible values of this unknown. On the other hand it is also possible to speculate that the difference between the “best” value of E_C obtained in this case and those considered in Figure 17 (i.e. in the dark) are meaningful, i.e. they are related to the variation of E_C with the experimental condition. Indeed, E_C values around -4 eV were necessary to reproduce the experimental data under illumination, whereas when we considered I_3^- an interval centred at -4.2 eV gave recombination lifetimes compatible with the experiment. This behaviour has been noted upon by O'Regan and Durrant [167] who reported a recombination flux twice as big under illumination than in the dark and suggested that a change in the surface charge is taking place as the operational conditions of the device are changed. This intriguing hypothesis surely represents an interesting challenge for both theory and experiment,

since no calculation or local measurements of the conduction band minimum at different illumination intensities have been carried out to date.

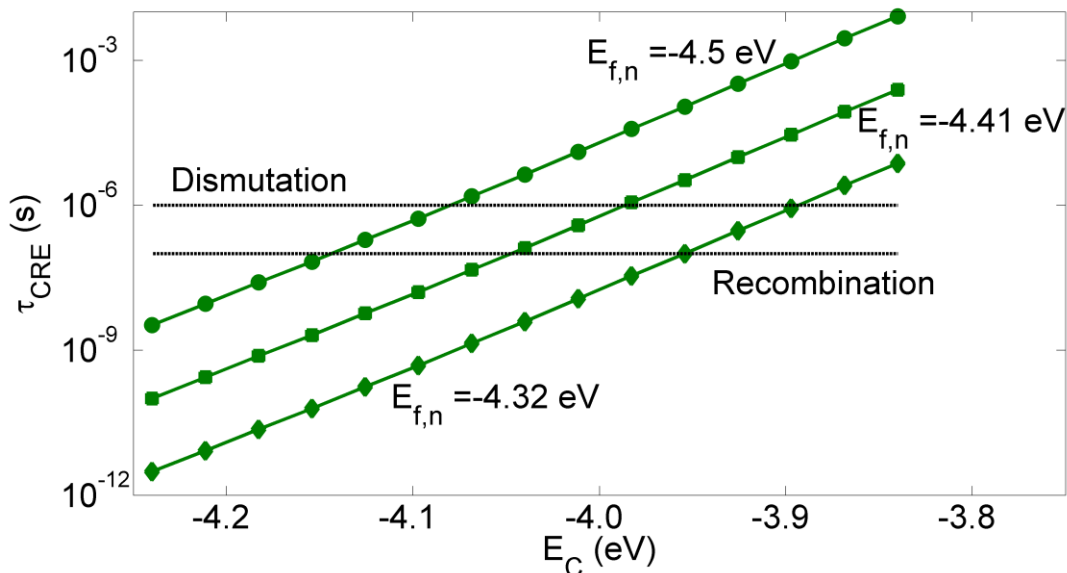


Figure 18. Recombination lifetime for I_2^- as a function of the conduction band edge for selected values of the *quasi*-Fermi level, horizontal lines indicate experimental values for recombination at high electron concentration and dismutation reactions, values employed for the *quasi*-Fermi levels $E_{f,n}$ are reported next to each line.

We can now analyse the charge recombination process under illumination for all the electrolyte species potentially present in a working DSSC. The CRE lifetimes for a range of E_C values are reported in Figure 19. τ_{CRE} for each species at $E_C = -4.01$ eV, i.e. the middle value of the interval obtained in the first half of this section, are 16 ms, 0.12 ms, 0.41 μ s respectively for I_3^- , I_2 , I_2^- . The rates obtained from equation (2.8) hold for a fixed acceptor concentration at the interface; in order to draw any conclusion on the processes taking place in an actual device we ought to consider the relative abundance of these electrolytes in solution. Although the detailed determination of the concentration profiles for each electrolyte near the

semiconductor surface would pose an intriguing problem *per se*, we must stress that it would require a completely different set of theoretical tools than those employed herein. Therefore, as an approximation, we will assume a uniform electrolyte distribution across the device.

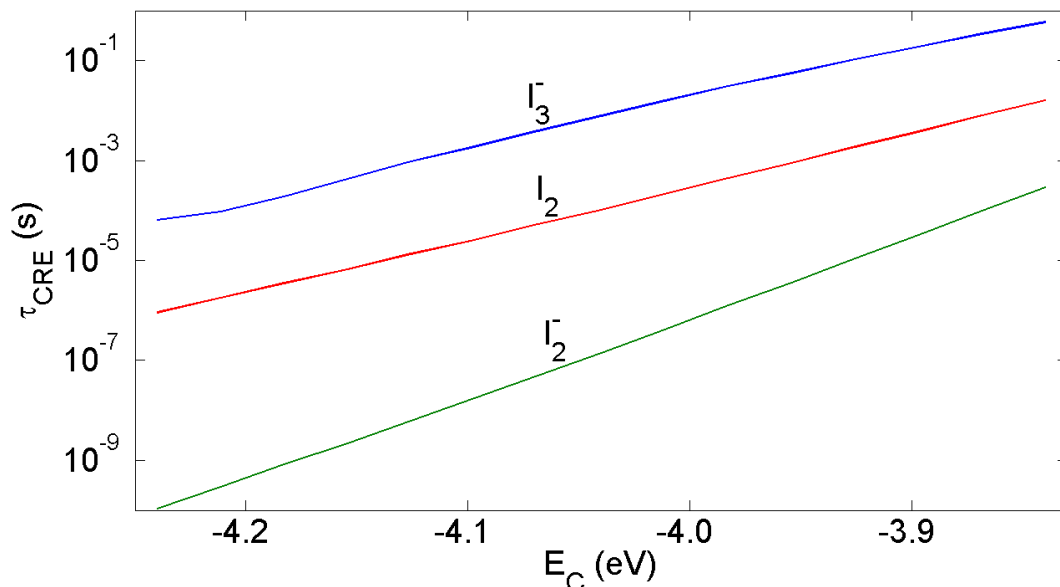


Figure 19. Recombination lifetimes as a function of the conduction band edge. Labels in figure refer to the species present at the interface. $E_{f,n}$ has been set equal to -4.41 eV for all electrolytes.

The prominent species present is I_3^- (with a concentration of about 10^{-2} mol dm⁻³), hence this species is the most likely to be the main acceptor for CRE processes; the free iodine concentration in a working device is particularly small ($\sim 10^{-8}$ mol dm⁻³) owing to the favourable triiodide formation constant in acetonitrile, thus suggesting that this species will not contribute to the CRE processes. The I_2^- steady state concentration, on the other hand, has been estimated as 3 μ M [144], as a subproduct of dye regeneration but also as due to photolysis of I_3^- [168]. In such a low

concentration limit it is reasonable to assume both processes (CRE and dismutation) involving I_2^- to be diffusion limited. As the characteristic diffusion limited lifetime is ~ 1 s (see Ref. [31]) we can see how the value for CRE obtained here is compatible with the TAS experiment by Montanari [45], where the lifetime for this species was quantified as 0.5 s.

4.4 Conclusions

In this chapter we have studied theoretically one of the main loss mechanisms in DSSCs, i.e. the charge recombination reaction to species present in the electrolyte solution surrounding the nanostructured anatase photoelectrode. This reaction has been modelled within the non-adiabatic theory for electron transfer in the condensed phase where the presence of the Franck-Condon term accounts for the solvent dynamics and the coupling between the semiconductor slab and the molecular adsorbate has been evaluated with the aid of Green's functions methods for non-orthogonal basis sets. Parameters entering the Franck-Condon term have been obtained from experimental sources (ΔE) and by applying an analytic expression for the external reorganisation energy for electron transfer at an idealised semiconductor-electrolyte interface. The other key parameter in this model, the conduction band edge, has been taken (as a range) from the experimental sources available following the same methodology used in the previous chapter and in Ref. [155].

The available experimental data are diverse and non-homogenous but the level of agreement between calculation and experiment is very good. The application of this model to CRE predicts lifetimes within the experimental range when the reaction

occurs in the dark for values of the *quasi*-Fermi level that match the experimentally variable range, in particular we find that (i) the ratio between CRE rates to iodine and triiodide rate is in agreement with the experiment and (ii) the CRE to triiodide rate is compatible with the measured electron depletion in the semiconductor electrode. Under illumination, we correctly reproduce the CRE absolute rate to I₂⁻ using value of the conduction band edge in a narrow range within the permissible values for this parameter. The validation of the methodology against a diverse set of experimental data provides confidence in the absolute values of the CRE rates computed for the three electrolytes in the condition appropriate for a working dye sensitized solar cell which we presented in the concluding part of this chapter.

Chapter 5: Impact of defects on the charge recombination reaction at the semiconductor-adsorbate interface

5.1 Introduction

In this chapter we focus on the role of defects in the semiconductor lattice and we study the impact of their energy level and position in the semiconductor slab on the charge recombination kinetics. Optimisation strategies that would impede the charge recombination are then devised by modifying the ‘molecular’ parameters that enter our model (i.e. the reorganisation energy and the energy difference between the neutral and oxidised adsorbate), while we keep the coupling strength between semiconductor and the adsorbate fixed to a constant value. Strategies for the modulation of the last parameter are reported in the following chapters 6 and 7.

An ideal device in operational conditions will produce a potential difference equal to V_{OC} , but the efficiency in a realistic system will be curbed by dissipative pathways for the photoinjected electrons, such as the recombination with oxidised species near the semiconductor surface or the trapping at defect states present in the semiconductor (sintered TiO_2 nanoparticles in the vast majority of cases). We believe that a theoretical approach to the characterisation of trap states in the semiconductor is particularly relevant since the experimental study of their impact on the DSSCs efficiency is complicated by the dependence of trap density on the specific chemical treatments that the TiO_2 nanoparticles underwent [30] prior to being assembled in a working device, hence making impossible to characterise the role of traps in a single experiment. Theoretical approaches on the subject, at the same time, generally

overlook the recombination from trap states: in kinetic Monte Carlo simulations of the charge carriers dynamics [50], for instance, it is only electrons in the semiconductor's conduction band that are able to recombine with oxidised adsorbates, notwithstanding that it has been shown how charge recombination can proceed through trap states in the semiconductor [143].

Spectroelectrochemical measurements [169] were able to distinguish two types of traps in a DSSCs: shallow trap states and deep traps. The first kind follow an exponential energy distribution whose typical mean value is between -4.09 eV and -4.16 eV [133, 170, 171] and can be related to grain boundaries or to local interactions at the nanoparticle-electrolyte interface [7]. Deep traps (located ~ 0.5 eV below the conduction band minimum) do not contribute to charge transport inside the semiconductor. This second type of trap states can be identified with oxygen vacancies as these defects are shown to locally increase the electron density [112, 172, 173] while the other possible type of lattice defects (interstitial Ti atoms) do not modify the semiconductor's surface reactivity [174], hence they are not relevant for the charge recombination (CR) process. The defects' relative abundance has been evaluated experimentally for the deep traps and the range $1.7 - 2.7 \times 10^{19} \text{ cm}^{-3}$ has been reported [133, 143, 175]. These relatively high concentrations make the occurrence of CR from defect states likely in real devices.

The expected impact of defects on the device performance is at least twofold, affecting both the amount of energy harvested by each device and the efficiency of the photon-to-current conversion. The first scenario arises because defects offer a lower energy state than those in the CB [176], hence reducing the V_{oc} of the device. The second effect originates from the build-up of a bigger electron concentration

near the semiconductor interface for a given *quasi*-Fermi level than the one present in an ideal (defect-free) semiconductor; this entails a faster charge recombination reaction, since this kinetics is first order in electron concentration. The kinetics of the individual charge recombination step is difficult to describe because it is largely influenced by the energy and distance from the interface of the defect state.

Theoretical studies of the role of defects in TiO_2 were mainly based on an atomistic level modelling of the semiconductor slab [177] and have been thoroughly summarised in Ref. [173]. These studies focus mostly on the electronic structure and geometric structure of the defect and not on its effect on the charge recombination kinetics. To clarify the relation between defect states and recombination kinetics it is desirable to consider a phenomenological model that captures the essence of the charge recombination with or without defects in terms of few parameters with a clear physical meaning. Such model can be used to relate the computational findings to the experimental observation and/or to map the experimental findings into a microscopic model. This type of model also allows the investigation of possible strategies that can be used to suppress the charge recombination channel.

In this chapter a simplified description of the TiO_2 -acceptor interface is employed, with the semiconductor, which may contain defect states, replaced by a tight-binding slab. After introducing our model (in section 5.2.1) we analyse the dependence of the charge recombination kinetics on the parameters of the model considering the possible strategies that can be employed to slow down the charge recombination to the oxidized dye and to the electrolyte (section 5.3.1). We then consider more specifically the effect of the defect energetics and position with respect to the

interface on the measured rate (section 5.3.2) and the effect of bias on the semiconducting electrode in the presence of defects.

5.2 Methodology

5.2.1 Model system

To study the effect of point defects on CR, a minimal model of the semiconductor's electronic structure can include only the conduction band, eventually modified by the presence of a point defect. We therefore considered a tight-binding Hamiltonian H_0 for a simple cubic lattice with nearest neighbour interaction between sites and one orbital per site:

$$H_0 = \sum_{j=1}^{N^3} |j\rangle \alpha_j \langle j| + \sum_{\langle m,n \rangle} |m\rangle \beta \langle n| \quad (4.9)$$

The on-site energy α_j is fixed to a constant value α for ordinary lattice positions, while for the defect site, d , the value α_d is used; the first summation runs over the total number of lattice sites, and the second over nearest neighbours. We considered a slab of $N \times N \times N$ lattice sites repeated periodically in the xy direction. We assumed that the electron acceptor A is electronically coupled only with one site on the surface (denoted as $|1\rangle$), with coupling constant γ . The Hamiltonian of the semiconducting slab interacting with A is therefore

$$H = H_0 + \gamma (|1\rangle \langle A| + |A\rangle \langle 1|) \quad (4.10)$$

A schematic of the system is shown in Figure 20. The electron transfer rate from the semiconductor conduction band to the adsorbate species has been introduced in

chapter 2 (see equation (2.8)), here we simplify the expression for the spectral density, $\tilde{\Gamma}(E)$, consistently with the level of approximation introduced for the Hamiltonian in (4.10):

$$\tilde{\Gamma}(E) = \frac{2\pi\gamma^2}{\hbar} \rho_1(E) \quad (4.11)$$

where $\rho_1(E)$ is the local density of states (LDOS) of the isolated semiconductor on the surface atom connected to the adsorbate. The model Hamiltonian presented in equations (5.1) and (5.2) is reminiscent of the Haldane-Anderson model for chemisorption on semiconductor surfaces [88] although the Coulomb interaction on the adsorbate has not been included herein (see below). A major consequence of the self-energy effects in this model is related to the energy shift of the adsorbate level whenever this is resonant with states in the semiconductor's bands. Albeit it is possible in general to evaluate these effects, this is not the case for the model at hand as it includes only one band in the description of the semiconductor's electronic structure and the acceptor's energy level, E_m , is located well below the conduction band minimum (see Table 3). Instead, the gap states introduced in this model are meant to be phenomenologically related to experimental accounts on defect states characterisation. The model presented in equation (4.9) does not include the Coulomb interaction between different electrons in the semiconductor for simplicity; the standpoint adopted is instead an effective one-body picture for the excess electron present in the conduction band (or in the trap states below it). This picture will be adopted also in chapter 8, where the Coulomb interaction treated by solving an effective one-body Schrödinger equation.

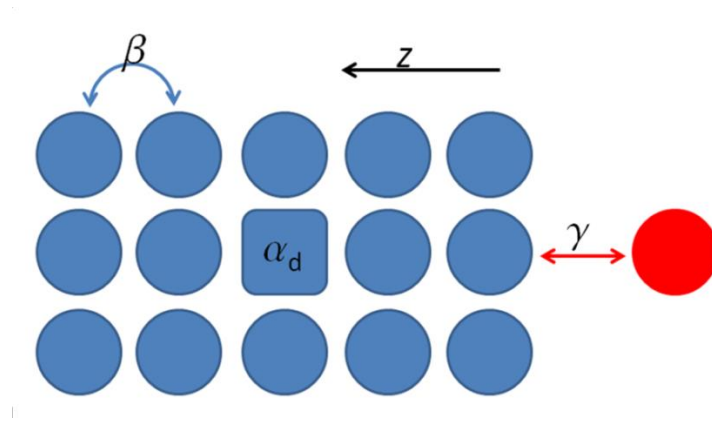


Figure 20. Section of the system studied along the plane containing the adsorbate, the defect position along the z axis is varied with $z = 1$ being the site at the interface interacting with the adsorbate through the coupling γ .

Other quantities required for the evaluation of the rate in equation (2.8) are the Fermi-Dirac distribution and the Franck-Condon term, $F(E_m - E)$, which we express in the high-temperature limit (2.10). The parameters necessary to calculate these quantities are introduced in the next section.

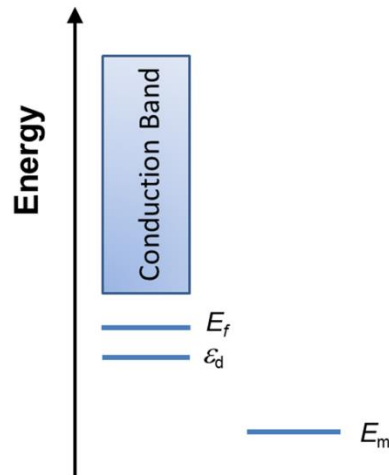


Figure 21. Schematics of the energy levels present in the model: ε_d indicates the defect state energy (related to the on-site energy α_d), E_m is the acceptor state energy level, E_f is the *quasi*-Fermi level position and it is shown here for an arbitrary value in the accessible range.

5.2.2 Model parameters

The slab-acceptor model presented above depends on a set of parameters, listed in Table 3. As we are interested in modelling the charge recombination process taking place in an idealised (TiO_2 based) dye sensitised solar cell, we set the nearest neighbour transfer integral β to -0.35 eV to reproduce the effective electron mass $\mu = 1.22 m_e$ measured for TiO_2 -anatase nanoparticles in [178] ($|\beta| = \frac{\hbar^2}{2\mu a^2}$) when we set the lattice spacing $a = 0.3$ nm. The on-site energy, α , has been fixed at -1.74 eV, so that the band minimum (E_C) is attained close to the experimental value for TiO_2 of -4.0 eV [136]. The introduction of a point defect in the slab is modelled by modifying one of the on-site energies from α to $\alpha_d = -4.2$ eV in order to obtain a state at 0.5 eV below the CB minimum, corresponding to a deep trap state, and $\alpha_d = -3.8$ eV to reproduce the energy of a typical shallow trap (the effect of varying this parameter will be also considered below). The nearest neighbour interaction strength is not changed for the point defect. To study the rate dependence on the distance between the defect and the slab surface, the position of this point defect is varied within the $16 \times 16 \times 16$ semiconductor slab. The introduction of a defect in the semiconductor slab creates an extra state below E_C . This state modifies the charge transfer rate by modifying the function $\tilde{\Gamma}(E)$ that is proportional to the local density of states $\rho_1(E)$ (see equation (5.3)). Figure 22 illustrates how $\rho_1(E)$ is modified as the defect is moved deeper into the semiconductor bulk: the local density of states at the energy of the defect decreases exponentially as the defect is moved away from the interface.

In this model, the different interaction between molecular species and the semiconductor is parameterised by three quantities: the reorganisation energy λ , the adsorbate's free energy variation with the electron transfer E_m and its electronic coupling with the semiconductor slab γ . Each of these parameters has received some attention in the previous literature in the attempt to increase the efficiency of DSSCs [165, 179–182]. The impact of the variation of E_m on the CR lifetime has been studied both for the case of CR to oxidised dye and for the redox couple. In the first case other factors seem to dominate the CR dynamics [50] and the only constraint on the value of E_m for the sensitiser is that it cannot lie below ~ -6 eV: if the dye's HOMO was any lower it would not absorb the majority of the solar radiation, given that the dye's excited state has to lie above the semiconductor CB minimum. For the most common redox pair (I^-/I_3^-) $E_m = -4.9$ eV [144] and so the range of value considered for E_m is between -6 and -4.8 eV. When we present the rates we allow the reorganisation energy to vary between 0.4 and 2.1 eV.

Same results will also be presented for selected (E_m, λ) pairs corresponding to specific experimental conditions. The value $E_m = -5.2$ eV is the optimal position for the oxidised dye energy level according to Ref. [29] and the value $E_m = -5.1$ eV is the value for the prototypical cobalt (III/II) tris-bipyridyl complex ($[\text{Co}(\text{bpy})_3]^{3+/2+}$). The latter is an example of redox couple able to generate a bigger V_{OC} (with a more negative E_m) than the popular iodide/triiodide redox couple. The reorganisation energy for cobalt complexes is characterised by a particularly high contribution of the internal degrees of freedom (involved in the transition from high spin to low spin

configurations) hence we assume that the value $\lambda = 1.41$ eV obtained by Ondersma and Hamann [143] for similar Co-based complexes can be used in conjunction with $E_m = -5.1$ eV. Iodide/triiodide has a bigger reorganisation energy ($\lambda = 1.8$ eV) [183], while for the oxidised dye we pick $\lambda = 0.9$ eV, although chemical modifications of the dye also can impact on this value [179]. The values selected for the reorganisation energy are based on the nuclear relaxation of the molecular species involved and of the dielectric relaxation for the solvation shell surrounding them; as such the contribution of lattice relaxation has been disregarded thus far. While this approximation is typically justified when the electronic state on the semiconductor are delocalised, it might break down when the initial state is located in a ‘deep trap’ as the one considered herein. As an evaluation of these effects has not been attempted previously for TiO_2 but only for late transition metals oxides [184], we neglect this contribution to the total reorganisation energy as its estimate would be completely arbitrary.

We set $\gamma = 0.001$ eV so that the charge recombination lifetime computed for $E_f = -4.1$ eV, $E_m = -4.9$ eV and $\lambda = 1.8$ eV (parameters compatible with charge recombination to electrolyte under illumination) produces a CR lifetime, $\tau = 1/k$, of 10 ms, close to the experimental observation [25]. It is however obvious from equation (4.11) that this parameter is only a prefactor of the total rate and it does not influence the main points that will be discussed in the rest of the chapter.

In a real device the *quasi*-Fermi level E_f spans the range from -4.9 eV to -4.1 eV depending on the illumination conditions [39]; in this study we focus on the CR under illumination, hence fixing E_f to -4.14 eV. In a real device this value may

change by modifying either the electrolyte or the sensitiser, however we do not consider this effect here.

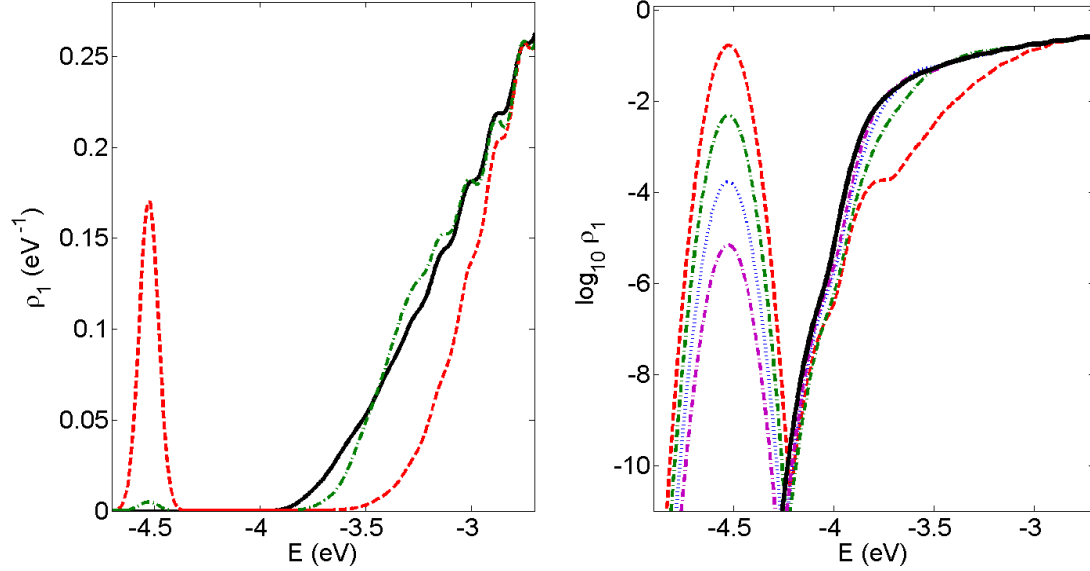


Figure 22. The local density of states for a simple cubic lattice of size $16 \times 16 \times 16$ evaluated at the adsorption site is plotted on a linear scale (left panel) and on a logarithmic scale (right panel). Curves shown are obtained for a slab with no defect (black line), or with defect position $z = 2$ (red dash line), $z = 3$ (green dash-dot line); on the right also defects in positions $z = 4$ (blue dots) and $z = 5$ (purple dash-dots) are considered. Gaussian broadening is set to 0.05 eV and $\alpha_d = -4.2$ eV.

Table 3. Parameters employed for defining the Hamiltonian matrix and the charge recombination kinetic constant.

Symbol	Definition	Numerical values (in eV)
E_C	conduction band minimum	-4.04
E_m	acceptor's energy level	from -4.9 to -5.2
E_f	<i>quasi</i> -Fermi level	-4.14
ε_d	defect energy	-4.53 (deep trap), -4.2 (shallow trap)
λ	reorganisation energy	from 0.9 to 1.8
γ	slab-adsorbate coupling strength	0.001
α	on-site lattice energy	-1.78
β	nearest-neighbour interaction strength	-0.35
α_d	defect on-site energy	-4.2 (deep trap) or -3.8 (shallow trap)
β_d	defect interaction strength	-0.35

5.3 Results

5.3.1 Effect of the redox potential and reorganisation energy

We analyse the charge recombination lifetime in a map containing this quantity as a function of the two parameters E_m and λ whose range has been previously described. The data in Figure 23 also indicate a dotted line in correspondence with the I^-/I_3^- redox couple Fermi level. The two panels shown refer to the CR proceeding from a defect-free semiconductor slab (top panel) or from a slab with a deep trap state ($\varepsilon_d = -4.5$ eV) in the third slab layer (bottom panel). In both panels the round marker has been positioned at $\lambda = 0.9$ eV and $E_m = -5.2$ eV as reference for a “typical” dye in this parameter space. Comparing the recombination lifetimes reported in Figure 23 we note how the introduction of a single defect has a large impact on the CRR kinetics, accelerating the electron transfer by roughly three orders of magnitude. This effect is not unexpected: experimental reports relate a TiCl_4 based treatment, employed to reduce the defect density at the nanoparticle interface, with a 20-fold CRE lifetime increase at fixed charge density in the photoelectrode [29]. Since lattice defects can act as electron traps, it is reasonable to assume that this chemical treatment would also locally reduce the electron density at the interface; the experimental estimate can then be considered as a lower bound on the actual recombination lifetime increase.

If we seek to slow down the charge recombination by modifying the parameters E_m and λ , from Figure 23 we see that depending on whether a defect state is present or not the optimised value for these parameters might be different. In a defect-free semiconductor the charge recombination becomes slower if we decrease E_m or λ or

both (as shown by the arrow in the top panel of Figure 23). E_m is closely related to the HOMO energy and cannot be arbitrarily decreased without compromising the light harvesting characteristics of the dye. The LUMO of the dye needs to be few tenths of electronvolts above E_C for efficient injection so that the lowering of the HOMO shifts the onset of light absorption to the blue, reducing the fraction of photon transformed into free charges. The reorganisation energy can also be modulated by modifying the chemical structure of the dye: long alkyl chains can reduce the interaction with the first solvation sphere, hence decreasing λ . However, also this process cannot be pushed too much as bulky substituents reduce the surface coverage and may reduce the rate of charge neutralization of the dye from the redox couple.

If a defect state is present at 0.5 eV below the CB minimum (bottom panel of Figure 23), E_m and λ should be both increased, with respect to the typical values (highlighted by the round mark) to slow down charge recombination. Both in the case with and without defect the typical values of E_m and λ are such that the rate of charge recombination is close to its maximum value. Consequently, small changes of these parameters do not cause dramatic changes in the rates. For example, if we increase E_m by 0.2 eV the CR will be slower only by a factor of 4. Making the sensitizer's E_m less negative is a strategy that has been adopted in recent experiments: in the most efficient DSSC to date [4] the HOMO energy of the porphyrin based chromophore has been increased in comparison with a dye taken as a reference by ~ 0.2 eV leading to a slower CR by a factor between 2 and 10. Unfortunately, this scheme is not likely to be iterated indefinitely to improve DSSCs performances

because an offset between the electrolyte's and the oxidised dye's energy levels will still be necessary to drive the dye regeneration reaction. Therefore in the presence of defects the energy alignment is hard to improve, also considering that one of the goals of DSSCs is to keep the electrolyte redox potential as low as possible to maximise the open-circuit voltage V_{oc} .

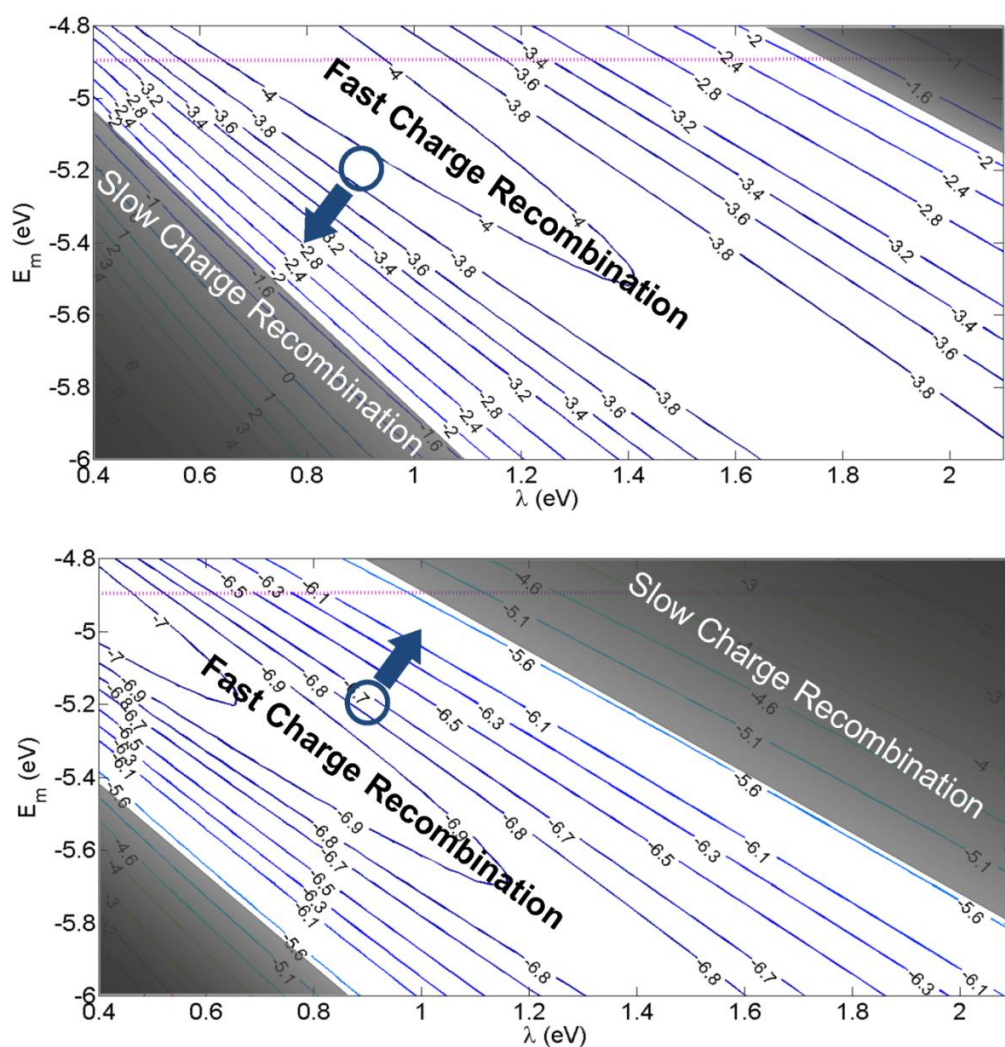


Figure 23. Contour plot of the logarithm of the charge recombination lifetime, $\log_{10}(\tau/\text{second})$, as a function of E_m and λ for a defect-free slab (top panel) and with a sub-surface defect (bottom panel), $\alpha_d = -4.2$ eV $z = 3$. The symbol indicates a set of reference parameters for a “typical” dye and the arrow the best direction to slow down the recombination rate.

Many groups are attempting to replace the Γ/I_3^- redox couple ($E_m = -4.9$ eV) with alternatives at lower redox potential, such as Co(II/III) ($E_m = -5.1$ eV). The map in Figure 23 shows that this change will always increase the charge recombination to electrolyte in the presence of a defect, unless the reorganisation energy for the electron transfer to the electrolyte is bigger than the value for the Γ/I_3^- couple. This is extremely unlikely as the reorganization energy decreases with the increase of the size of the redox species. For this reason (and considering the map in the presence of defect to be closer to the actual situation in DSSCs), the lowering of E_m , which would be desirable to increase V_{OC} , may be counterproductive as it will also increase the rate of charge recombination to the electrolyte. It must be remembered however that different electrolytes may have different interaction with the electrode (here we are keeping the relevant coupling term γ constant throughout). It may be possible to improve the energetics of the electrolyte without increasing the charge recombination rate if the electrolyte is designed to have little affinity for the TiO_2 surface (i.e. smaller values of γ).

The two panels in Figure 23 represent two idealized situations but in practice not all dyes are equally close to a defect and the charge recombination rate fluctuates from dye to dye as a result of the different relative position of the defect state. These effects are analysed next.

5.3.2 Defect characterisation

In this section we study the effect of the defect energy and position on the charge recombination rate. The energy of the point defect is controlled by the parameter α_d of the Hamiltonian. For convenience we report in Figure 24a the energy ε_{\min} of the

lowest eigenstate of the Hamiltonian in (5.1) as a function of the parameter α_d . For $\alpha_d < -1.8$ eV a defect is formed below the conduction band minimum E_C .

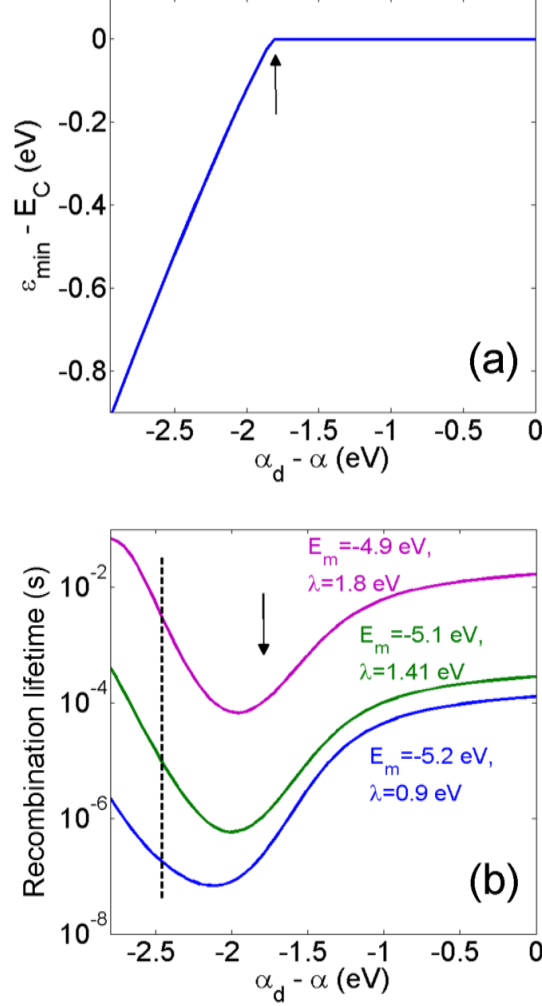


Figure 24. (a) Value of the smallest eigenvalue for the lattice energy spectrum (which coincides with the smallest value between E_C and ε_d) relative to the CB minimum as the defect on-site energy α_d is varied below the regular lattice point's on-site energy α . (b) CR lifetime for $E_m = -4.9$ eV, $\lambda = 1.8$ eV, $E_m = -5.1$ eV, $\lambda = 1.41$ eV, and $E_m = -5.2$ eV, $\lambda = 0.9$ eV as a function of the defect on-site energy; black arrow indicates when the defect energy ε_d is inside the CB, dashed vertical line is positioned at the surface state energy. Defect is positioned in the third slab layer.

Figure 24b illustrates the dependence of the charge recombination lifetime on the parameter α_d controlling the defect energy for three representative sets of the

parameters (E_m , λ). The defect is positioned in the third layer from the interface. The lifetime reaches a minimum (and the charge recombination rate a maximum) for $\alpha_d - \alpha \approx -2.0$ eV, corresponding to a defect energy ~ 0.2 eV lower than the conduction band minimum. This maximum recombination rate occurs at energies (values of α) where the Franck-Condon factor has a maximum. The position of such maximum does not change much for the different parameters E_m and λ used to illustrate this dependence. Moreover, the reduction in the recombination lifetime at this energy is rather small, smaller than the difference caused by varying E_m and λ . An important consequence of the result in Figure 24b is that the exact determination of the defect energy is not very crucial for the description of the charge recombination kinetics. Modifying the defect energy by tenths of electronvolts only changes the lifetime by less than one order of magnitude. Interestingly, the defect still accelerates the charge recombination when it is within the conduction band because it enhances the local density of states near the dye.

In Figure 25 we report the lifetime for charge recombination reactions as a function of the defect position for three sets of the (E_m , λ) parameters and $\alpha_d = -3.8$ eV. The presence of a defect close to the interface increases the value of ρ_1 for energies below the conduction band edge (see Figure 22) making the charge recombination reaction faster. As discussed above, defects few tenths of electronvolt below the conduction band promote faster recombination also because the Franck-Condon factor at that energy is at its maximum. By moving the defect deeper into the semiconductor bulk we progressively recover the recombination lifetime obtained for the defect-free case, which are shown in Figure 25 by horizontal lines. The behaviour

such as that reported in Figure 25 is similar to what is observed in donor-bridge-acceptor systems with increasing length of the bridge [185]. The portion of TiO_2 that the electron needs to cross to recombine with the dye acts as a tunnelling barrier.

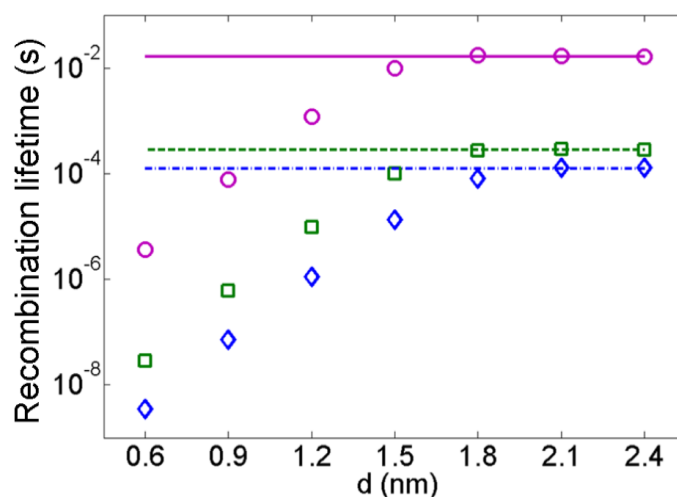


Figure 25. Charge recombination lifetimes as a function of the defect ($\alpha_d = -3.8$ eV, $z = 3$, $\varepsilon_d = E_c - 0.17$ eV) position d ($d = \text{layer number} \times \text{lattice spacing}$) for $E_m = -5.2$ eV, $\lambda = 0.9$ eV, (circles) $E_m = -5.1$ eV, $\lambda = 1.41$ eV (squares) and $E_m = -4.9$ eV, $\lambda = 1.8$ eV (diamonds). Horizontal lines represent the respective CR lifetime for the defect-free case.

The relatively high abundance of trap states reported in the introduction has been identified experimentally [186] as the reason for the multi-exponential kinetics for the charge recombination to oxidised dye molecules measured by spectroscopic techniques. Therefore, the defect spatial distribution is required to assess the impact on the charge recombination rate, at least in the proximity of the interface. Selloni *et al.* [187] have pointed out how oxygen vacancies in the first two atomic layers are not energetically stable and defects in the second layer are spontaneously filled; the favourable occurrence of defects in sub-surface positions has been then validated experimentally [188]. Given this characterisation of the anatase surface, we assume a

uniform distribution of defects within the semiconductor slab, except in the first two layers, which are taken to be defect-free.

The relative defect abundance provided by experimental sources (between 1.7 and $3.0 \times 10^{19} \text{ cm}^{-3}$ depending on the experimental technique [133, 143, 175]) translates into a defect occurrence of 2-3 per (256×16) slab, which implies the presence of a defect every five atomic layers approximately. Combining the information on the defect concentration and the range of rates shown in Figure 25, we conclude that an extremely large range of charge recombination rates is to be expected. Indeed, as reported in Ref. [189], the CR reaction is characterised as a ‘highly non-exponential process’ whose description required up to five time constants spanning six orders of magnitude. In this regard we can conclude that reducing the number of trap states is a viable strategy to reduce the charge recombination losses in dye sensitised solar cells. A systematic study of chemical treatments that can reduce the number of defects in the TiO_2 nanoparticles has been carried out recently by O’Regan and co-workers [30].

5.3.3 Charge recombination for a slab with a surface bias

The rate in equation (2.8) can be partitioned into two contributions by dividing the integration domain into two subsets; the first ranging from $-\infty$ to E_C takes into account any contribution from the defect state, the second includes energies above the conduction band minimum E_C . In this section we aim at identifying which of the two contributions to the charge recombination lifetime is predominant as the conduction band edge is allowed to be shifted in comparison with the reference value of -4.0 eV vs. vacuum. A shift in the conduction band edge energy is obtained in our

model by modifying the on-site energy α in comparison with the reference value in Table 3. It is, in fact, possible for the small nanoparticles used in DSSC to neglect the effect of local CB bending, hence, by changing the particular experimental conditions (pH, applied potential) the whole band is shifted [40].

The CR lifetimes shown in the three panels in Figure 26 are obtained using the reference values of E_m and λ discussed earlier. In each panel the total CR lifetime is evaluated as a function of the conduction band shift, together with the separate contributions from conduction band states and from the defect state. Data in Figure 26 show how the defect state dominates the charge recombination lifetime for values of conduction band edge near the reference value of -4.0 eV and for all values above it, whereas the conduction band states become relevant for the charge recombination reaction only when the CB minimum is shifted by 0.3 eV below the value taken as a reference in this work. This shift of the CB edge can be achieved by modifying the concentration of lithium ions in solution, as reported in Ref. [190].

Comparing the three panels in Figure 26 we can also notice how the increase in reorganisation energy (from top to bottom) makes the CR from the defect state progressively slower. Conversely, for the top panel, where the reorganisation energy is smallest, the defect state determines the CR lifetime over a wider range of CB shifts, owing to the favourable alignment between the Franck-Condon term, as previously pointed out, and also because the Franck-Condon term is more peaked at small λ , hence reducing the contribution from conduction band states to the charge recombination rate.

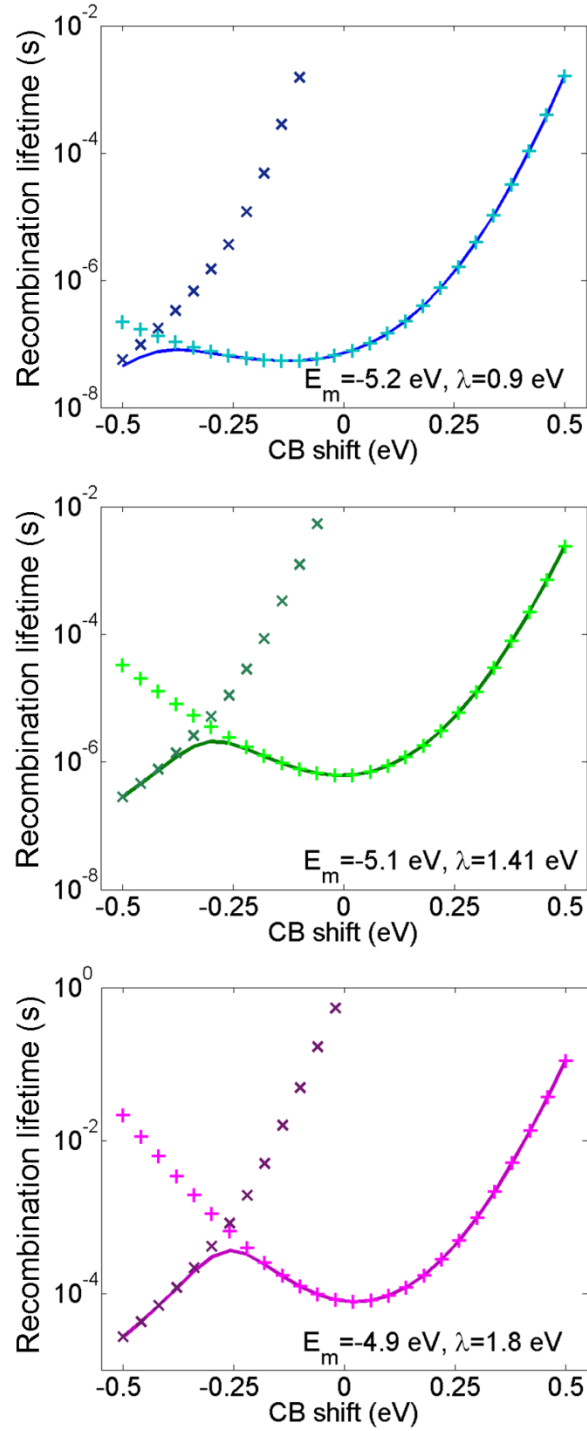


Figure 26. CR lifetimes for different acceptors as a function of the conduction band (CB) shift. Rates are evaluated over the whole energy range (lines), for energies above the conduction band minimum (' \times ' symbols), or taking into account only CR from the defect state ($\alpha_d = -3.8$ eV, $z = 3$) ('+' symbols).

5.4 Conclusions

We have presented a phenomenological model for the study of the charge recombination process in dye sensitised solar cells, based on the tight binding description of a simple cubic lattice, whose parameters were derived from known physical properties of the TiO_2 conduction band, and on a Marcus-type rate equation for the non-adiabatic electron transfer. The choice of this level of theory has proved necessary in order to describe effects such as the position and energy of the defect and to provide a “map” of the charge recombination rate for different system parameters.

The main findings of this analysis can be summarized as follows:

- (i) Electron trap defects in realistic concentration and for a realistic energy range increase the charge recombination rate.
- (ii) For realistic energetic parameters of the typical DSSC dye the CR rate is close to a maximum (with or without defect included). At the same time, within a realistic range of dyes’ energetic parameters (free energy, reorganisation energy) it is very difficult to devise a strategy that decreases this rate considerably if the semiconductor is not changed.
- (iii) If an optimization of the energetic parameters of the dye is attempted, the “ideal” parameters will be different depending on whether the dye is close to a defect or not. In other words, considering that the distance between a dye and the closest electron trap is very broadly distributed, it is not possible to minimize the CR rate for all adsorbed dyes (i.e. those adsorbed far and close to a defect) at the same time.

- (iv) The exact energy of the electron traps (within a physical range) does not change significantly the phenomenology. However, the charge recombination component from the electron trap decreases exponentially with the distance of this trap from the interface. The model justifies therefore the very broad range of charge recombination rates that is reported experimentally.
- (v) Lowering the CB edge with suitable additives does lower the importance of the defects on the CR process. On the other hand this is detrimental for the open circuit voltage which decreases with the lowering of the CB edge.

Although the results above may indicate that the current DSSC devices can be only improved by reducing the number of electron trap states in titania, there is another possible route for their improvement implicitly suggested by our model. All rates computed in this chapter assume for convenience the same electronic coupling between the dye (or electrolyte) and the electrode (the parameter γ). It was shown repeatedly, especially in the field of molecular electronics [191, 192], that this interaction can be tuned in many different ways. The use of donor-acceptor dyes is a common strategy to reduce selectively the electrode/dye coupling for the charge recombination [193]. We have recently proposed a strategy to design dyes bases on symmetry rule that guarantees a vanishingly small value of γ (while leaving the charge injection rate unaffected) [194] and it may be possible to devise other mechanisms, based on controlling the semiconductor-dye interaction, that can be used to lower the charge recombination rates.

Chapter 6: Using orbital symmetry to minimise charge recombination

6.1 Introduction

In this chapter and in the next we bring to fruition the molecular insight stemming from our theory of charge transfer developed in chapter 2. Here we present a strategy for controlling the charge recombination rate by minimising the coupling between semiconductor and the relevant molecular orbital on the oxidised dye. As such, the strategy does not affect the charge injection process, which involves instead the LUMO orbital on the neutral dye. This strategy is implemented by imposing specific symmetry constraints on the chromophore moiety and its connection to the semiconductor and by providing few realistic examples. The validity of this approach is then tested by considering similar molecules (with an identical chromophore fragment) that do and do not fulfil the symmetry requirements previously specified.

An ideal dye for dye sensitized solar cells (DSSC) should inject an electron as fast as possible into the semiconductor nanoparticle it is connected to and, in its oxidized form, it should be neutralized as slowly as possible by the electrons in the conduction band of the semiconductor [7, 195]. This latter charge recombination process is always very strongly favoured thermodynamically and the only way to limit the charge recombination is to hamper its kinetics. A number of synthetic groups are designing and preparing dyes that, when oxidized, should recombine as slowly as possible with the electrons in the semiconductor, while maintaining a good charge injection efficiency [14, 196]. The strategy commonly used is to prepare molecules that, when adsorbed on the semiconductor, have their HOMO density localized as far

as possible from the semiconductor and the LUMO density localized as close as possible to it. The resulting dyes have a clear donor-acceptor structure so that, in their excited state, there is a partial charge transfer character with negative charge closer to the semiconductor and, in the oxidized state, the HOMO (positive charge) is spatially separated from the semiconductor. The poor overlap between the HOMO of the dye and the conduction band orbitals of the semiconductors should slow down the recombination, which depends, among other things, on the square of the electronic coupling between the dye's HOMO and semiconductor's orbitals. This strategy led to the realization of DSSC with up to 10% efficiency [197]. We show in this chapter that there is an alternative way of designing organic dyes that have strong coupling with the electrode when they are excited and very weak coupling when they are oxidized and this is based on few elementary ideas from orbital symmetry and through bond electron tunnelling in donor-bridge-acceptor (D-B-A) systems.

In the traditional D-B-A systems studied since the late 1970s a donor fragment is chemically connected to an acceptor fragment through a chemical "bridge". The donor fragment can be excited by radiation and, in its excited state, it can donate an electron to the acceptor [198]. It was realized long ago that a suitable design of the D-B-A system may make the charge separation reaction ($D^*-B-A \rightarrow D^+-B-A^-$) symmetry allowed while the charge recombination reaction ($D^+-B-A^- \rightarrow D-B-A$) can be symmetry forbidden. Such a design, extensively investigated in Refs. [199, 200], promotes long lived charge separation states and relies on initial and final states of different symmetry (i.e. transforming according to different representations, in the language of group theory). Using an orbital picture, if the charge recombination can

be seen as a transfer from the LUMO of A to the HOMO of D, these two orbitals must have different symmetry to make the transition symmetry-forbidden and therefore very slow. We can naively try to extend the same idea to the field of DSSC assuming that the role played by the acceptor fragment in isolated molecules is played by the semiconductor in DSSC. This is not an accurate analogy as the acceptor states in DSSC are a continuum of semiconductor states, a fraction of which always have the right symmetry to be coupled with the HOMO of the donor (i.e. the chromophore in this case). However, if a bridge moiety (the anchoring group or anchor plus linker group) connects the chromophore and the semiconductor, the dye-semiconductor coupling is mediated by the bridge, i.e. it is proportional to the product of the coupling between dye and bridge and between bridge and semiconductor, as we have shown in equation (2.34). As we have seen, there is no symmetry rule for the latter, but we can hope to design a bridge that, for symmetry reasons, is not coupled to the HOMO of the dye. We plan, in other words, to design a donor-bridge-semiconductor system that “isolates” the HOMO of the dye from the semiconducting states and we will use orbital symmetry to do so.

6.2 Symmetry analysis

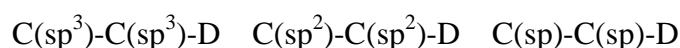
We proceed to define more formally the problem and the assumptions made:

- (i) The system is composed by a chromophore D, connected to the surface of a semiconductor S, via a bridge B.
- (ii) To make the chemistry more defined (and aligned with the current dye development) the dye is an organic conjugated dye and the bridge is a

chain of sp , sp^2 or sp^3 carbon atoms saturated by hydrogen and terminating with an anchoring group ($-COOH$).

- (iii) The bridge is at least 2 atoms long to prevent through space coupling.
- (iv) We wish to define the symmetry conditions that make the coupling of the HOMO orbital of D with the orbitals localized on B null (or very small).
The coupling between the LUMO of D and the orbitals localized on B must not be null by symmetry.

According to the theories of through bond tunnelling, an efficient coupling through the bridge is observed if there is a coupling between the orbital localized on the donor D and the highest occupied and lowest unoccupied orbitals that can be localized on the bridge. These bridge orbitals are either the σ or π bonds between carbon atoms if the bridge carbon chain is saturated or unsaturated respectively. Given hypothesis (ii), there are three possible structure of the bridge in the vicinity of the dye:



If D is a conjugated organic molecule, i.e. it contains a plane of symmetry, its HOMO and LUMOs will be antisymmetric with respect to the symmetry plane of the molecule (σ_{yz} in Figure 27). The coupling with the saturated bridge (sp^3) will be very small by symmetry regardless of the symmetry of the orbitals on D. In this case it is not possible to hope for a large coupling of LUMO and small coupling of HOMO: the tunnelling matrix element will be small in both cases and promoted by more complicated through space interactions and hyperconjugation. Saturated bridges are also unsuitable because they generate more flexible structure whose geometry at the

interface is more difficult to control and design, as shown by calculations in chapter 3.

For the $C(sp^2)-C(sp^2)-D$ and $C(sp)-C(sp)-D$ case, the coupling between bridge and dye is always allowed in absence of additional symmetry elements beyond the plane of the D backbone. Either by adding a C_2 axis or another symmetry plane (no inversion centre is possible), the largest symmetry group will become C_{2v} .

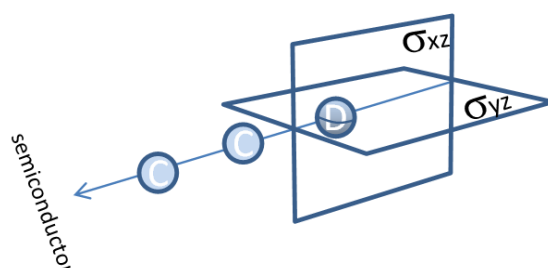


Figure 27. Sketch of the symmetry elements present in the molecular systems considered.

Condition (iii) can be verified if the molecule has C_{2v} symmetry and the HOMO and LUMO are antisymmetric and symmetric with respect to the plane (σ_{xz}). In the case of $C(sp)$ chains the π orbitals on the bridge carbon atoms are strictly not coupled with the antisymmetric (with respect to σ_{xz}) HOMO orbital. For the case of $C(sp^2)$ chains the symmetry is lowered by the chain and only the coupling between the p orbital on the nearest carbon atom and the chromophore will be (approximately) null. In both cases, the bridge must be connected to an atom that lies on the symmetry plane perpendicular to the plane of the backbone of D. In the following section we will provide examples with sp^2 bridges which are more easily achievable synthetically and less likely to give other problems (stability on the semiconductor, photostability, etc.).

6.3 Application to realistic dyes

To exemplify our reasoning, Figure 28 shows three simple aromatic molecules that have been modified to generate efficient dyes for DSSC (pyrene [201], azulene [202] and fluorene [203]) and are chosen because they have a symmetry plane (illustrated) perpendicular to the conjugation plane and crossing at least one carbon atom of the backbone that can be connected to a bridge (this carbon atom is also indicated). As the molecular orbitals (MOs) of this molecule are either symmetric or antisymmetric with respect to this plane, some of the MOs (the antisymmetric ones) will have a nodal plane in correspondence with these carbon atoms. The HOMO of pyrene, azulene, fluorene happens to be antisymmetric with respect to the indicated symmetry plane, i.e. the orbital density on the carbon atom crossed by the symmetry plane is null. A bridge that connects the dye with the semiconductor via that carbon atom has the minimum possible coupling with the HOMO of the molecule.

The same three dyes have a symmetric LUMO with respect to the same plane¹, i.e. a bridge between them and the semiconductor connected to the same carbon will couple strongly the LUMO and the semiconductor and very weakly the HOMO and the semiconductor. Before quantifying this effect it should be noted that the selected dyes are chosen for their simplicity and not their efficiency as dyes (they adsorb light at too high energy). The rest of the discussion relies on the assumption that these dyes can be chemically modified to improve their light absorption while retaining the same orbital symmetry characteristics (the likelihood of this is discussed below).

¹ The LUMO and LUMO+1 of unsubstituted pyrene are antisymmetric and symmetric respectively. Upon substitution with the bridge the (*quasi*) symmetric orbital is stabilized to become the lowest unoccupied orbital.

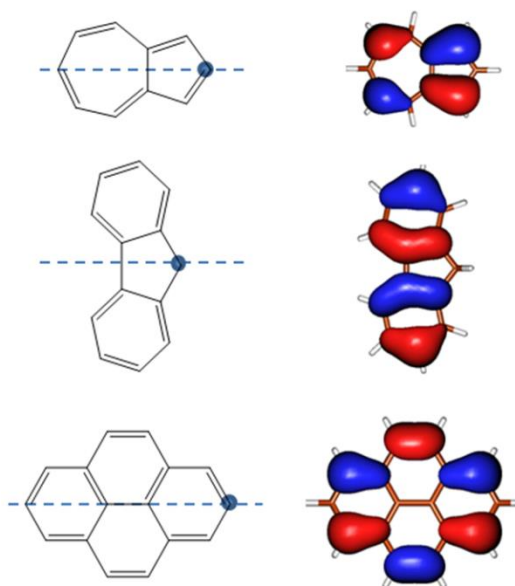


Figure 28. The azulene, fluorene, pyrene molecules with an illustration of their symmetry plane which crosses a carbon atom that can be connected to a bridge. The HOMO of these molecules is antisymmetric with respect to this plane.

It is not possible to completely prevent the coupling between bridge and some orbital of the dye because of through space coupling. To minimize this coupling we therefore consider a “thin” bridge with chemical structure $-\text{CH}=\text{CH}-\text{COOH}$, which is very common in DSSC (the carboxylic acid is the most common anchoring group used in DSSCs). It was repeatedly shown that a good coupling between the dye and the semiconductor is determined by the dye’s orbital weight on the atoms of the carboxylic group [116, 155]. Connecting this bridge to the dye through the special symmetry point identified above should (i) mix the original LUMO density with the bridge orbital and generate good orbital density on the carboxylic group and (ii) leave the HOMO almost unchanged with negligible orbital density on the carboxylic group. Figure 29 shows that this is exactly what happens. The orbital symmetry of the aromatic part of the molecules remains the same as in the unsubstituted molecules, therefore creating a large LUMO weight and a negligible HOMO weight

on the carboxylic bridge. To be more quantitative, we can define a quality factor Q , as the ratio between the orbital density on the carboxylic acid on the LUMO divided by the same quantity computed for the HOMO:

$$Q = \frac{\sum_i |c_i^{LUMO}|^2}{\sum_i |c_i^{HOMO}|^2} \quad (6.1)$$

when Q is close to 1, HOMO and LUMO are similarly coupled to the electrodes, with $Q \gg 1$ the LUMO has a much stronger coupling with the electrode than the HOMO. Q represents the propensity of insulating the HOMO from the semiconductor (with respect to the LUMO) intrinsic in a dye. This quantity is 575, 168 and 2106 for azulene, fluorene and pyrene, respectively, indicating a very strong localization of the LUMO on the carboxylic group in comparison with the HOMO.

To further illustrate the point we repeated the calculation for pyrene with the same bridge substituted in the two asymmetric positions (2 and 3 in Figure 29). The effect of “HOMO isolation” completely disappears and the quantity Q drops to 4 and 8 when the asymmetric substitution is considered.

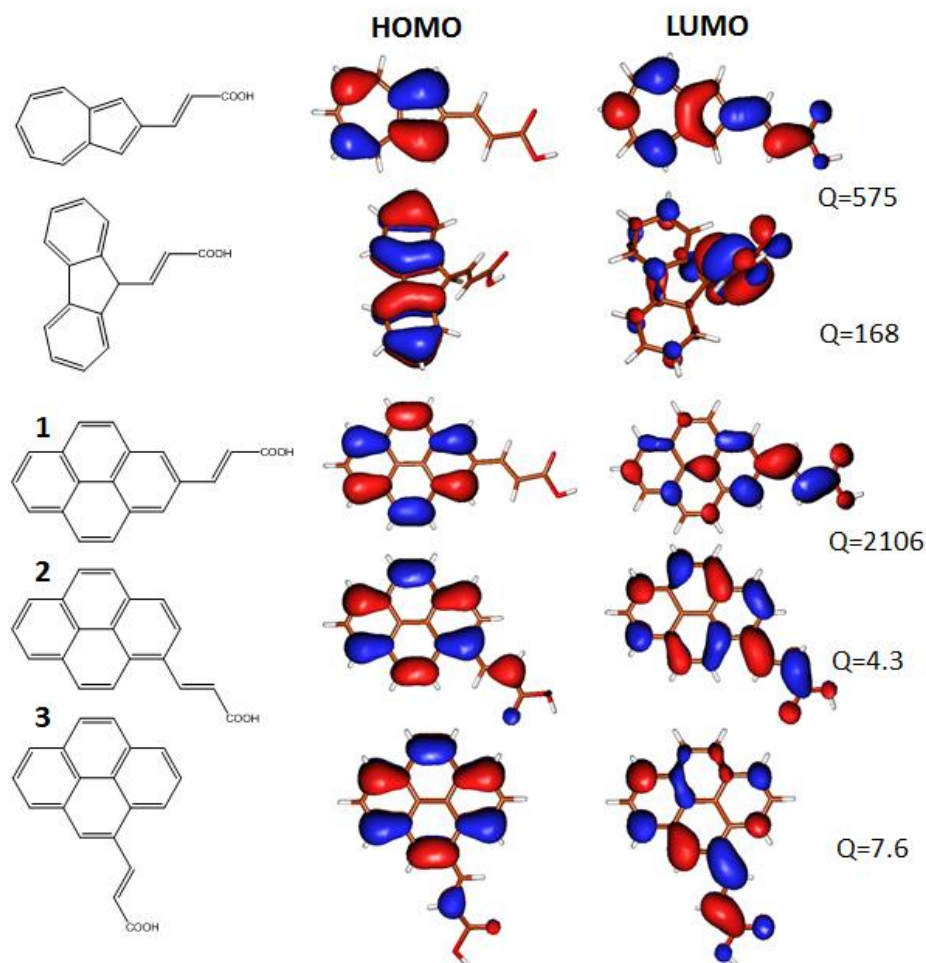


Figure 29. Chemical diagrams and HOMO and LUMO plots of three molecules substituted with a bridge in the symmetry position that isolates the HOMO from the bridge (top three rows). Alternative, non-symmetric substitutions of pyrene that do not isolate the HOMO from the bridge. The parameter Q is discussed in the text.

We consider the case of pyrene to provide an even more quantitative analysis. By using the computational method of chapters 2 and 3 to estimate the charge recombination rate in DSSC we can compare the charge recombination rate of pyrene substituted in positions 1, 2 and 3. This calculation relies on the explicit calculation of the coupling between the dye and the semiconductor (TiO_2) and goes well beyond the simple analysis presented so far. As we discussed in chapter 3 the

actual estimate of the rate is affected by a number of assumptions but the relative recombination rate is rather robust for rigid molecules with sp^2 bridges. The expression for the spectral density used herein is given in equation (2.29) and its computational implementation is identical to that exposed in chapter 3. Using the parameters given in Table 4 (as well as a position for the conduction band minimum at -4.0 eV and a *quasi*-Fermi level located 0.14 eV below, consistently with the estimate provided in section 3.2.3.5) we find that the recombination rate for the asymmetric (“wrong”) substitution is ~ 1400 and ~ 360 times faster than the rate computed when the best symmetric position of the bridge it is used (see Table 4). By using symmetry, the charge recombination rate can be reduced by 2 to 3 orders of magnitude. It is essential for this analysis to be valid that the dye stands perpendicularly to the surface so that through bond tunnelling is much more probable than through space tunnelling (more flexible bridges do not allow this type of control).

Table 4. Energy difference, ΔE , reorganisation energy, λ , and recombination rates for the three pyrene isomers considered; the ratio of the rates relative to the smallest one (k_{CRI}) is also shown.

	ΔE (eV)	λ (eV)	k (s $^{-1}$)	k/k_{CRI}
Pyrene 1	-5.55	0.48	0.43	-
Pyrene 2	-5.46	0.46	625	6.88×10^{-4}
Pyrene 3	-5.50	0.47	156	2.76×10^{-3}

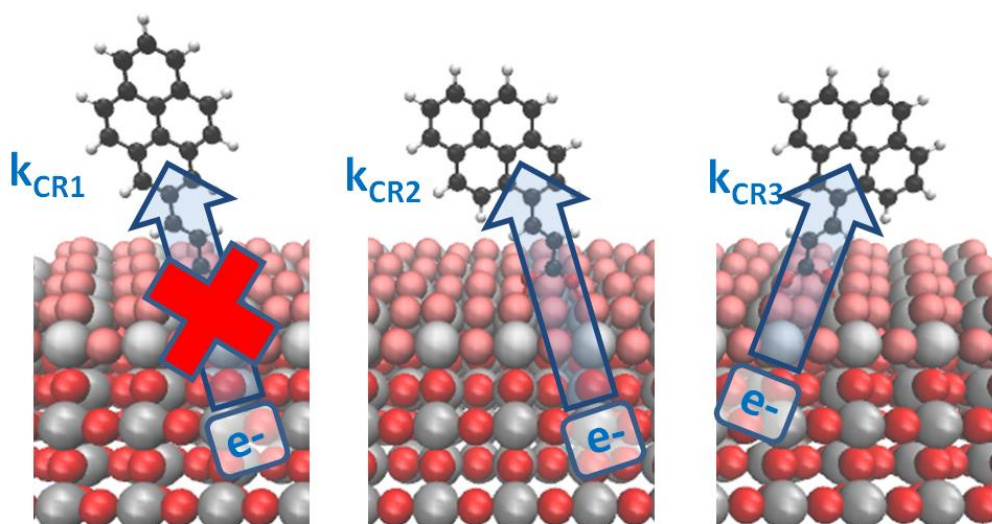


Figure 30. Schematics of the adsorption of three substituted pyrenes on anatase (101). The computed charge recombination rate is more than two orders of magnitude lower for the symmetric pyrene 1, for which the charge recombination is virtually forbidden.

6.4 Conclusions

Symmetry considerations are generally very robust [204] and the concept proposed here is worth considering for the actual design of new dyes. Once the symmetry considerations are satisfied, i.e. there is an atom of the dye that can be connected to the bridge and lies on a symmetry plane perpendicular to the molecular plane; the likelihood that the relevant orbitals have the right symmetry is very high. Very roughly we could think that the HOMO and LUMO of these molecules would be antisymmetric and symmetric respectively with respect to this plane about one fourth of the times but, as the symmetry of these two orbitals is often different from each other (i.e. one symmetric and the other antisymmetric), the actual probability is closer to one half. For this reason it is not essential for the proposed model that the molecules provided in this work are not the ideal dyes because in all three cases they can be substituted symmetrically to modify the energetics of the HOMO and LUMO and it is extremely likely that some (if not all) of them will retain the desirable MO

symmetry. Another advantage of this strategy is that it does not require complicated theory to support the design of new dyes and additional complication in the electronic structure models (e.g. dispersion and image charge interaction) are not expected to alter the relative advantage of using these symmetrically substituted dyes. The only crucial assumption is that the dye stands perpendicularly to the surface so that through bond tunnelling is much more probable than through space tunnelling. The effect of the surrounding environment on the proposed strategy is expected to be marginal: solvent effects in particular have been elucidated in the recent study by De Angelis and co-workers [62] by explicitly including acetonitrile molecules in the DFT simulation box. While the impact on the interfacial energy level alignment was substantial, modifications in the adsorption geometry in the sensitizer were limited to the anchoring group/bridge molecular portion, and therefore are bound to equally affect the different sensitizers for which the comparison to test the strategy was carried out.

In conclusion, we have proposed in this chapter that suitably designed symmetric dyes can be used in dye sensitized solar cells to reduce the charge recombination rate by 2 to 3 orders of magnitude.

Chapter 7: Exploiting Quantum Interference in Dye Sensitised Solar Cells

7.1 Introduction

The expression for the charge recombination rate derived in chapter 2 has been used throughout the following chapters without imposing on the molecular system the partition into bridge and chromophore sub-units. In this chapter we analyse specifically the role of the bridge unit connecting the semiconductor surface with the chromophore unit in the organic sensitiser. This type of structure is quite common among the organic dyes that have been employed in the field of DSSCs [6], therefore we explore an optimised design of the bridge portion, able to slow down the charge recombination process, might have a big impact on the quest for more efficient DSSCs.

Two different approaches can be suitable to curb the charge recombination reaction (CRR): diminishing the concentration of either of the reactants or reducing the reaction rate constant of the process. The first approach can be implemented by increasing the electron mobility in the semiconductor, for instance by reducing the number of defects in the crystalline lattice, or by making the dye regeneration reaction faster. The reduction of defect states in the TiO_2 substrate has been intensively studied experimentally [29, 30] and chemical protocols have been devised to this end; however this would also impact on the manufacturing cost of the device. The dye regeneration reaction, on the other hand, is already the most energetically wasteful process in conventional DSSCs (because of the driving force needed) [167], therefore increasing the driving force to make this reaction faster

would further reduce the work extracted by the device (and moving the electrolyte level to higher energies, i.e. closer to the TiO_2 conduction band edge, could also make the CRR to electrolyte species more favourable as shown in chapter 5).

For these reasons, the most advantageous strategy to reduce the CRR is to make this process inherently slower by a suitable design of the electronic structure of the dye. For example, we have seen in the previous chapter how the orbital symmetry of the dye can be used to reduce the CRR by two to three orders of magnitude [194]. In this chapter we suggest an alternative approach to reduce the CRR, applicable when the dye is formed by a chromophore weakly coupled to a bridge that connects it to the semiconductor surface, and that can be adopted in synergy with the previous one.

In what follows we compute the CRR rate for dyes featuring a cross-conjugated bridge and compare it with the linearly conjugated counterpart, which is very common among DSSCs sensitisers [6]. A cross-conjugated molecule can be defined as a polyene chain made of sp^2 carbon atoms which features a branching point (see Figure 31). The carbon atom at the branching point will be connected to a substituent via a double bond and to two carbon atoms via formally single bonds. The latter two atoms are therefore not conjugated as they are separated by two consecutive single bonds. Two molecular fragments are connected by a cross conjugated bridge when two consecutive single bonds between sp^2 carbons are found along the chain that connects the two fragments. This type of bridge has been extensively studied in the field of electron transport and their prominent characteristic is the occurrence of an antiresonance feature in the electronic transmission, i.e. the transmission function through the bridge is negligible for incoming electrons in a well-defined energy window [205]. Furthermore, it has been shown how, by substituting the functional

group attached to the branching point, it is possible to modulate the transmission properties by shifting the energy range at which the antiresonance occurs [205]. A recent study by Thygesen and co-workers [191, 206] has related the presence of this antiresonance to the topology of the π system, and has established a simple graphical rule to predict the presence of this quantum interference feature in the transmission function.

This chapter is articulated as follows: the theory of bridge mediated charge recombination is briefly reconsidered in section 7.2 and it is then adapted to study the phenomenology of a simple model Hamiltonian in section 7.3. The results will then be generalised to the case of a realistic system, studied at the DFT level of theory.

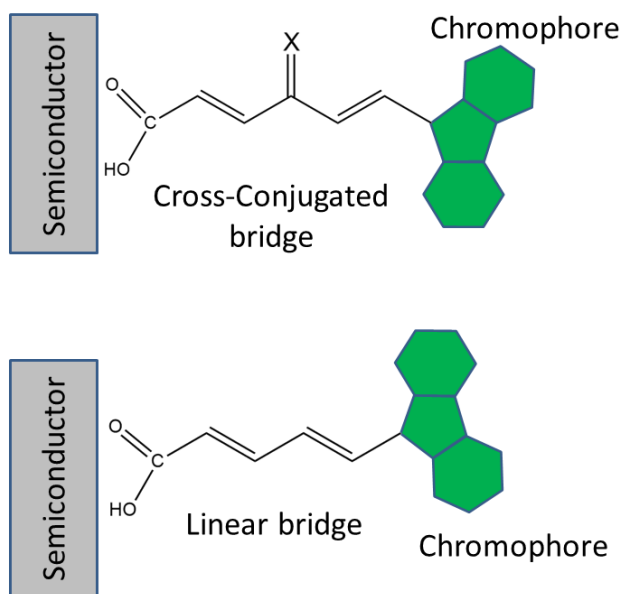


Figure 31. Sketches of dye molecules featuring a cross-conjugated bridge (top) and a linearly conjugated one (bottom).

7.2 Bridge mediated charge recombination

For convenience we report below the key equations introduced in chapter 2 that will then be adapted to the tight binding model introduced in section 7.3 for a cross conjugated bridge. If we consider a system that can be partitioned into semiconductor (S) bridge (B) and chromophore (M), then by labelling with s , b and m the states pertaining to each partition respectively, we can express the electronic Hamiltonian as:

$$H = H_S + H_B + H_M + V_{SB} + V_{BM} \quad (7.1)$$

$$H_S = \sum_{s \in S} \varepsilon_s |s\rangle\langle s|; \quad H_B = \sum_{b \in B} \varepsilon_b |b\rangle\langle b| + \sum_{b' \in B} \beta_{bb'} |b\rangle\langle b'|; \quad H_M = \varepsilon_m |m\rangle\langle m| \quad (7.2)$$

$$V_{SB} = \sum_{s,b} \tau_{sb} |s\rangle\langle b| + h.c.; \quad V_{BM} = \sum_{b \in B} \kappa_{bm} |b\rangle\langle m| + h.c. \quad (7.3)$$

where the semiconductor's Hamiltonian term has been expressed in a diagonal representation for convenience. We indicate with τ and κ respectively the coupling matrix elements between semiconductor and chromophore orbitals with states on the bridge, while β is the coupling term between different bridge states. This representation will prove convenient when the tight binding approximation is considered.

According to the derivation reported in chapter 2, the charge recombination rate can be expressed as the integral of the product of the Fermi-Dirac distribution (2.9), the Franck-Condon term, $F(\varepsilon_m - E)$ as expressed in (2.11) and the spectral density $\tilde{\Gamma}(E)$:

$$\tilde{\Gamma}(E) = \text{tr}\{\mathbf{\Gamma} \mathbf{g} \mathbf{K} \mathbf{g}^\dagger\} \quad (7.4)$$

where $\text{tr}\{\cdot\}$ is the trace operator over the bridge states acting on the matrices involved which are respectively: the coupling between the semiconductor and the bridge ($\mathbf{\Gamma}$, defined in equation (2.33)), the Green's function operator \mathbf{g} introduced in equation (2.28) (which is related to the tunnelling probability across the bridge moiety) and the coupling between the bridge and the chromophore unit (\mathbf{K}).

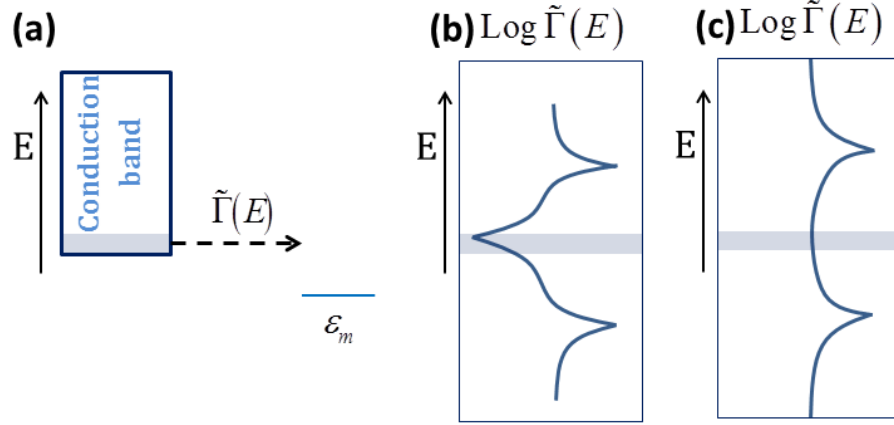


Figure 32. (a) Illustration of the energy levels for the electron transfer from the bottom of the conduction band of the semiconductor to the dye. A relatively narrow range of initial energies E is involved. The rate is controlled by the spectral density $\tilde{\Gamma}$ which depends on the nature of the bridge. Herein we design a bridge that contains an antiresonance (a minimum of $\tilde{\Gamma}$) in correspondence of the electron transfer energy, to minimize the rate of charge recombination. This is illustrated in (b), while the spectral density for a bridge without antiresonances is shown in (c).

The rate expression in equation (2.8) involves a summation over the energies of the incoming electrons present in the semiconductor. At each energy the charge recombination rate is determined by the by the population of the electronic states $f_\mu(E)$, the Franck-Condon term and the spectral density $\tilde{\Gamma}$ that collects the information on the electronic structure of semiconductor-dye interface and the

tunnelling probability across the bridge. For many realistic situations only a narrow range of energies (within few $k_B T$ above the conduction band edge) will give a contribution to the rate. To minimize the charge recombination rate (without affecting the charge injection) one should design a dye that has a minimum of $\tilde{\Gamma}(E)$ for energies close to the conduction band edge. In this respect cross-conjugated bridges can be successfully employed to modulate the charge recombination rate, thanks to their antiresonance feature mentioned in the introduction [192, 205, 207]. At the same time this property will not affect the charge injection mechanism since the injecting orbital is generally localised close to the interface and the energies involved are well above the semiconductor's conduction band edge [56]. The role of this antiresonance for charge recombination is shown in Figure 32. We will obtain these antiresonance features with a tight binding model of the bridge moiety for linear and cross-conjugated bridges. These results will be compared to those obtained from a DFT simulation of the TiO_2 -dye interface.

7.3 Charge recombination through tight binding linear and cross-conjugated bridges

We initially consider a tight binding bridge model to explore the phenomenology in a fully controllable system, before considering a realistic case. If we indicate with N the total number of bridge states, which coincides with the number of bridge sites as shown in Figure 33, and allow only the terminal sites to interact with the semiconductor and the light harvesting unit respectively then the bridge Hamiltonian and the coupling terms become:

$$H_B = \sum_{b=1}^N \alpha_b |b\rangle\langle b| + E_X |X\rangle\langle X| + \sum_{b=1}^{N-1} \beta (|b\rangle\langle b+1| + |N-2\rangle\langle X|) + h.c. \quad (7.5)$$

$$V_{SB} + V_{BM} = \tau |l\rangle\langle 1| + \kappa |N\rangle\langle m| + h.c.$$

where $|X\rangle$ indicates the substituent group connected to the bridge over the cross-conjugated bond and E_X is the corresponding site energy, α_b is the on-site energy parameter for the remaining bridge sites while β is the tunnelling matrix element from one site to the next, the substituent is attached to the bridge at the site $N-2$. We consider cross-conjugated bridges of length $N = 5, 7$.

We describe the linearly conjugated system by removing the terms containing the cross-conjugated state $|X\rangle$ from equation (7.5) and setting $N = 6, 8$.

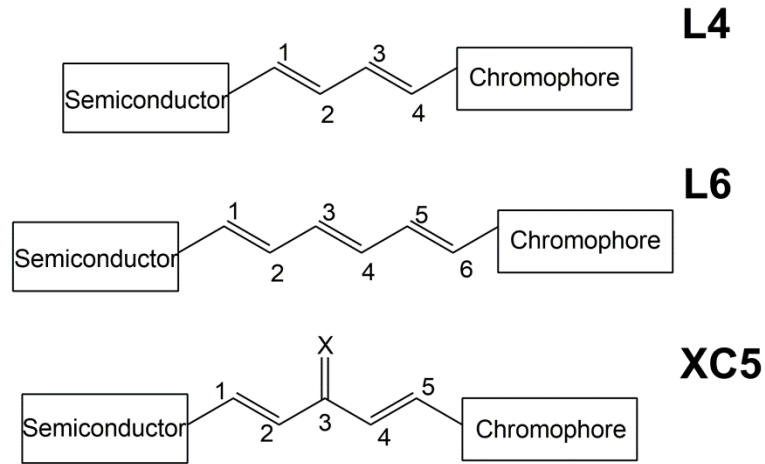


Figure 33. Sketches of the tight-binding systems considered.

If we assume a uniform distribution of semiconductor's states, ρ , above an energy threshold (which can be identified with the conduction band minimum), equation (7.4) can be simplified into [96]:

$$\tilde{\Gamma}(E) = \frac{2\pi}{\hbar} |\tau\kappa|^2 |G_{1,N}^0(E)|^2 \rho \quad (7.6)$$

where the only surviving element of the Green's operator is the one corresponding to the path connecting the first and the last bridge sites and because of the choice made for the density of semiconductor states the expression above will return a non-zero spectral density only for energies above the semiconductor's conduction band minimum. In deriving equation (7.6) we have exploited the same assumptions made in chapter 2, where the bridge Green's function for the interacting case had been replaced by the corresponding quantity for the non-interacting case on the basis of weak coupling between bridge and semiconductor, while the interaction with the chromophore does not affect the spectral density in the energy range of interest. In this way, since the Green's function will depend only on the bridge's Hamiltonian, equation (7.6) contains well factorised the properties of the bridge and of its coupling with the semiconductor and the rest of the dye molecule.

The Green's function is an analytic function in the complex plane with isolated singularities corresponding to the eigenvalues of the Hamiltonian operator; we will refer to these peaks in the Green's function as resonances. The presence of resonances is the only type of behaviour that the Green's function can show in a linear bridge as shown in Figure 34 for this simple example. On the other hand, for cross conjugated systems, the occurrence of destructive quantum interference is also possible for specific energies of the incoming electron. This feature manifests as a vanishing probability of electron tunnelling across the bridge fragment at certain energies, correspondingly the Green's function will have a zero at those energies, i.e. it will show an antiresonance.

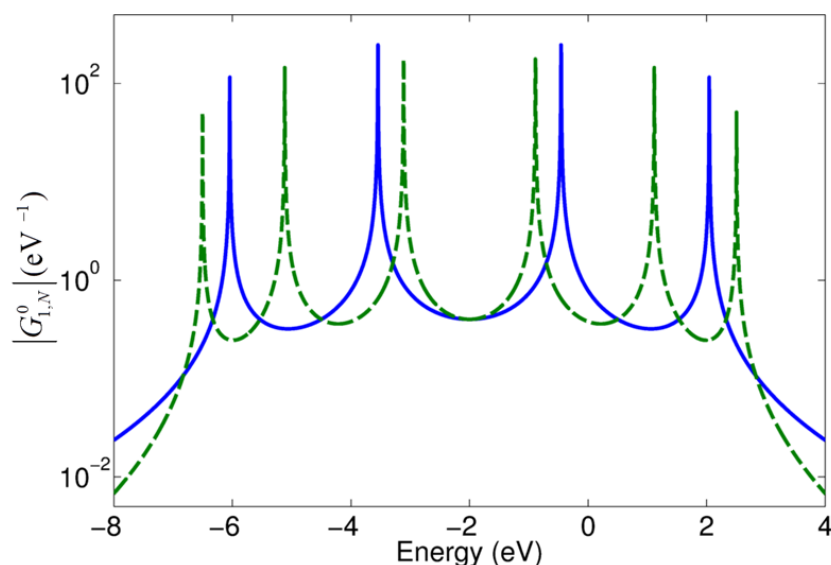


Figure 34. Green's function (in absolute value) for the linear tight-binding bridges L4 (solid line) and L6 (dashed line). Tight binding parameters are $\alpha_b = -2.0$ eV, $\beta = -2.5$ eV.

The occurrence of an antiresonance in the XC5 cross-conjugated bridge is shown in Figure 35, where the absolute value of the Green's function is reported in panel a) for an incoming electron entering the bridge through the first site and leaving through the last. The different Green's functions shown are obtained varying the on-site energy E_X of the cross-conjugated group substituent and, in correspondence of the energy value E_X , an antiresonance is observed. This feature is suppressed when the energy E_X is aligned with a resonance of the bridge (as for the case of $E_X = -4.5$ eV, red dashed line).

In a real molecule, however, the coupling with the semiconductor can have a more complex structure than that postulated in this tight binding model: for instance the coupling between the second bridge site and the semiconductor can be bigger than zero, giving a finite probability for the electron to enter the bridge through this site. In this case the Green's functions show a richer structure, as reported in Figure 35b.

The tunnelling probability for the incoming electron vanishes at two different energy values; one of the two antiresonance features (the one occurring at higher energies) can still be modulated by modifying the value of the site connected to the cross-conjugated chain. By progressively decreasing the value of E_X this antiresonance is shifted towards lower energies until it coalesces with the second antiresonance, which is not sensitive to the particular value of E_X employed. Based on this model we can therefore expect that (at least some) antiresonance features occurring in realistic systems might be tuneable by chemical means, i.e. by replacing the chemical substituent attached to the cross-conjugated branching point.

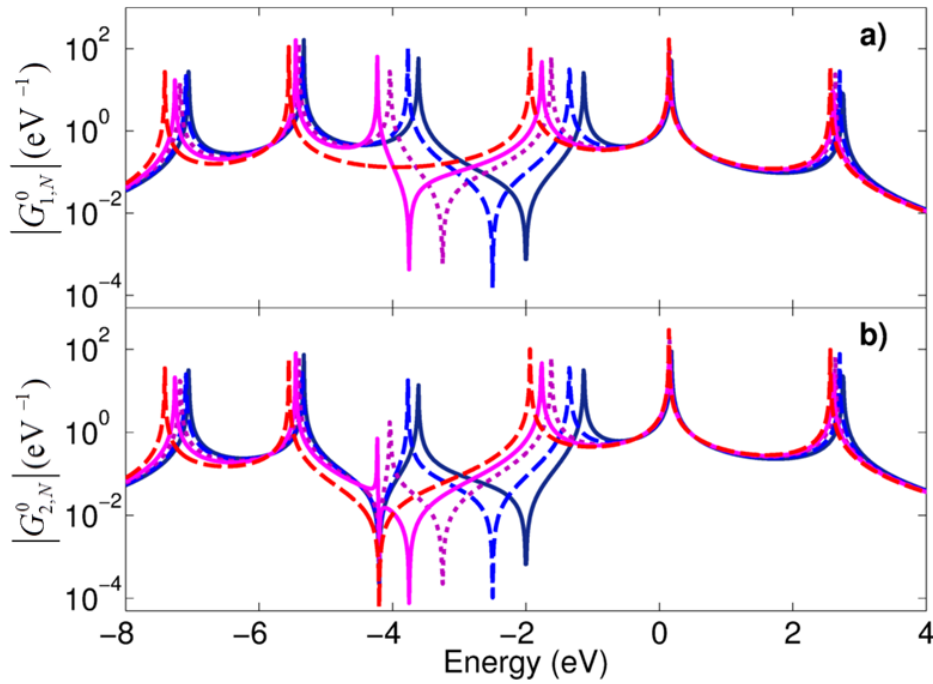


Figure 35. Green's functions for the XC5 bridge evaluated between the first and the terminal bridge sites (panel a) and between the second and the terminal site (panel b) for different values of E_X : -2.0 eV (solid blue), -2.5 eV (dashed blue), -3.25 eV (dotted purple), -3.75 eV (solid magenta) and -4.5 eV (dashed red). Tight binding parameters: $\alpha_b = -4.2$ eV for $b = 1$, $\alpha_b = -2.0$ eV otherwise, $\beta = -2.5$ eV

To assess the impact of the cross-conjugated geometry on the bridge-mediated recombination rate, the spectral density is computed by setting $\kappa = 0.25$ eV, $\tau = 0.1$ eV and $2\pi\rho \sim 1\text{eV}^{-1}$ in equation (7.6). The other tight binding parameters have been selected as specified in Figure 35, since this choice produces antiresonances near $E = -4.0$ eV, which is the lower energy threshold for the semiconductor's states. Other parameters required to evaluate the charge recombination lifetime are the reorganisation energy λ and the free energy variation ε_m , together with the quasi-Fermi level μ inside the semiconductor. These values have been chosen as $\lambda = 0.4$ eV, $\varepsilon_m = -5.0$ eV, and $\mu = -4.1$ eV, consistently with the values obtained from electronic structure calculations (specified in chapter 3) for the realistic dyes considered in section 7.4.

The charge recombination lifetime (computed as the reciprocal of the rate) is reported in Figure 36 as a function of the cross-conjugated on-site energy E_X for the bridge XC5 (solid line) and for the linear bridge L6 as a reference (dashed line). Results show that the recombination lifetime can be slowed down by four orders of magnitude, if the antiresonance feature in the $G_{l,N}^0$ function is aligned with the conduction band edge. This characteristic of cross-conjugated bridges is very encouraging and justifies further investigation at a higher level of theory to confirm the results obtained and ascertain if this property is shared by more realistic systems.

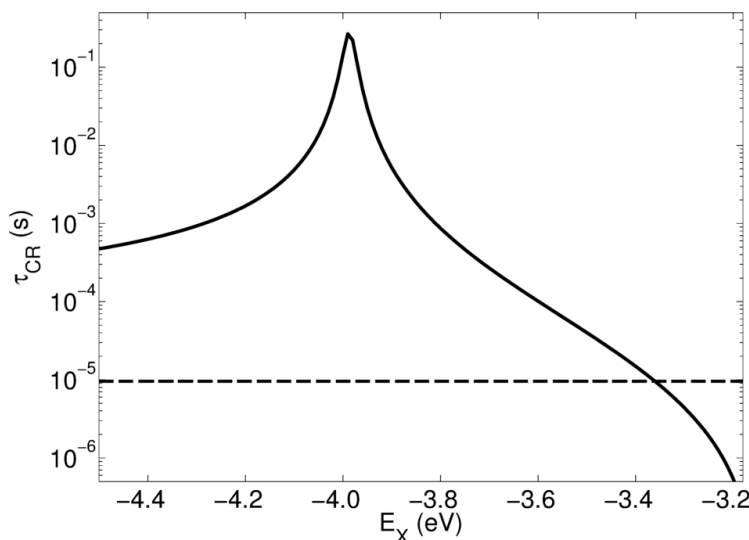


Figure 36. Charge recombination lifetime for the XC5 bridge as a function of the cross-conjugated group site energy. The value obtained for the linear bridge L6 is indicated by a dashed line.

7.4 Atomistic DFT simulation of the dye-TiO₂ interface and charge recombination evaluation

In this section we explore the possibility to design a realistic dye which, according to accurate DFT calculations, displays the same features identified in the tight binding model. We start by considering the case of linear bridges and we study the charge recombination as a function of the bridge length, then we will consider bridges with a cross-conjugated structure.

7.4.1 Linear Bridges

We consider the series of dyes reported in Figure 37 with bridges of different length. In these dyes the coupling between bridge and chromophore is particularly weak, as expected from the results reported in chapter 6 and in Ref. [194], hence, the partitioning method proposed above should be particularly suitable. The length of the bridge will allow us to disregard the direct coupling contribution between dye and semiconductor.

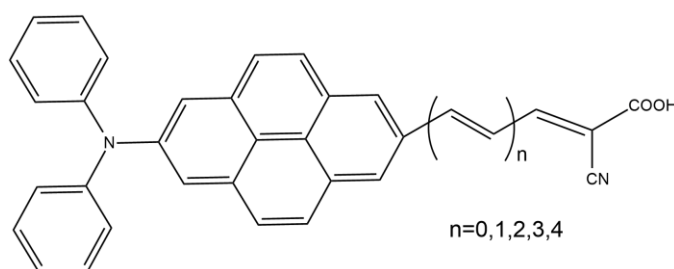


Figure 37. Chemical structure of the dyes considered

The electronic structure calculation for the evaluation of the spectral density in equation (7.4) proceeds in two steps: using the SIESTA code [118] we have simulated independently the isolated TiO_2 slab and the whole system semiconductor + dye. The anatase (101) surface was modelled using a 3×3 surface supercell containing 108 atoms and four atomic layers. Geometry relaxation was performed while keeping the coordinates of the bottom atomic layer fixed at the values of the bulk phase. The Brillouin zone was then sampled with a cutoff parameter for the grid in the reciprocal space of 30 \AA , the electronic structure was computed with a GGA-PBE exchange and correlation functional with double- ζ basis set and Troullier-Martins pseudopotentials. A similar geometry optimisation was also carried out in presence of formic acid in order to establish the adsorption geometry of the dye's anchoring group. The rest of the dye molecule was attached to the carboxylic group preserving the relative orientation, energy single point calculations were then performed at the same level of theory but including only the Γ -point on the slab + adsorbate system in order to obtain the matrix elements of the full Hamiltonian operator. This last calculation was performed at the Γ -point only because we are not

considering a periodic array of dyes interacting with each other, but rather only one dye adsorbed on a periodic semiconductors surface.

The semiconductor's Hamiltonian matrix H_S was obtained from the isolated slab calculation and it has been employed to evaluate the semiconductor's spectral density defined in chapter 2. The simulation of the semiconductor + dye system allowed us to extract from the total Hamiltonian matrix the semiconductor-bridge and the bridge-chromophore coupling matrix elements (indicated with τ and κ respectively in the previous section), together with the bridge's Hamiltonian matrix H_B . The use of a localised basis set makes it possible to partition the dye molecule (and its Hamiltonian) into the bridge and chromophore fragments as required by our theoretical scheme. The chromophore fragment has been identified as the aromatic core in Figure 37, including the diphenylamino substituent; the bridge has been defined as the polyene chain including the carboxylic anchor and the cyano group attached to it. The coefficients of the molecular orbital on the chromophore fragment, indicated by c_j^m in chapter 2, have been extracted from a similar single point energy calculation on the isolated dye.

In Figure 38 we report the spectral densities for the dyes in Figure 37; $\tilde{\Gamma}(E)$ is shown as a function of the independent energy variable introduced in the definition of the Green's operator. To improve the agreement between the position of the conduction band edge of the simulated system (in this case the isolated slab) with the values attained experimentally in a DSSC (reported in Ref. [136]) the semiconductor's states have been shifted upwards by 0.6 eV; the energy range relevant for the evaluation of the rate is highlighted in Figure 38 by a shaded marker.

A shift of this integration interval of 0.1 eV relative to the chosen energy scale does not change our conclusions. The spectral density is a complicated function of the bridge's electronic Hamiltonian (which also reflects the chemical connectivity between its atoms) and the coupling matrices with the other subsystems. The occurrence of peaks, as mentioned before, is related to bridge's eigenvalues, while the antiresonances are associated with signatures of quantum destructive interference. If a model system is studied, with the interaction restrained to the bridge's terminal sites, antiresonances do not appear, while if the electron is allowed to hop on bridge's orbitals other than the terminal one and then to propagate across the molecule destructive interference can be generated [208].

The position of the peaks in Figure 38 relates well with the bridge's eigenenergies: by changing the length of the bridge we are effectively modifying the energy spectrum of that subsystem, hence shifting the energies at which the peaks are located. Interestingly a sharp antiresonance appears close to the conduction band edge, which is not affected by changing the length of the bridge. The presence of this antiresonance is associated with the anchoring group used and with its coupling to the semiconductor (it disappears when the calculation is done on a hypothetical model molecule without anchoring group and coupled only through the terminal atom to the electrode). This is possibly an explanation for the success of the carboxylic acid anchoring group in dye sensitised solar cells, since having an antiresonance located in this energy range is going to slow down the charge recombination to the oxidised dye.

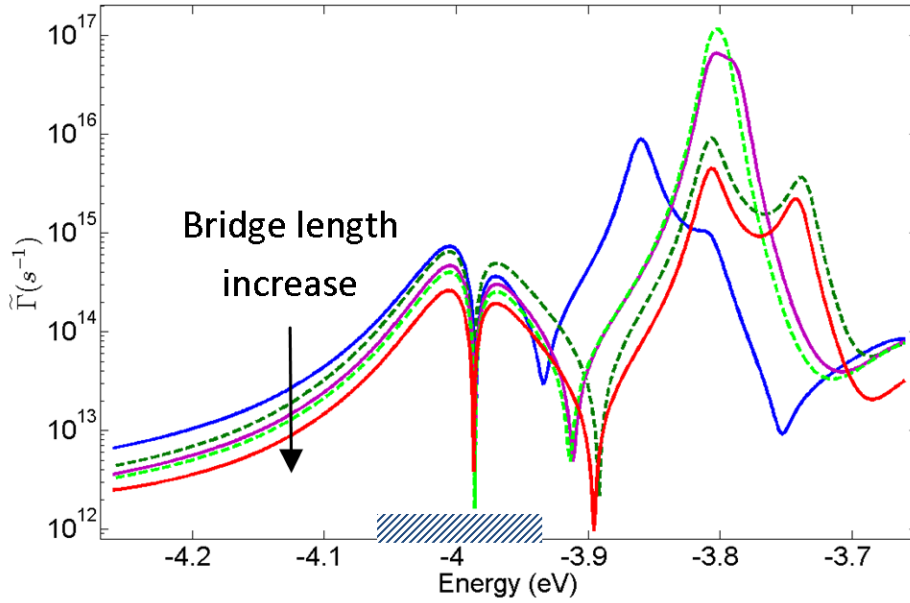


Figure 38. Spectral density for the dyes considered, the energy range that contributes most to the rate is highlighted assuming a sharp limit for the conduction band at -4.06 eV (shaded).

The values obtained for the charge recombination lifetime τ_{CR} are reported in Figure 39 using the same values of ε_m and λ employed in section 7.3, the quasi Fermi level has been set to 0.2 eV below the conduction band edge. Data show an exponential increase with the length of the bridge fragment, which is defined as the distance between the carbon atom of the anchoring group and that in the pyrene core linked to the bridge. If the data are fitted to the exponential $\tau_{CR} = \tau_0 \exp[\beta'R]$, where R is the bridge length, we obtain $\beta' = 0.1 \text{ \AA}^{-1}$ in complete agreement with the value reported for similar systems [198].

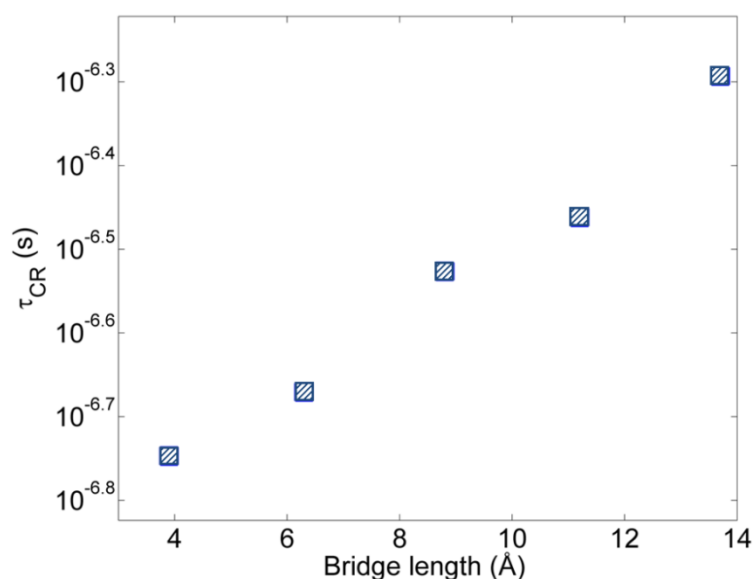


Figure 39. Charge recombination lifetime as a function of the bridge length.

The electron transfer processes taking place in DSSCs depend critically on the characteristics of the semiconductor surface: for instance the presence of trap states is known to speed up the charge recombination process, as we show in a phenomenological model of the interfacial electron transfer. Since the relative ranking of the spectral density does not change over a wide energy range below the conduction band edge, we can conclude that the role of the bridge will be unaffected by the presence of traps, with the charge recombination showing the same dependence on the bridge length, in agreement with previous experimental observations [165]. In order to slow down the charge recombination we test a different approach in which at the same time the HOMO of the dye is localized far from the interface with the semiconductor and the bridge mediated process is minimised. This will be achieved by introducing a cross-conjugated structure along the bridge moiety.

7.4.2 Cross-Conjugated Bridges

In this section we consider a cross-conjugated structure for the bridge moiety in the attempt to reproduce the increase in charge recombination lifetimes in the tight binding model. The chemical structures of the dyes considered are shown in Figure 40, with X indicating the substituent on the cross-conjugated chain.

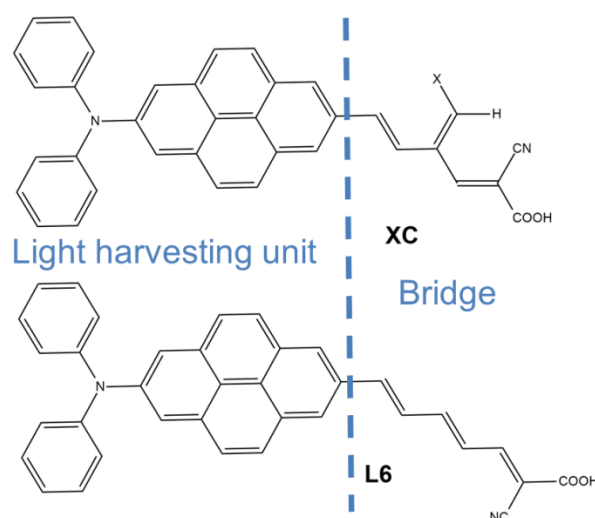


Figure 40. Chemical structures for the Pyrene derivatives employed in the DFT calculations. We set the cross-conjugated substituent X equal to: $-\text{NO}_2$, $-\text{CN}$, $-\text{COCl}$, $-\text{COMe}$, $-\text{CHO}$, $-\text{OH}$, $-\text{H}$ and $-\text{OMe}$.

The computational procedure followed for these molecules is identical to that reported in the previous section for linear bridges. The resulting $\tilde{\Gamma}$ is shown in Figure 41 for the cross-conjugated systems considered: again, the energy axis has been shifted upwards by 0.6 eV so that the calculated conduction band minimum E_C , estimated for the isolated slab, has been aligned to its typical experimental value (-4.0 eV) in a DSSC [136]; the energy range which affects the most the resulting recombination lifetime is highlighted by a dark marker, the lowest value in the highlighted region is the conduction band edge.

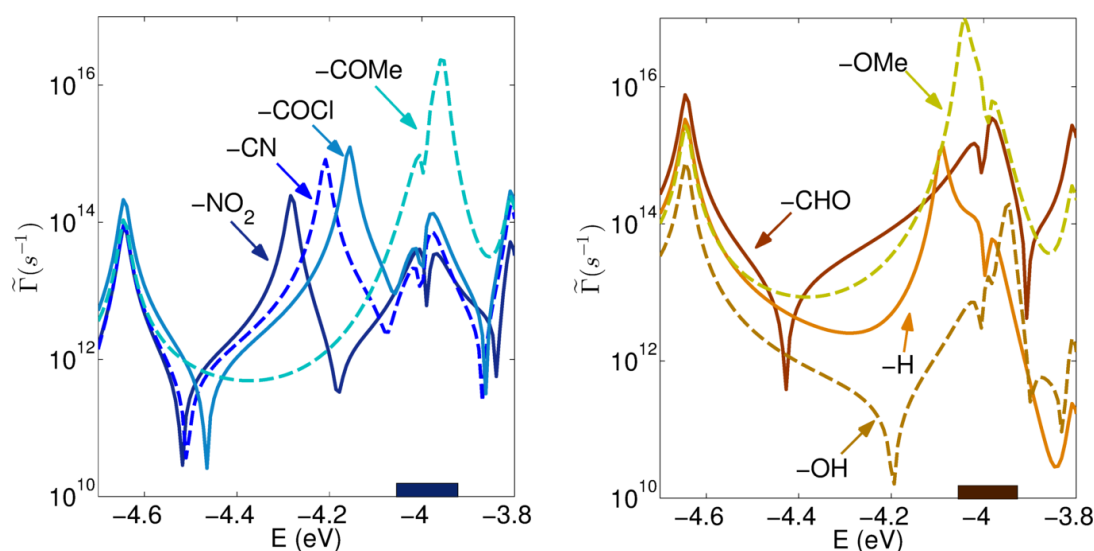


Figure 41. The bridge mediated semiconductor-dye coupling for electron withdrawing cross-conjugated groups (left panel) and for electron donating groups (right panel). The integration range is highlighted by a shaded area.

In agreement with what was found for the tight binding model, the position in energy of the antiresonance feature can be modulated by changing the substituent on the cross-conjugated group. In Figure 41 (left panel) the spectral density is reported for cross-conjugated bridges with electron-withdrawing substituents: the main feature of these bridges is the presence of a resonance peak that is progressively shifted towards higher energies by less electron-withdrawing substituents. This feature is also present in similar molecules whose transport properties were studied theoretically [205].

Proceeding along the series of substituents with those reported in the right panel of Figure 41, we notice how the antiresonance feature, originally located at -4.5 eV approx. is shifted towards higher energies. The case of the -OH substituted bridge is particularly interesting since it shows the occurrence of an antiresonance near the conduction band edge together with similar features at higher E ; as a result the

spectral density is significantly depressed in an energy range of 0.3 eV, more than the interval of few $k_B T$ relevant for the integral in equation (2.8).

In general, we can say that the calculation reveals the presence of antiresonances above and below the conduction band edge; some of these features are modulated by the energy of the side group, as predicted by the tight binding model analysed in section 7.3. Others, as already established in the case of linear bridges, are less intuitive and require a calculation of the full semiconductor-molecule interface.

The values of charge recombination lifetimes are reported in Figure 42 and have been obtained evaluating the rate over the conduction band energy range. From the data in Figure 42 we can see how the introduction of a cross-conjugated bridge can slow down the charge recombination reaction by a factor 30 in comparison with the linear bridge L6 (shown in Figure 40). The information provided by the DFT simulation of the interface is richer than the minimal tight binding model for the (π electron mediated) charge transfer, however some similarities exist. In particular, the profile observed for electron-donating groups (shown in the right panel of Figure 41) is in qualitative agreement with the behaviour for high values of the substituent on-site energy E_X . For these functional groups there is a progressive increase in charge recombination lifetime, starting from the most electron-donating group, until a maximum is reached, corresponding to the $-OH$ substituent. The reason for this slower charge recombination has been ascribed to the presence of two antiresonances close to the energy window of interest. As these antiresonances are moved away (for the aldehyde substituent) the lifetime τ_{CR} decreases again, as predicted by the tight binding model. For electron-withdrawing groups (whose spectral densities are shown

in the left panel of Figure 41) the suppression of the antiresonance first (for the –COMe group) and then the appearance of a feature showing an antiresonance near the conduction band minimum produces an increase in τ_{CR} that is not accounted for in the tight binding model.

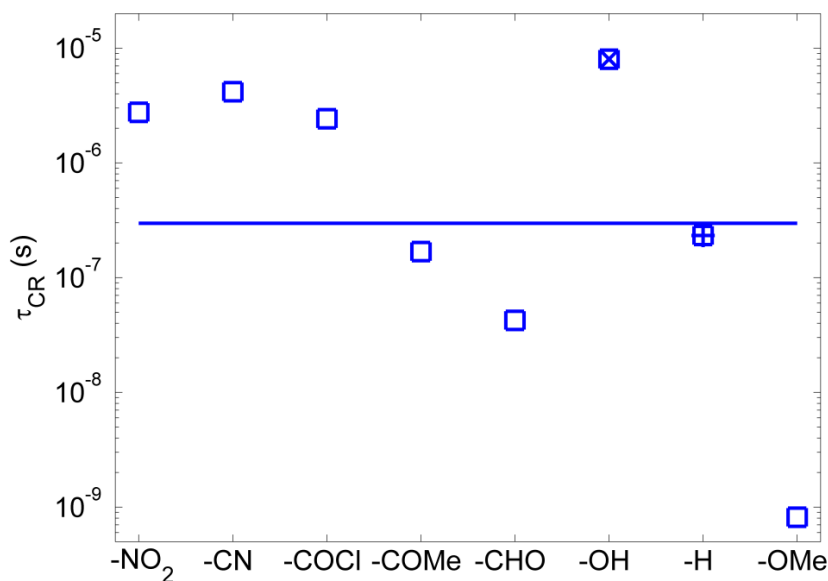


Figure 42. Charge recombination lifetimes for cross-conjugated molecules (with the lifetime for the linearly conjugated bridge L6 shown by a solid line), as a function of the chemical substituent.

Finally, we assess the robustness of the calculations on distortions of the dye's equilibrium geometry. We consider the dihedral angle (θ) between the cross conjugated group and the rest of the bridge moiety shown in Figure 43a. Previous research on electron transmission has shown the relevance of this structural parameter on the electronic properties of the bridge studied [207]. The ground state energy is evaluated as a function of θ leaving the remaining nuclear degrees of freedom at their equilibrium values. The energy difference with the equilibrium

conformation ($\theta = -1.8$ deg) is shown in panel (b) for the cross-conjugated bridge showing the slowest charge recombination lifetime ($X=OH$); this quantity is then evaluated over a range of θ values and reported in panel (c) together with τ_{CR} for the $-H$ substituted cross-conjugated bridge.

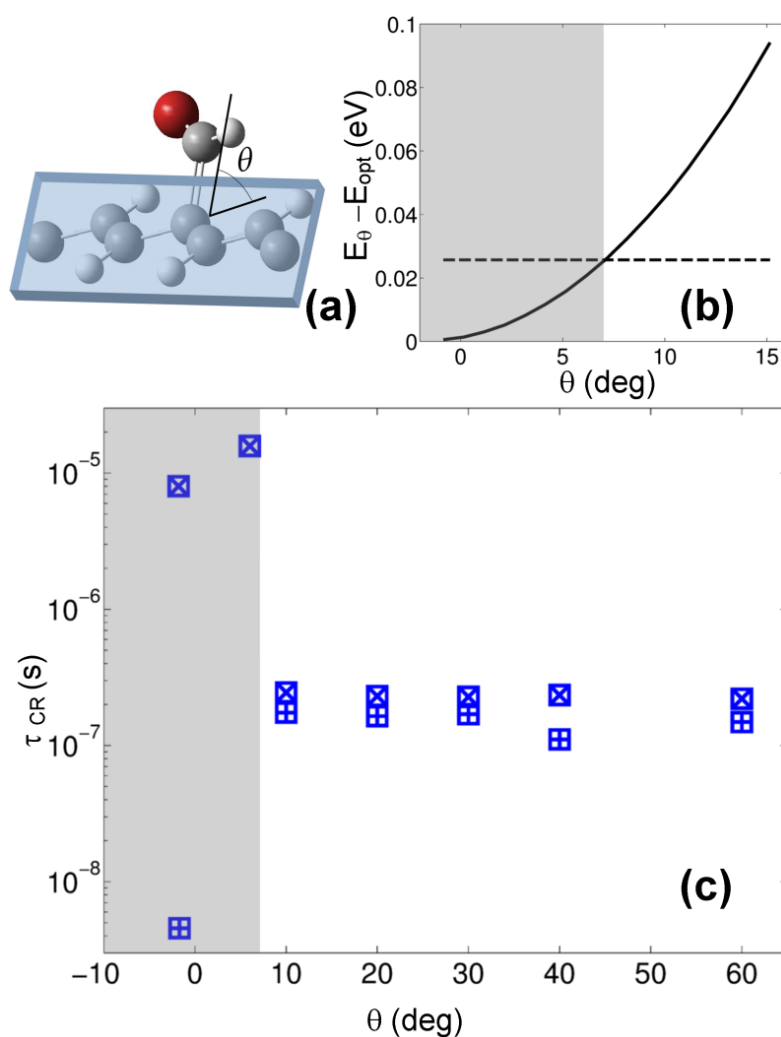


Figure 43. (a) Dihedral angle θ studied in the $-OH$ and $-H$ substituted bridges. (b) Energy scan for the $-OH$ substituted molecule as a function of the dihedral angle, the thermal energy ($T=298.15$ K) is marked by a dashed line. (c) Charge recombination lifetimes (τ_{CR}) for the $-OH$ ($-H$) substituted bridge are marked with 'x' ('+') symbols respectively; the shaded area highlights values for conformations accessible at room temperature.

Large distortions of the dihedral angle θ have a substantial impact on τ_{CR} : as shown in Figure 43c a variation of more than 10 degrees on the equilibrium value effectively ‘isolates’ the cross-conjugated group, giving an lifetime comparable with that obtained for a linearly conjugated bridge. However the bridge structure is rather rigid, as shown by the span of θ accessible by interaction with a thermal bath in panel (b); for values of θ in this range the rate is left unaffected.

7.5 Conclusions

In this chapter we have applied the theory of bridge mediated electron transfer theory in the attempt to impede the charge recombination reaction in dye sensitised solar cells. To this end we have selected chromophores that feature a cross-conjugated bridge connecting the semiconductor with the light harvesting unit. We show that this class of molecules can be useful for the design of innovative sensitisers, since it is possible to modify with chemical means the intrinsic lifetime for the main dissipative pathway in the photon to electron conversion mechanism.

The theory allows us to rationalise the dependence of the charge recombination lifetime on the chemical nature of the bridge substituent in terms of the more prominent resonance and antiresonance features that most affect the spectral density near the semiconductor’s conduction band edge. To help disentangle these features a minimal tight binding model has complemented the description of the bridge’s π electronic structure. Nuclear conformational effects have also been taken into account at the DFT level of theory; results are shown to be robust for distortions of the equilibrium conformation compatible with typical thermal energy values.

Chapter 8: Evaluation of the interfacial electrostatics effects through an effective one-body Schrödinger equation

8.1 Introduction

In this chapter we will test one of the underpinning assumptions we have made in the formulation of the expression for the charge recombination reaction rate, namely the weak-coupling regime between the adsorbate and the semiconductor substrate [209].

In this chapter we test the solidity of this argument by computing the spatial distribution of the photoinjected electron at the interface of two dielectric continua; the electron interacts with a positive charge at fixed distance from the interface between the two media (each characterised by its dielectric constant). The set of a localised electron in the semiconductor and a positive charge in the electrolyte solution is referred to as a charge transfer exciton and it has been discussed in the literature on DSSCs [113, 210, 211].

Besides the theoretical relevance of this investigation, this chapter is also relevant for the characterisation of the trap states postulated by the most widespread model of the electron diffusion in dye sensitised solar cells, the ‘multiple-trapping model’ already mentioned in chapter 1. In this model an exponential distribution of trap states is postulated and the experimental interval for its average energy is between 0.09 eV and 0.14 eV below the CBm. Different hypothesis have been put forward concerning the microscopic origin of these shallow trap states: from the presence of surface states [17], to the dependence on the material morphology [212]. The role of grain boundaries is also acknowledged, especially in ZnO based architectures, where

significant differences in electron diffusion have been measured between nanoparticles and nanorods [213]. However, for the more common TiO_2 based DSSCs, the role of grain boundaries seems to be marginal, with the experiment failing to highlight differences between nanowires and nanoparticles based electrodes [9, 214]. Some experimental report has hinted at the presence of these shallow trap states as not an intrinsic property of TiO_2 nanoparticles but rather associated with electron-ion interactions [215]. To the best of our knowledge this issue has not been addressed theoretically thus far, and the model proposed in this chapter is well suited to this purpose. In particular we will see that the ground state energy for the charge transfer exciton relates well with the typical energy position of the trap states for a reasonable choice of the physical parameters introduced in the model.

The one-body Schrödinger equation for the charge transfer exciton is reported in the next section and, after briefly discussing the choice of parameters entering in it, it is solved employing the variational method. For convenience, some of the more formal derivations are placed in appendixes of this chapter after the result section (8.3): the interaction potential for point-like particles with the method of the image charges is derived in section 8.5 and the Hamiltonian matrix elements are given in section 8.6.

8.2 Description of the model

In what follows we introduce an effective one body Hamiltonian for the injected electron in the semiconductor's conduction band. To allow for the interaction between the electron and its surroundings we adopt a continuum dielectric description of the TiO_2 nanoparticle. Clearly, for the formalism to be consistent, the

electronic wavefunction, solution to the stationary Schrödinger equation, is required to be delocalised over a large spatial region in comparison to the crystal unit cell, as also required by the effective mass approximation employed. Then, we can assume that the electrostatic interaction could be described in terms of the dielectric constant of the two media near the interface. Furthermore, the presence of an interface between the nanocrystal and the electrolyte can be introduced exploiting the image charge formalism [216–218].

The effective one body Hamiltonian in cylindrical coordinates $\mathbf{r}=(\rho, \varphi, z)$ reads:

$$\hat{H} = -\frac{\hbar^2}{2\mu} \nabla^2 - \frac{\beta e^2}{16\pi\epsilon_0\epsilon_2 z} - \frac{\gamma e^2}{4\pi\epsilon_0 \sqrt{\rho^2 + (z + z_h)^2}} \quad (8.1)$$

where the Laplacian operator in cylindrical coordinates is given explicitly in equation (8.20) and the constants introduced are the Plank's constant \hbar , the electron effective mass μ , the elementary charge e , the vacuum permittivity ϵ_0 , the macroscopic dielectric constant for the two media respectively ϵ_1 (for the electrolyte solution) and ϵ_2 (for the semiconductor). The positive charge embedded in the first medium, has been positioned at $(0, 0, -z_h)$ as shown in Figure 44b. The potential term in the Hamiltonian above comprises of two contributions, each of them with a distinctive symmetry. The first term is due to the image charge generated by the electron at the interface and depends on the coordinate on the z -axis orthogonal to the surface of the semiconductor, while the last term takes into account the Coulomb contribution arising from the point charge and it is spherically symmetrical. The constants β and γ

are introduced in the appendix 8.5 and have been defined as: $\beta = (\varepsilon_2 - \varepsilon_1)/(\varepsilon_2 + \varepsilon_1)$ and $\gamma = 2/(\varepsilon_2 + \varepsilon_1)$.

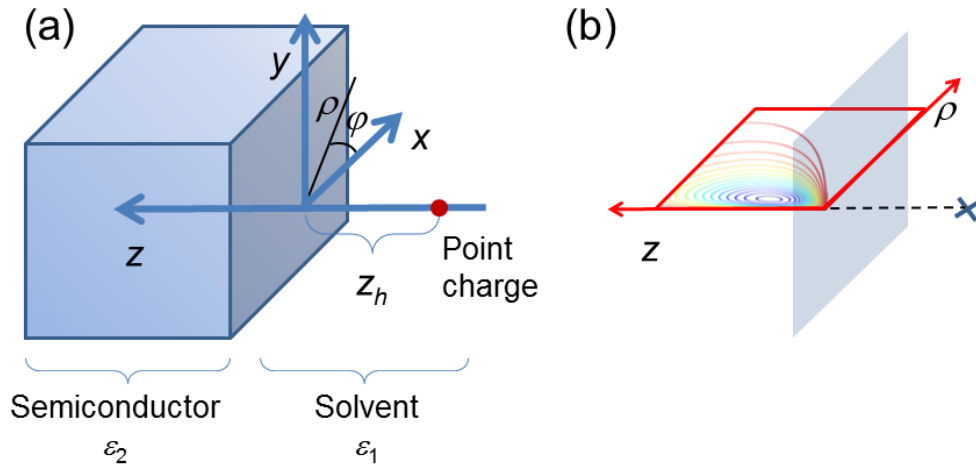


Figure 44. (a) Sketch of the model system and cylindrical coordinate system employed. (b) Section plane (highlighted in red) in which the electronic wavefunction will be evaluated. The plane is orthogonal to the interface between the two media (in grey) and contains the point-like charge. Illustrative contour plot for the electron wavefunction is also shown in the section plane.

The potential operator is isotropic (i.e. it does not depend on the coordinate φ), hence the angular term in the Laplacian can be factorised. The eigenfunctions of the operator $\hat{l}_z = -i\hbar \frac{\partial}{\partial \varphi}$ will then factorise the overall solution, leading to a dependence on the angular quantum number m . We will label the solutions obtained for different values of m following the practice for systems with spherical symmetry: $m = 0 \rightarrow s$, $m = \pm 1 \rightarrow p$ and so on. Owing to the presence of the Coulomb term it is not possible to solve analytically the Schrödinger equation in the remaining coordinates (ρ, z) , hence an approximate solution has to be sought. To do so we resort to the linear variation technique; the eigenstates of the system will be approximated by a linear

combination of basis functions. A suitable, orthonormal basis set for the radial coordinate is given by the Landau states [218, 219]:

$$R_l^{|m|}(\xi) = \sqrt{\sigma} \sqrt{\frac{l!}{(l+|m|)!}} e^{-\frac{\xi}{2}} \xi^{\frac{|m|}{2}} L_l^{|m|}(\xi) \quad (8.2)$$

where with $L_l^{|m|}(\xi)$ we have indicated the generalised Laguerre polynomials defined as a function of the scaled variable $\xi = \frac{\sigma}{2} \rho^2$, of the principal quantum number $l = 0, 1, 2, \dots$ and of the angular quantum number $m = 0, \pm 1, \pm 2, \dots$. For the z coordinate we employ the eigenfunctions of the particle in a box:

$$\Lambda_v(z) = \sqrt{\frac{2}{L}} \sin\left(\frac{v\pi}{L} z\right) \quad (8.3)$$

with L we indicate one endpoint of the domain $[0, L]$ on which the basis set is defined; this definition of the domain is consistent with the constraint $z > 0$ we assumed on a physical basis. The quantum number v takes non-negative integer values. We refer to the end of chapter appendix for the explicit evaluation of the Hamiltonian matrix elements. By diagonalisation of the Hamiltonian matrix we obtain the energy spectrum and the coefficients of the linear combination to express the variational wavefunction in terms of the basis set elements:

$$\Psi(\xi, z) = \sum_{l,v} C_{l,v} R_l^{|m|}(\xi) \Lambda_v(z). \text{ The expression for the Hamiltonian matrix elements}$$

is reported in section 8.6. The algorithm for the evaluation of these matrix elements has been implemented in Fortran90 with double precision arithmetic and the variational parameters $C_{l,v}$ are obtained as elements of the eigenvector matrix

obtained diagonalising the Hamiltonian matrix. The non-linear variational parameters L and σ have been obtained through minimisation of the ground state energy [220]; this has been achieved with a BFGS search algorithm [221].

To completely specify the model few other quantities are required, these are the dielectric constants for the two media and the effective electron mass. The value previously used in chapter 5 for the effective electron mass $\mu = 1.22 m_e$ measured for TiO_2 -anatase nanoparticles in reference [178] will be employed here as well; for the same quantity Kormann *et al.* [222] have proposed a value between $5 m_e$ and $13 m_e$ and we will consider the impact on the electron localisation for values of the effective mass in this range in the result section. The dielectric constant in nanocrystalline TiO_2 films has been estimated as $\epsilon_2 = 12 \pm 4$ (in units of vacuum permittivity) in ref [223], while the dielectric constant for bulk acetonitrile is 36.6 [224]. The presence of a solid interface, however, is known to affect the value of the dielectric constant for electrolytic solutions and it can be determined by solving the Poisson-Boltzmann equation for a given solute concentration. We will not pursue this approach here as it is not congruous with our theoretical framework and it would not be conclusive for the model presented as there are uncertainties on other parameters; we therefore assume that the behaviour shown by aqueous solutions in Ref. [225] can be extended to the case of acetonitrile and take the value of ϵ_1 to be one tenth of the value in bulk, i.e. $\epsilon_1 = 3.66$. This approach is consistent with the aim of this chapter which is to provide a conservative estimate of the exciton radius. Indeed, for big values of ϵ_1 the electron is more delocalised as the image charge

interaction that binds it to the interface becomes repulsive for $\varepsilon_1 > \varepsilon_2$ and the attractive Coulomb term in (8.1) is screened by the prefactor γ .

8.3 Results

We start by considering for illustrative purposes the variational solutions to the Hamiltonian in equation (8.1) for the case of a high value for the semiconductor's dielectric constant. In Figure 45 we report the three dimensional representation of the first five states at lower energy, obtained for $\varepsilon_1 = 1$, $\varepsilon_2 = 32$, $\mu = 1.22 m_e$ and with a positive charge located at 5 Å from the interface. The Cartesian axis orientation shown in figure matches the one showed in Figure 44, with the interface lying in the xy plane.

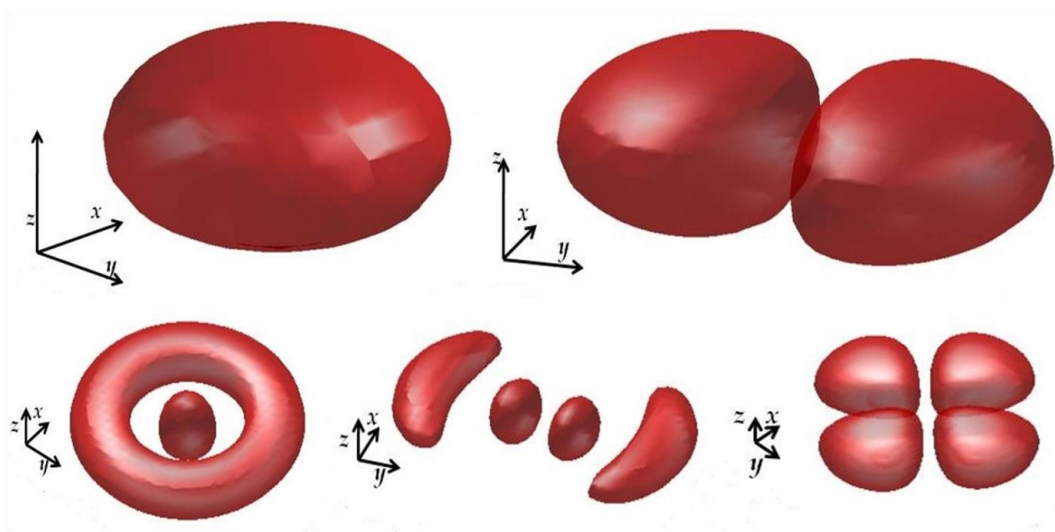


Figure 45. Real space representation for the electron density for the orbitals 1s, 1p, 2s, 2p, 1d, shown in order of increasing energy from top-left to bottom right.

The showcase presented is not meant to be representative of a strongly localised exciton: the interaction with the positive charge has a far stronger impact on the

wavefunction for the states shown in Figure 46, where we report the contour plot for a section of the wavefunction in the plane $\varphi = 0$ (shown in red in Figure 44b). These are obtained for a value of electron effective mass $\mu = 10 m_e$, while the dielectric constants are chosen to match the values introduced in the previous section: $\varepsilon_1 = 3.66$, $\varepsilon_2 = 12$; the positive charge has been positioned at 2.4 \AA from the interface, this value is compatible with the adsorption distance of an alkaline metal ion on the anatase (101) surface.

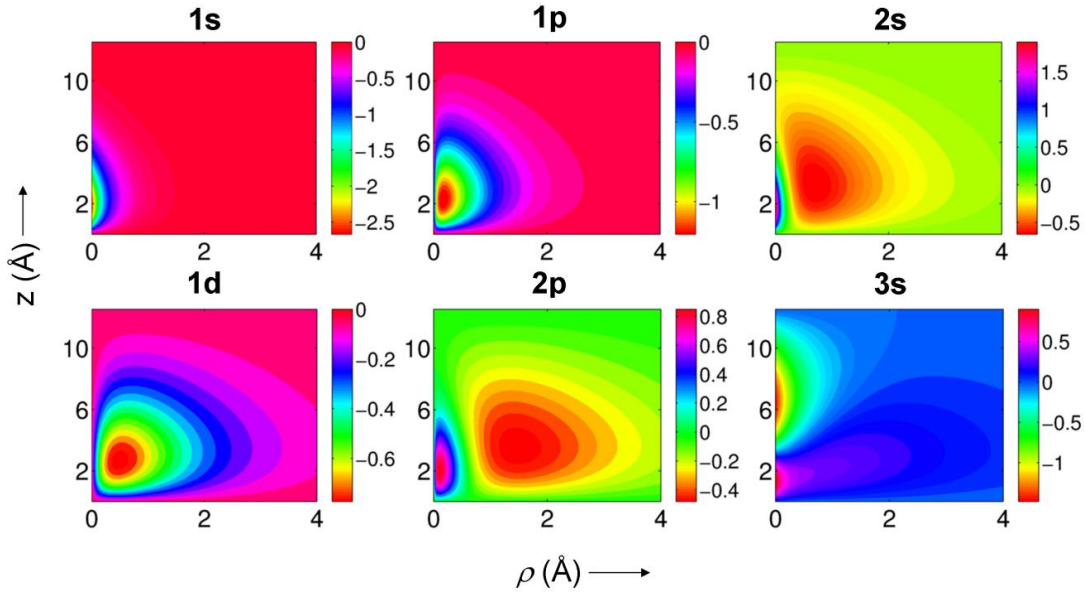


Figure 46. Contour plot for the electronic wavefunction, their respective energies are $E(1s) = -0.27 \text{ eV}$, $E(1p) = -0.19 \text{ eV}$, $E(2s) = -0.16 \text{ eV}$, $E(1d) = -0.15 \text{ eV}$, $E(2p) = -0.13 \text{ eV}$, $E(3s) = -0.13 \text{ eV}$.

The impact of the effective electron mass and of the semiconductor's dielectric constant, i.e. the two parameters affected by bigger experimental uncertainties, on the exciton ground state energy is analysed in Figure 47. The average value for the exponential trap distribution has been identified experimentally within -0.09 eV and

-0.14 eV (with the energy zero being the TiO_2 conduction band edge) and it is marked in Figure 47 by dashed lines. Interestingly, different intervals of ε_2 are compatible with the observed shallow trap energy for different values of the effective mass, in particular for $\mu = 1.22 m_e$ the permissible range for ε_2 overlaps with the experimental estimate of 12 ± 4 given in Ref. [223].

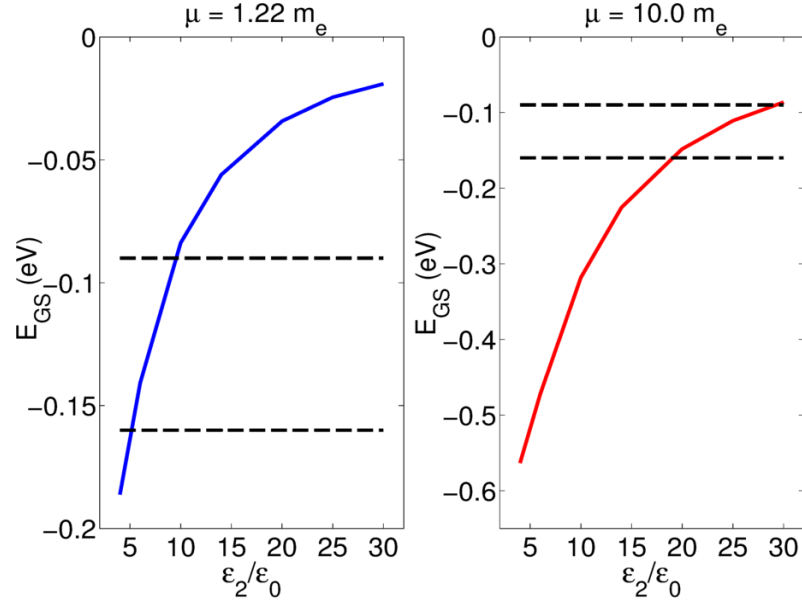


Figure 47. Ground state energy for the exciton obtained for $z_h = 2.43$ Å and $\varepsilon_1 = 3.66$ as a function of the other model parameters. Dashed lines represent the average value for the exponentially distributed trap states reported in chapter 5.

For heavier values of the electron mass that also have been reported [226] (shown in the right panel of Figure 47) the ground state is far lower in energy and for values of ε_2 near 10 gives a trap state positioned ~ 0.3 eV below the conduction band edge. Albeit ‘deep’ trap states (with trapping energies around 0.5 eV) have also been identified in working DSSCs, there is widespread consensus in identifying them with oxygen vacancies in the crystalline lattice [172, 173, 227]. Hence we exclude these states from the analysis of the electron localisation as the presence of isolated lattice

defects is clearly beyond the capabilities of the model presented here; the role of isolated point-like defects has been presented in chapter 5.

We now evaluate the exciton localisation for the two values of μ considered keeping ε_2 in the permissible physical range. To better quantify the localisation of the electron we define the exciton radius as the expectation value of the cubic root of the ‘volume’ operator $\hat{\rho}^2 \hat{z}$:

$$R = \langle \Psi_{1s} | \sqrt[3]{\hat{\rho}^2 \hat{z}} | \Psi_{1s} \rangle \quad (8.4)$$

where the subscript 1s identifies the ground state wavefunction; the values of R are reported in Table 5. In both cases considered the exciton radius is far bigger than the elementary cell of TiO_2 anatase, hence justifying the effective mass approximation made in this chapter and the small coupling regime postulated in chapter 2.

Table 5. Exciton radius for selected values of the semiconductor dielectric constant and electron effective mass. $z_h = 2.4 \text{ \AA}$ and $\varepsilon_1 = 3.66$

$\mu = 1.22 m_e$		$\mu = 10.0 m_e$	
ε_2	$R (\text{\AA})$	ε_2	$R (\text{\AA})$
6	174.8	20	47.85
10	218.2	25	41.94
14	513.0	30	41.92

8.4 Conclusions

In this chapter we have presented a model for the photoinjected electron in the semiconductor’s conduction band interacting with a positive charge at fixed distance from the semiconductor surface. The model is able to predict, for a reasonable choice

of the system's parameters, the binding energy observed experimentally for shallow trap states in DSSCs, hence supporting an experimental conjecture [215] that cannot be addressed directly because of the lack of direct *in situ* measurements of the surface charge under working conditions [167]. The electron localisation has been evaluated for these physically justified values of the parameters and the value of the exciton radius is comparable with the diameter of the TiO_2 nanoparticles used to assemble the photoelectrode. An important assumption made concerns the value of the dielectric constant of the solvent which has been estimated heuristically. A detailed description of the charge distribution on both sides of the interface is required to evaluate this quantity rigorously, which might be challenging from a theoretical standpoint.

In this model we have selected the parameters in order to evaluate the strongest possible excitonic binding energy. Under many circumstances, such as for ϵ_1 values comparable with its solution bulk value or for oxidised dyes of bigger size (with a positive charge density located further from the interface), the exciton binding energy can become smaller than the thermal energy and the existence of these states can be neglected when describing the initial state of the charge recombination process.

A limitation of the model presented lies in the minimal description of the molecular system adsorbed on the semiconductor's surface. This limitation restricts the applicability of the model, in particular since recent experimental studies have shown that depending on the molecular species adsorbed the charge transfer exciton was localised near the interface or delocalised over the whole nanoparticle [228].

This type of effects cannot be described by the model presented in this chapter; however the more general formalism given in chapter 2 should be able to include the impact of different adsorbates on the charge recombination kinetics, thanks to the explicit account of the semiconductor-molecule coupling.

8.5 Appendix: Evaluation of the potential energy using the image charge method

In this appendix we derive an expression for the electrostatic potential generated by a point-like charge in the proximity of a dielectric medium. In Figure 48 we can see how the plane $z = 0$ separates the two media, each characterised by the relative dielectric constant, hence we can write Gauss's law for each spatial region:

$$\begin{aligned}\epsilon_1 \vec{\nabla} \cdot \vec{E} &= 4\pi\rho_e & \text{for } z > 0 \\ \epsilon_2 \vec{\nabla} \cdot \vec{E} &= 0 & \text{for } z < 0\end{aligned}\tag{8.5}$$

where $\vec{E}(x, y, z)$ represents the electric field and the second equation follows from the fact that in region 2 we have no charges. Since there are no magnetic fields in our problem Faraday's law should be taken into account as $\vec{\nabla} \times \vec{E} = \vec{0}$.

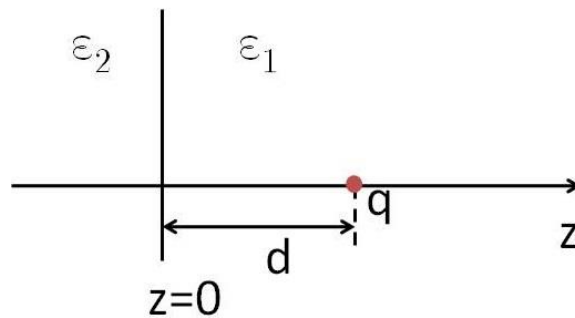


Figure 48. Sketch of the interface between the two media and position of the charge q relative to it.

The requirement of continuity for the fields at the interface leads to the equations:

$$\lim_{z \rightarrow 0^+} \epsilon_1 E_z = \lim_{z \rightarrow 0^-} \epsilon_2 E_z \quad (8.6)$$

$$\lim_{z \rightarrow 0^+} E_i = \lim_{z \rightarrow 0^-} E_i \quad i = x, y \quad (8.7)$$

Furthermore, since the electric field is irrotational then we can restate the problem in terms of the potential field φ : $\vec{E} = -\vec{\nabla} \varphi$.

Now we are going to apply the image potential method. To determine the field in the first medium let us introduce the fictitious charge q' as shown in Figure 49. The potential then reads as the sum of two contributions:

$$\varphi_1 = \frac{1}{4\pi\epsilon_0\epsilon_1} \left(\frac{q}{\sqrt{x^2 + y^2 + (z-d)^2}} + \frac{q'}{\sqrt{x^2 + y^2 + (z+d)^2}} \right) \quad (8.8)$$

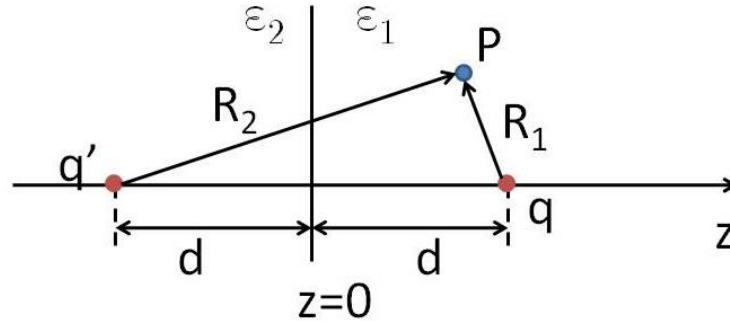


Figure 49. Image charge method to determine the field at point P

To specify anything more about q' we have to consider the second region. Here the potential satisfies the Laplace equation $\nabla^2 \varphi = 0$. In Figure 50 we show the charge distribution generating the potential, which can be expressed in the form:

$$\varphi_2 = \frac{1}{4\pi\epsilon_0\epsilon_2} \frac{q''}{\sqrt{x^2 + y^2 + (z-d)^2}} \quad (8.9)$$

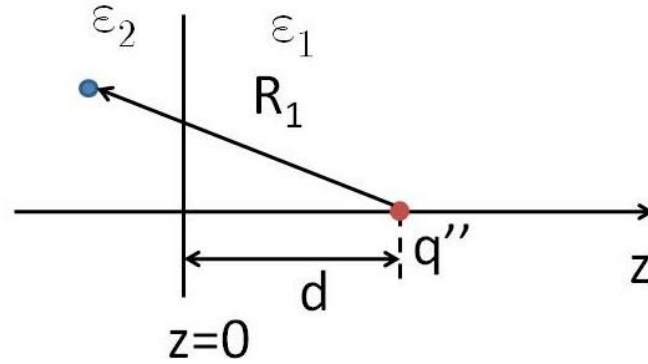


Figure 50. Charge distribution generating φ_2 .

Now let's consider the continuity equation (8.6). To do so we evaluate the partial derivative with respect to z and introduce the notation $\rho^2 = x^2 + y^2$

$$\begin{aligned} \frac{\partial \varphi_1}{\partial z} &= -\frac{1}{4\pi\epsilon_0\epsilon_1} \left[\frac{1}{2} \frac{2q(z-d)}{(\rho^2 + (z-d)^2)^{\frac{3}{2}}} + \frac{1}{2} \frac{2q'(z+d)}{(\rho^2 + (z+d)^2)^{\frac{3}{2}}} \right] \Rightarrow \\ \Rightarrow \frac{\partial \varphi_1}{\partial z} \Big|_{z=0} &= -\frac{1}{4\pi\epsilon_0\epsilon_1} \left[\frac{d}{(\rho^2 + d^2)^{\frac{3}{2}}} (q' - q) \right] \end{aligned} \quad (8.10)$$

Similarly:

$$\begin{aligned} \frac{\partial \varphi_2}{\partial z} &= -\frac{1}{4\pi\epsilon_0\epsilon_2} \left[\frac{1}{2} \frac{2q''(z-d)}{(\rho^2 + (z-d)^2)^{\frac{3}{2}}} \right] \Rightarrow \\ \Rightarrow \frac{\partial \varphi_2}{\partial z} \Big|_{z=0} &= -\frac{1}{4\pi\epsilon_0\epsilon_2} \left[\frac{d}{(\rho^2 + d^2)^{\frac{3}{2}}} (-q'') \right] \end{aligned} \quad (8.11)$$

Then the condition $\varepsilon_1 \frac{\partial \phi_1}{\partial z} = \varepsilon_2 \frac{\partial \phi_2}{\partial z}$ at the interface implies $q - q' = q''$. To recover another relation between the unknown charges we use the other continuity requirement:

$$\begin{aligned} \frac{\partial \phi_1}{\partial \rho} &= -\frac{1}{4\pi\varepsilon_0\varepsilon_1} \left[\frac{1}{2} \frac{2q\rho}{(\rho^2 + (z-d)^2)^{\frac{3}{2}}} + \frac{1}{2} \frac{2q'\rho}{(\rho^2 + (z+d)^2)^{\frac{3}{2}}} \right] \Rightarrow \\ \Rightarrow \frac{\partial \phi_1}{\partial \rho} \Big|_{z=0} &= -\frac{1}{4\pi\varepsilon_0\varepsilon_1} \left[\frac{\rho}{(\rho^2 + d^2)^{\frac{3}{2}}} (q + q') \right] \end{aligned} \quad (8.12)$$

And for the second region:

$$\begin{aligned} \frac{\partial \phi_2}{\partial \rho} &= -\frac{1}{4\pi\varepsilon_0\varepsilon_2} \left[\frac{1}{2} \frac{2q''\rho}{(\rho^2 + (z-d)^2)^{\frac{3}{2}}} \right] \Rightarrow \\ \Rightarrow \frac{\partial \phi_2}{\partial \rho} \Big|_{z=0} &= -\frac{1}{4\pi\varepsilon_0\varepsilon_2} \left[\frac{\rho}{(\rho^2 + (z-d)^2)^{\frac{3}{2}}} q'' \right] \end{aligned} \quad (8.13)$$

Hence we obtain a second relation between the charges. The system of linear equations to solve is:

$$\begin{cases} q - q' = q'' \\ \frac{1}{\varepsilon_1} (q + q') = \frac{1}{\varepsilon_2} q'' \end{cases} \quad (8.14)$$

Then we get $q' = q'' \left(\frac{\varepsilon_1 - \varepsilon_2}{2\varepsilon_2} \right)$ and $q = q'' \left(\frac{\varepsilon_1 + \varepsilon_2}{2\varepsilon_2} \right)$. If we now allow for the

original charge q to take value Ze , where e is the elementary charge, and hence test the electric potential with a charge $-e$ then the potential energy takes form:

$$V_2 = -\frac{Ze^2}{4\pi\epsilon_0\epsilon_2} \left(\frac{2\epsilon_2}{\epsilon_1 + \epsilon_2} \right) \frac{1}{\sqrt{\rho^2 + (z-d)^2}} = -\frac{Ze^2}{4\pi\epsilon_0} \frac{\gamma}{\sqrt{\rho^2 + (z-d)^2}} \quad (8.15)$$

where γ has been defined as $\gamma = \frac{2}{\epsilon_1 + \epsilon_2}$. This term of the potential is in agreement with the expression obtained by Zhu et al [229], although the overall expression (i.e. including the image potential term) is different. The minus sign in the denominator of equation (8.15) is due to the particular choice of the coordinate axis orientation. Making the substitution $z \rightarrow -z'$ we can take $(-1)^2$ out of the brackets, hence leaving a plus sign inside and $d > 0$, consistently with the axis orientation in Figure 44 and the sign convention in equation (8.1).

The potential generated in the first medium can be easily inferred from equation (8.8) and the relation between q and q' which reads: $q' = \frac{\epsilon_1 - \epsilon_2}{\epsilon_2 + \epsilon_1} q = -\frac{\epsilon_2 - \epsilon_1}{\epsilon_2 + \epsilon_1} q$.

Therefore we have:

$$\varphi_1 = \frac{1}{4\pi\epsilon_0\epsilon_1} \left(\frac{q}{\sqrt{x^2 + y^2 + (z-d)^2}} - \left(\frac{\epsilon_2 - \epsilon_1}{\epsilon_1 + \epsilon_2} \right) \frac{q}{\sqrt{x^2 + y^2 + (z+d)^2}} \right) \quad (8.16)$$

where we can recognise the contribution arising from the image charge in the second region.

Thanks to the superposition principle we can now address the problem concerning the potential energy in a system with two different charges in both media, as reported in Figure 51. The system comprises of the screened charge q'' and an elementary charge in region 2 which gives rise to a self-image charge, occupying a position symmetric to the interface.

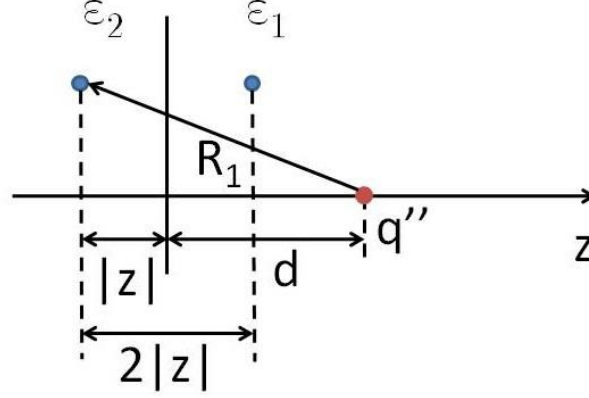


Figure 51. Screened charge q'' and self-image system interacting with an extra charge in the second medium.

It must be stressed that the image charge is a fictitious charge, which is employed to mimic the effect of a polarisation charge on the surface due to the presence of an electron in the second medium, hence it must have same magnitude and opposite sign to the extra electron in the same medium, so the force acting between the two is an attractive one. The potential generated by the image charge undergoes the very same screening on account of the two dielectrics as the charge q' did in the previous section. Therefore, if we refer to the image charge as e' , then the relation with the generating charge e can be written as $e' = -\frac{\epsilon_2 - \epsilon_1}{\epsilon_2 + \epsilon_1}e$. Following Taddei [230], we can write the Coulomb force acting between the electron and its image charge as:

$$\vec{F}(z) = -\hat{z} \frac{e^2}{4\pi\epsilon_0\epsilon_2} \left(\frac{\epsilon_2 - \epsilon_1}{\epsilon_2 + \epsilon_1} \right) \cdot \frac{1}{(2z)^2} \quad (8.17)$$

From which we can derive the potential energy for the electron self-interaction as the work required to bring the (real) charges to the final configuration:

$$V_{self-imag} = -W_{ext} = -\int_{-\infty}^z \vec{F}(z') \cdot \hat{z}' dz'. \text{ This integral can be evaluated to give:}$$

$$V_{self-imag} = -\frac{e^2}{4\pi\epsilon_0\epsilon_2} \left(\frac{\epsilon_2 - \epsilon_1}{\epsilon_2 + \epsilon_1} \right) \frac{1}{4|z|} \quad (8.18)$$

This expression has been given by Muljarov et al. [231] in the context of quantum wells and can be used as an operative definition of the self-energy for the electron at the interface.

Table 6. Expression for the potential field φ generated by an image charge in the second medium (first two rows, compare with equation (8.16)) and potential energy for the interaction of a charge with its image in the same medium (last two rows).

Expression for the potential field and potential energy according to reference	Reference
$\varphi = \frac{1}{4\pi\epsilon_0\epsilon_1} \left(\frac{\epsilon_1 - \epsilon_2}{\epsilon_1 + \epsilon_2} \right) \frac{q}{ d - z }$	Sometani 1977 [232]
$\varphi = \frac{1}{4\pi\epsilon_0} \left(\frac{\epsilon_1 - \epsilon_2}{\epsilon_1 + \epsilon_2} \right) \frac{q}{ d - z }$	Sometani 2000 [233]
$V_{self-imag} = -\frac{e^2}{4\pi\epsilon_0} \left(\frac{\epsilon_2 - \epsilon_1}{\epsilon_1 + \epsilon_2} \right) \frac{1}{4z}$	Zhu 2009 [229]
$V_{self-imag} = -\frac{e^2}{4\pi\epsilon_0\epsilon_2} \left(\frac{\epsilon_2 - \epsilon_1}{\epsilon_2 + \epsilon_1} \right) \frac{1}{4 z }$	Muljarov 1995 [231]

The problem of image charges at the interface has been previously dealt with in the scientific literature. We report the expression for the potential found in Table 6: it is quite surprising that they are not consistent with each other concerning the presence of the dielectric constant of the medium in which the charge is embedded.

For this reason we have reposed the derivation in this appendix, recovering the results given in Refs. [231, 232].

8.6 Appendix: Derivation of the matrix elements recursion relations

Here we report the explicit derivation for the Hamiltonian matrix elements evaluated over the basis set functions. We report the Hamiltonian as a starting point:

$$\hat{H} = -\frac{\hbar^2}{2\mu} \nabla_{\mathbf{r}}^2 - \frac{\beta e^2}{16\pi\epsilon_0\epsilon_2 z} - \frac{\gamma e^2}{4\pi\epsilon_0 \sqrt{\rho^2 + (z + z_h)^2}} \quad (8.19)$$

Were the symbols have been previously defined. Since the potential term does not depend on the angular coordinate, it is possible to factorise out the solution as $\Omega(\rho, \varphi, z) = \Theta(\rho, z) \cdot \Phi(\varphi)$, and therefore the eigenvalue equation can be recast as:

$$\left\{ \begin{aligned} & -\frac{\hbar^2}{2\mu} \left\{ \frac{\partial^2}{\partial \rho^2} + \frac{1}{\rho} \frac{\partial}{\partial \rho} - \frac{m^2}{\rho^2} + \frac{\partial^2}{\partial z^2} \right\} \Theta(\rho, z) - \frac{e^2}{4\pi\epsilon_0} \left\{ \frac{\beta}{4\epsilon_2 z} + \frac{\gamma}{\sqrt{\rho^2 + (z + z_h)^2}} \right\} \Theta(\rho, z) = E \Theta(\rho, z) \\ & \frac{d^2}{d\varphi^2} \Phi(\varphi) = -m^2 \Phi(\varphi) \end{aligned} \right. \quad (8.20)$$

This allows us to immediately find the angular dependence in the effective one body wavefunction as: $\Phi(\varphi) = \frac{1}{\sqrt{2\pi}} e^{im\varphi}$; in order to meet periodicity requirement we must have $m = 0, \pm 1, \pm 2, \dots$. The original problem has been reduced into two dimensions, depending on the additional parameter m which is can be thought of as an angular quantum number [234].

To address the variational solution for the model above, we perform the change of variable for the radial coordinate: $\xi = \frac{\sigma}{2} \rho^2$ where σ is a scaling coefficient which can be obtained by variational minimisation of the ground state energy. The top equation in (8.20) reads:

$$E\Psi(\xi, z) = -\frac{\hbar^2}{2\mu} \left\{ 2\sigma\xi \frac{\partial^2}{\partial \xi^2} + 2\sigma \frac{\partial}{\partial \xi} - \frac{\sigma m^2}{2\xi} + \frac{\partial^2}{\partial z^2} \right\} \Psi(\xi, z) - \frac{e^2}{4\pi\epsilon_0} \left\{ \frac{\beta}{4z} + \frac{\gamma}{\sqrt{\frac{2}{\sigma}\xi + (z+z_h)^2}} \right\} \Psi(\xi, z) \quad (8.21)$$

It is to solve this equation that we have to resort to the variational technique as already mentioned. We proceed with the evaluation of the terms containing differential operators. These are:

$$\hat{D}_T = -\frac{\hbar^2}{2\mu} \left\{ \frac{1}{\rho} \frac{\partial}{\partial \rho} \left(\rho \frac{\partial}{\partial \rho} \right) + \frac{\partial^2}{\partial z^2} \right\} \quad (8.22)$$

Hence the kinetic part of the Hamiltonian matrix can be evaluated through the integral: $\langle R_k^{[m]} \Lambda_w | \hat{K}_T | R_l^{[m]} \Lambda_v \rangle$, with $\hat{K}_T = \hat{D}_T + \frac{\hbar^2 m^2}{\mu \rho^2}$ which, in turn, can be decomposed according to the following expression:

$$\langle R_k^{[m]} \Lambda_w | \hat{K}_T | R_l^{[m]} \Lambda_v \rangle = \langle R_k^{[m]} | \hat{K}_\xi | R_l^{[m]} \rangle \cdot \langle \Lambda_w | \Lambda_v \rangle + \langle R_k^{[m]} | R_l^{[m]} \rangle \cdot \langle \Lambda_w | \hat{K}_z | \Lambda_v \rangle \quad (8.23)$$

The matrix elements for the z part are particularly straightforward to evaluate:

$$\langle \Lambda_w | \hat{K}_z | \Lambda_v \rangle = \frac{\hbar^2}{2\mu} \cdot \frac{2}{L} \cdot \frac{v^2 \pi^2}{L^2} \int_0^L dz \sin\left(\frac{w\pi}{L} z\right) \sin\left(\frac{v\pi}{L} z\right) \quad (8.24)$$

For the radial coordinate the integral is more involved because of the change of variable to carry out both in the differential operator and in the integral. We give therefore an explicit account for the expression to compute (with m we refer to the absolute value of the angular quantum number) for the integrals:

$$\left\langle R_k^m \left| -\frac{d^2}{d\rho^2} R_l^m \right. \right\rangle = -\left\langle R_k^m \left| \left(\frac{d\xi}{d\rho} \right)^2 \frac{d^2}{d\xi^2} + \frac{d^2\xi}{d\rho^2} \frac{d}{d\xi} R_l^m \right. \right\rangle \quad (8.25)$$

$$\left\langle R_k^m \left| -\frac{1}{\rho} \frac{d}{d\rho} R_l^m \right. \right\rangle = -\left\langle R_k^m \left| \sqrt{\frac{\sigma}{2\xi}} \frac{d\xi}{d\rho} \frac{d}{d\xi} R_l^m \right. \right\rangle \quad (8.26)$$

Rearranging the previous integrals we can define two distinct contributions to the kinetic term $\left\langle R_k^m \left| \hat{K}_\xi \right| R_l^m \right\rangle = N_{k,l} \{T_{k,l} + K_{k,l}\}$, where:

$$T_{kl} = -\int_0^{+\infty} d\xi e^{-\frac{\xi}{2}} \xi^{\frac{m}{2}} L_k^m(\xi) \left(2\xi \frac{d^2}{d\xi^2} \left(e^{-\frac{\xi}{2}} \xi^{\frac{m}{2}} L_l^m(\xi) \right) \right) \quad (8.27)$$

$$K_{kl} = -\int_0^{+\infty} d\xi e^{-\frac{\xi}{2}} \xi^{\frac{m}{2}} L_k^m(\xi) \left(2 \frac{d}{d\xi} \left(e^{-\frac{\xi}{2}} \xi^{\frac{m}{2}} L_l^m(\xi) \right) \right) \quad (8.28)$$

The final expression, combining the previous two, reads:

$$\left\langle R_k^m \left| \hat{K}_\xi \right| R_l^m \right\rangle = N_{kl} \left\{ \left(l + \frac{m}{2} + \frac{1}{2} \right) I[m, k, l] - \frac{m^2}{4} I[m-1, k, l] - \frac{1}{4} I[m+1, k, l] \right\} \quad (8.29)$$

where we have used the shorthand notation:

$$I[m+\alpha, i, j] = \int_0^{+\infty} d\xi e^{-\xi} \xi^{m+\alpha} L_i^m(\xi) L_j^m(\xi) \text{ and } N \text{ is the normalisation constant.}$$

The Potential term is more obvious and can be obtained immediately as the sum of two contributions:

$$\langle R_k^m \Lambda_w | \hat{V}_T | R_l^m \Lambda_v \rangle = \langle R_k^m | R_l^m \rangle \cdot \langle \Lambda_w | \hat{V}_\beta | \Lambda_v \rangle + \langle R_k^m \Lambda_w | \hat{V}_\gamma | R_l^m \Lambda_v \rangle \quad (8.30)$$

Where we have tacitly introduced the operators: $\hat{V}_\beta = \frac{e^2}{4\pi\epsilon_0} \cdot \frac{\beta}{4\epsilon_2 \hat{z}}$ and

$\hat{V}_\gamma = -\frac{e^2}{4\pi\epsilon_0} \cdot \frac{\gamma}{\sqrt{2\sigma\xi + \sigma^2(\hat{z} + z_h)^2}}$; we indicate the position operators with the

corresponding spatial variables with a hat sign. The abstract notation above can be recast in terms of its real space representation as:

$$\langle \Lambda_w | \hat{V}_\beta | \Lambda_v \rangle = -\frac{e^2 \beta}{8\pi\epsilon_0 \epsilon_2 L} \int_0^L dz \sin\left(\frac{w\pi}{L} z\right) \frac{1}{z} \sin\left(\frac{v\pi}{L} z\right) \quad (8.31)$$

$$\langle R_k^m \Lambda_w | \hat{V}_\gamma | R_l^m \Lambda_v \rangle = -\frac{e^2 \gamma N_{k,l}}{2\pi\epsilon_0 L} \iint_D \frac{d\xi dz}{\sqrt{2\sigma\xi + \sigma^2(z + z_h)^2}} \sin\left(\frac{w\pi}{L} z\right) e^{-\xi} \xi^m L_k^m(\xi) \sin\left(\frac{v\pi}{L} z\right) L_l^m(\xi) \quad (8.32)$$

In the previous equation the integration domain D stands for $[0, \infty) \times [0, L]$.

Conclusions

In this thesis we have developed a phenomenological theory for the charge recombination in dye sensitised solar cells (DSSCs) and applied on several realistic systems using DFT electronic structure calculations. The importance of the charge recombination processes and the limitations of current theoretical methods have been highlighted and an expression for the pseudo-first order rate has been derived in chapter 2. The quantities required for its evaluation can be related to properties of the molecular system (the Franck-Condon term), to the strength of the interaction between the adsorbate molecule and the semiconductor (the spectral density) and to the occupation of electronic states in the semiconductor. The computational procedure for the molecular quantities has been described in chapter 3, while various evaluations of the spectral density have been discussed throughout the thesis. On the other hand, the model proposed does not offer a self-contained description of the process as the electron population in the semiconductor is a function of the energy levels alignment, which is inferred from experimental data. The uncertainty on this variable is considerably reduced in chapter 4, where a more extensive characterisation of the electrolyte charge recombination is available. The model is, however, capable of reproducing the correct ranking (slow to fast) for the dyes considered in chapter 3 for the whole permissible range of experimental variables. Hence, we expect the insight gained by using this model to be robust with respect to changes in the details of the energy levels positions.

In particular, the strategies proposed for the minimisation of the charge recombination rate (presented in chapters 6 and 7) are based on a partitioning scheme

of the sensitizer molecule which has been intuitively applied by experimentalists since the early days of the research in the field of DSSCs. Applying results from scattering theory, we express the coupling term as the sum of two contributions, the first accounts for the direct interaction semiconductor-molecule, while the second includes the features of the bridge connecting the semiconductor with the chromophore unit in the dye. The first term is analysed in chapter 6, where suitably symmetric chromophores have shown a significant improvement of the charge recombination kinetics when compared against similar dyes that lack the symmetry requirement. In chapter 7 the contribution of the bridge unit is taken into account and it is shown that by modifying its chemical structure the charge recombination can be significantly modulated. In both chapters the description of the model system is substantiated by DFT electronic structure calculations and, for more complicated scenarios, tight binding models have been fruitfully applied to rationalise the main features. Furthermore, the model proposed highlights a connection with the Landauer formalism of charge transport through molecular junctions, hence allowing for concepts and strategies developed in this field to be applied to the case of DSSCs.

An outline of ‘conventional’ optimisation strategies, based on tuning the molecular properties of dye and electrolyte has been reported in chapter 5. The model employed therein includes the contribution from lattice defects which are common in real devices; unfortunately, the evidence gathered points towards the lack of a universal optimisation strategy involving only the molecular parameters. This result is consistent with the extensive literature on DSSCs where several families of dyes and redox couples have been tested, and the registered improvements have been

only incremental. On this ground, we hope that the implementation of the strategies we suggest could lead to substantially more efficient devices.

The theoretical description offered in this thesis relies on some subtleties, for instance the out-of-equilibrium electronic population present in the semiconductor's conduction band is assumed to follow the Fermi-Dirac distribution, which holds rigorously for non-interacting fermionic systems in thermal equilibrium. This assumption is well-accepted in the current literature and the evaluation of chemical potential in operational conditions can be carried out experimentally. However, the many shortcomings of the current reaction-diffusion model used to interpret the experimental results may call this assumption into question, particularly in the limit of high illumination intensities, where the non-ideal (diode) behaviour is more pronounced.

Another intriguing issue concerns the nanoporous structure of the photoelectrode, peculiar to DSSCs. Specifically, the solution that permeates the electrode can be constricted in small volumes that do not allow for interfacial effects to decay completely in the centre of pores, as mentioned in chapter 8, thus impacting on the solvent local dielectric properties. The relatively high concentration of species in solution ($> 20\%$ in volume) and the characteristics of the pores can also lead to a position-dependent diffusion coefficient, which would impact on the electrolyte double layer and hence on the surface charge distribution in the semiconductor. In this regard, more theoretical studies are needed to disentangle the different mechanisms operating in such a complex environment. The theory presented in this thesis can be adapted in principle to take these effects into account and we also

expect it to be transferrable to a large degree to other semiconductor-molecule architectures.

Bibliography

- [1] *Key World Energy Statistics*; International Energy Agency, 2011.
- [2] Price, S.; Margolis, R. *Solar Technologies Market Report*; U.S. Department of Energy, 2008.
- [3] O'Regan, B.; Grätzel, M. *Nature* **1991**, 353, 737–740.
- [4] Yella, A.; Lee, H.-W.; Tsao, H. N.; Yi, C.; Chandiran, A. K.; Nazeeruddin, M. K.; Diau, E. W.-G.; Yeh, C.-Y.; Zakeeruddin, S. M.; Grätzel, M. *Science* **2011**, 334, 629–634.
- [5] Miyasaka, T. *J. Phys. Chem. Lett.* **2011**, 2, 262–269.
- [6] Mishra, A.; Fischer, M. K. R.; Bäuerle, P. *Angew. Chem. Int. Ed.* **2009**, 48, 2474–2499.
- [7] Hagfeldt, A.; Boschloo, G.; Sun, L.; Kloo, L.; Pettersson, H. *Chem. Rev.* **2010**, 110, 6595–6663.
- [8] Listorti, A.; O'Regan, B.; Durrant, J. R. *Chem. Mater.* **2011**, 23, 3381–3399.
- [9] Enache-Pommer, E.; Liu, B.; Aydil, E. S. *Phys. Chem. Chem. Phys.* **2009**, 11, 9648–9652.
- [10] Law, M.; Greene, L. E.; Johnson, J. C.; Saykally, R.; Yang, P. *Nat Mater* **2005**, 4, 455–459.
- [11] Ramasamy, E.; Lee, J. *J. Phys. Chem. C* **2010**, 114, 22032–22037.
- [12] Diamant, Y.; Chappel, S.; Chen, S. G.; Melamed, O.; Zaban, A. *Coord. Chem. Rev.* **2004**, 248, 1271–1276.
- [13] Lenzmann, F.; Krueger, J.; Burnside, S.; Brooks, K.; Grätzel, M.; Gal, D.; Rühle, S.; Cahen, D. *J. Phys. Chem. B* **2001**, 105, 6347–6352.
- [14] Clifford, J. N.; Martinez-Ferrero, E.; Viterisi, A.; Palomares, E. *Chem. Soc. Rev.* **2011**, 40, 1635–1646.
- [15] Yum, J.-H.; Baranoff, E.; Wenger, S.; Nazeeruddin, M. K.; Gratzel, M. *Energy Environ. Sci.* **2011**, 4, 842–857.
- [16] Asbury, J. B.; Hao, E.; Wang, Y.; Ghosh, H. N.; Lian, T. *J. Phys. Chem. B* **2001**, 105, 4545–4557.
- [17] Wiberg, J.; Marinado, T.; Hagberg, D. P.; Sun, L.; Hagfeldt, A.; Albinsson, B. *J. Phys. Chem. C* **2009**, 113, 3881–3886.
- [18] Choi, H.; Kang, S. O.; Ko, J.; Gao, G.; Kang, H. S.; Kang, M.-S.; Nazeeruddin, M. K.; Grätzel, M. *Angew. Chem. Int. Ed.* **2009**, 48, 5938–5941.
- [19] Liang, Y.; Peng, B.; Chen, J. *J. Phys. Chem. C* **2010**, 114, 10992–10998.
- [20] Paek, S.; Choi, H.; Choi, H.; Lee, C.-W.; Kang, M.; Song, K.; Nazeeruddin, M. K.; Ko, J. *J. Phys. Chem. C* **2010**, 114, 14646–14653.
- [21] Hamann, T. W.; Jensen, R. A.; Martinson, A. B. F.; Van Ryswyk, H.; Hupp, J. T. *Energy Environ. Sci.* **2008**, 1, 66–78.
- [22] Yum, J.-H.; Baranoff, E.; Kessler, F.; Moehl, T.; Ahmad, S.; Bessho, T.; Marchioro, A.; Ghadiri, E.; Moser, J.-E.; Yi, C.; Nazeeruddin, M. K.; Grätzel, M. *Nat. Commun.* **2012**, 3, 631.
- [23] Wang, H.; Nicholson, P. G.; Peter, L.; Zakeeruddin, S. M.; Grätzel, M. *J. Phys. Chem. C* **2010**, 114, 14300–14306.
- [24] Daeneke, T.; Kwon, T.-H.; Holmes, A. B.; Duffy, N. W.; Bach, U.; Spiccia, L. *Nat. Chem.* **2011**, 3, 211–215.

- [25] Wang, M.; Chamberland, N.; Breau, L.; Moser, J.-E.; Humphry-Baker, R.; Marsan, B.; Zakeeruddin, S. M.; Grätzel, M. *Nat Chem* **2010**, *2*, 385–389.
- [26] Cappel, U. B.; Smeigh, A. L.; Plogmaker, S.; Johansson, E. M. J.; Rensmo, H.; Hammarström, L.; Hagfeldt, A.; Boschloo, G. *J. Phys. Chem. C* **2011**, *115*, 4345–4358.
- [27] Yu, S.; Ahmadi, S.; Sun, C.; Palmgren, P.; Hennies, F.; Zuleta, M.; Göthelid, M. *J. Phys. Chem. C* **2010**, *114*, 2315–2320.
- [28] Wang, Z.-S.; Cui, Y.; Dan-oh, Y.; Kasada, C.; Shinpo, A.; Hara, K. *J. Phys. Chem. C* **2007**, *111*, 7224–7230.
- [29] O'Regan, B. C.; Durrant, J. R.; Sommeling, P. M.; Bakker, N. J. *J. Phys. Chem. C* **2007**, *111*, 14001–14010.
- [30] O'Regan, B.; Xiaoe, L.; Ghaddar, T. *Energy Environ. Sci.* **2012**, *5*, 7203–7215.
- [31] Halme, J.; Vahermaa, P.; Miettunen, K.; Lund, P. *Adv. Mater.* **2010**, *22*, E210–E234.
- [32] Bisquert, J.; Vikhrenko, V. S. *J. Phys. Chem. B* **2004**, *108*, 2313–2322.
- [33] Bisquert, J.; Fabregat-Santiago, F.; Mora-Seró, I.; Garcia-Belmonte, G.; Giménez, S. *J. Phys. Chem. C* **2009**, *113*, 17278–17290.
- [34] Schlichthörl, G.; Huang, S. Y.; Sprague, J.; Frank, A. J. *J. Phys. Chem. B* **1997**, *101*, 8141–8155.
- [35] Oekermann, T.; Zhang, D.; Yoshida, T.; Minoura, H. *J. Phys. Chem. B* **2004**, *108*, 2227–2235.
- [36] O'Regan, B. C.; Scully, S.; Mayer, A. C.; Palomares, E.; Durrant, J. *J. Phys. Chem. B* **2005**, *109*, 4616–4623.
- [37] Nakade, S.; Kanzaki, T.; Wada, Y.; Yanagida, S. *Langmuir* **2005**, *21*, 10803–10807.
- [38] Nissfolk, J.; Fredin, K.; Hagfeldt, A.; Boschloo, G. *J. Phys. Chem. B* **2006**, *110*, 17715–17718.
- [39] Boschloo, G.; Hagfeldt, A. *J. Phys. Chem. B* **2005**, *109*, 12093–12098.
- [40] Zaban, A.; Greenshtein, M.; Bisquert, J. *ChemPhysChem* **2003**, *4*, 859–864.
- [41] Bisquert, J.; Zaban, A.; Greenshtein, M.; Mora-Seró, I. *J. Am. Chem. Soc.* **2004**, *126*, 13550–13559.
- [42] Barnes, P. R. F.; Anderson, A. Y.; Juozapavicius, M.; Liu, L.; Li, X.; Palomares, E.; Forneli, A.; O'Regan, B. C. *Phys. Chem. Chem. Phys.* **2011**, *13*, 3547–3558.
- [43] Duffy, N. W.; Peter, L. M.; Rajapakse, R. M. G.; Wijayantha, K. G. U. *Electrochem. Commun.* **2000**, *2*, 658–662.
- [44] Green, A. N. M.; Chandler, R. E.; Haque, S. A.; Nelson, J.; Durrant, J. R. *J. Phys. Chem. B* **2004**, *109*, 142–150.
- [45] Montanari, I.; Nelson, J.; Durrant, J. R. *J. Phys. Chem. B* **2002**, *106*, 12203–12210.
- [46] Bauer, C.; Boschloo, G.; Mukhtar, E.; Hagfeldt, A. *J. Phys. Chem. B* **2002**, *106*, 12693–12704.
- [47] Miettunen, K.; Halme, J.; Visuri, A.-M.; Lund, P. *J. Phys. Chem. C* **2011**, *115*, 7019–7031.
- [48] Anta, J. A.; Casanueva, F.; Oskam, G. *J. Phys. Chem. B* **2006**, *110*, 5372–5378.

- [49] Villanueva-Cab, J.; Oskam, G.; Anta, J. A. *Sol. Energ. Mat. Sol. Cells* **2010**, *94*, 45–50.
- [50] Clifford, J. N.; Palomares, E.; Nazeeruddin, M. K.; Grätzel, M.; Nelson, J.; Li, X.; Long, N. J.; Durrant, J. R. *J. Am. Chem. Soc.* **2004**, *126*, 5225–5233.
- [51] Barnes, P. R. F.; Anderson, A. Y.; Durrant, J. R.; O'Regan, B. C. *Phys. Chem. Chem. Phys.* **2011**, *13*, 5798–5816.
- [52] Fabregat-Santiago, F.; Bisquert, J.; Garcia-Belmonte, G.; Boschloo, G.; Hagfeldt, A. *Sol. Energ. Mat. Sol. Cells* **2005**, *87*, 117–131.
- [53] Jennings, J. R.; Ghicov, A.; Peter, L. M.; Schmuki, P.; Walker, A. B. *J. Am. Chem. Soc.* **2008**, *130*, 13364–13372.
- [54] Jose, R.; Kumar, A.; Thavasi, V.; Fujihara, K.; Uchida, S.; Ramakrishna, S. *Appl. Phys. Lett.* **2008**, *93*, 23123–23125.
- [55] Ma, R.; Guo, P.; Cui, H.; Zhang, X.; Nazeeruddin, M. K.; Grätzel, M. *J. Phys. Chem. A* **2009**, *113*, 10119–10124.
- [56] Martsinovich, N.; Troisi, A. *J. Phys. Chem. C* **2011**, *115*, 11781–11792.
- [57] Kurashige, Y.; Nakajima, T.; Kurashige, S.; Hirao, K.; Nishikitani, Y. *J. Phys. Chem. A* **2007**, *111*, 5544–5548.
- [58] Le Bahers, T.; Pauporte, T.; Scalmani, G.; Adamo, C.; Ciofini, I. *Phys. Chem. Chem. Phys.* **2009**, *11*, 11276–11284.
- [59] Martsinovich, N.; Ambrosio, F.; Troisi, A. *Phys. Chem. Chem. Phys.* **2012**, *14*, 16668–16676.
- [60] Anselmi, C.; Mosconi, E.; Pastore, M.; Ronca, E.; De Angelis, F. *Phys. Chem. Chem. Phys.* **2012**, *14*, 15963–15974.
- [61] Martsinovich, N.; Jones, D. R.; Troisi, A. *J. Phys. Chem. C* **2010**, *114*, 22659–22670.
- [62] Mosconi, E.; Selloni, A.; De Angelis, F. *J. Phys. Chem. C* **2012**, *116*, 5932–5940.
- [63] Ronca, E.; Pastore, M.; Belpassi, L.; Tarantelli, F.; De Angelis, F. *Energy Environ. Sci.* **2013**, *6*, 183–193.
- [64] Cheng, J.; Sulpizi, M.; Sprik, M. *J. Chem. Phys.* **2009**, *131*, 154504–154520.
- [65] Yu, Q.; Wang, Y.; Yi, Z.; Zu, N.; Zhang, J.; Zhang, M.; Wang, P. *ACS Nano* **2010**, *4*, 6032–6038.
- [66] Bai, Y.; Zhang, J.; Wang, Y.; Zhang, M.; Wang, P. *Langmuir* **2011**, *27*, 4749–4755.
- [67] Cheng, J.; Sprik, M. *Phys. Rev. B* **2010**, *82*, 81406.
- [68] Nelson, J.; Haque, S. A.; Klug, D. R.; Durrant, J. R. *Phys. Rev. B* **2001**, *63*, 205321.
- [69] Li, J.; Nilsing, M.; Kondov, I.; Wang, H.; Persson, P.; Lunell, S.; Thoss, M. *J. Phys. Chem. C* **2008**, *112*, 12326–12333.
- [70] Wang, L.; Willig, F.; May, V. *J. Chem. Phys.* **2006**, *124*, 14711–14712.
- [71] Li, J.; Kondov, I.; Wang, H.; Thoss, M. *J. Phys. Chem. C* **2010**, *114*, 18481–18493.
- [72] Sebastian, K. L.; Tachiya, M. *J. Chem. Phys.* **2006**, *124*, 64710–64713.
- [73] Tsivlin, D. V.; Willig, F.; May, V. *Phys. Rev. B* **2008**, *77*, 35319.
- [74] Wang, L.; May, V. *Chem. Phys.* **2009**, *361*, 1–8.
- [75] Li, Z.; Zhang, X.; Lu, G. *J. Phys. Chem. B* **2010**, *114*, 17077–17083.

- [76] Duncan, W. R.; Craig, C. F.; Prezhdo, O. V *J. Am. Chem. Soc.* **2007**, *129*, 8528–8543.
- [77] Prezhdo, O. V; Duncan, W. R.; Prezhdo, V. V *Acc. Chem. Res.* **2008**, *41*, 339–348.
- [78] Stier, W.; Prezhdo, O. V *J. Phys. Chem. B* **2002**, *106*, 8047–8054.
- [79] Abuabara, S. G.; Rego, L. G. C.; Batista, V. S. *J. Am. Chem. Soc.* **2005**, *127*, 18234–18242.
- [80] Rego, L. G. C.; Batista, V. S. *J. Am. Chem. Soc.* **2003**, *125*, 7989–7997.
- [81] Da Silva, R.; Rego, L. G. C.; Freire, J. A.; Rodriguez, J.; Laria, D.; Batista, V. S. *J. Phys. Chem. C* **2010**, *114*, 19433–19442.
- [82] Wang, H.; Thoss, M. *J. Chem. Phys.* **2009**, *131*, 24114.
- [83] Kestner, N. R.; Logan, J.; Jortner, J. *J. Phys. Chem.* **1974**, *78*, 2148–2166.
- [84] Nitzan, A. *Chemical Dynamics in Condensed Phases: relaxation, transfer, and reactions in condensed molecular systems*; Oxford University Press: Oxford, 2006; pp. xxii, 719.
- [85] Schmickler, W. *J. Electroanal. Chem.* **1986**, *204*, 31–43.
- [86] Schmickler, W. *Chem. Phys. Lett.* **1995**, *237*, 152–160.
- [87] Newns, D. M. *Phys. Rev.* **1969**, *178*, 1123–1135.
- [88] Haldane, F. D. M.; Anderson, P. W. *Phys. Rev. B* **1976**, *13*, 2553–2559.
- [89] Davydov, S. Y.; Troshin, S. V. *Phys. Solid State* **2007**, *49*, 1583–1588.
- [90] Siders, P.; Marcus, R. A. *J. Am. Chem. Soc.* **1981**, *103*, 741–747.
- [91] Powell, J. L.; Crasemann, B. *Quantum Mechanics*; Addison-Wesley Publishing Company, Inc.: Reading, London, 1961; p. 495.
- [92] Gradshteyn, I. S.; Ryzhik, I. M. *Table of Integrals, Series and Products*; Jeffrey, A.; Zwillinger, D., Eds.; 6th ed.; Academic Press: San Diego; London, 2000.
- [93] Albeverio, S. A.; Høegh-Krohn, R. J.; Mazzucchi, S. *Mathematical Theory of Feynman Path Integrals*; Morel, J.-M.; Takens, F.; Teissier, B., Eds.; 2nd ed.; Springer-Verlag: Berlin-Heidelberg, 2008.
- [94] Markham, J. *Rev. Mod. Phys.* **1959**, *31*, 956–989.
- [95] McConnell, H. M. *J. Chem. Phys.* **1961**, *35*, 508–515.
- [96] Mujica, V.; Kemp, M.; Ratner, M. A. *J. Chem. Phys.* **1994**, *101*, 6849–6855.
- [97] Hansen, T.; Solomon, G. C.; Andrews, D. Q.; Ratner, M. A. *J. Chem. Phys.* **2009**, *131*, 194704–194712.
- [98] De Santana, O. L.; da Gama, A. A. S. *Chem. Phys. Lett.* **1999**, *314*, 508–515.
- [99] Magarshak, Y.; Malinsky, J.; Joran, A. D. *J. Chem. Phys.* **1991**, *95*, 418–432.
- [100] Goldman, C. *Phys. Rev. A* **1991**, *43*, 4500–4509.
- [101] Fetter, A. L.; Walecka, J. D. *Quantum Theory of Many-Particle Systems*; Schiff, L. I., Ed.; McGraw-Hill, Inc.: New York, 1971; p. 601.
- [102] Mukamel, S. *Principles of Nonlinear Optical Spectroscopy*; Oxford University Press: Oxford, 1996; p. 543.
- [103] Thygesen, K. S. *Phys. Rev. B* **2006**, *73*, 35309.
- [104] Maggio, E.; Martsinovich, N.; Troisi, A. *J. Chem. Phys.* **2012**, *137*, 22A508.
- [105] Xue, Y.; Datta, S.; Ratner, M. A. *Chem. Phys.* **2002**, *281*, 151–170.
- [106] Mujica, V.; Kemp, M.; Ratner, M. A. *J. Chem. Phys.* **1994**, *101*, 6856–6864.
- [107] Gruhn, N. E.; da Silva Filho, D. A.; Bill, T. G.; Malagoli, M.; Coropceanu, V.; Kahn, A.; Brédas, J.-L. *J. Am. Chem. Soc.* **2002**, *124*, 7918–7919.

- [108] Liu, T.; Troisi, A. *J. Phys. Chem. C* **2011**, *115*, 2406–2415.
- [109] Wang, Q.; Ito, S.; Grätzel, M.; Fabregat-Santiago, F.; Mora-Seró, I.; Bisquert, J.; Bessho, T.; Imai, H. *J. Phys. Chem. B* **2006**, *110*, 25210–25221.
- [110] Bisquert, J. *Phys. Chem. Chem. Phys.* **2008**, *10*, 3175–3194.
- [111] Bisquert, J.; Zaban, A.; Salvador, P. *J. Phys. Chem. B* **2002**, *106*, 8774–8782.
- [112] Li, Z.; Zhang, X.; Lu, G. *J. Phys. Chem. B* **2010**, *114*, 17077–17083.
- [113] Gregg, B. A. *J. Phys. Chem. B* **2003**, *107*, 4688–4698.
- [114] Schmickler, W.; Santos, E. *Interfacial Electrochemistry*; Springer: Berlin, Heidelberg, 2010.
- [115] McMahon, D. P.; Troisi, A. *Phys. Chem. Chem. Phys.* **2011**, *13*, 10241–10248.
- [116] Jones, D. R.; Troisi, A. *Phys. Chem. Chem. Phys.* **2010**, *12*, 4625–4634.
- [117] Persson, P.; Lundqvist, M. J.; Ernstorfer, R.; Goddard, W. A.; Willig, F. *J. Chem. Theory Comput.* **2006**, *2*, 441–451.
- [118] Soler, J. M.; Artacho, E.; Gale, J. D.; García, A.; Junquera, J.; Ordejón, P.; Sánchez-Portal, D. *J. Phys.: Condens. Matter* **2002**, *14*, 2745–2779.
- [119] Perdew, J. P.; Burke, K.; Ernzerhof, M. *Phys. Rev. Lett.* **1997**, *78*, 1396 LP – 1396.
- [120] Moreno, J.; Soler, J. M. *Phys. Rev. B* **1992**, *45*, 13891.
- [121] Tomasi, J.; Mennucci, B.; Cammi, R. *Chem. Rev.* **2005**, *105*, 2999–3094.
- [122] Nazeeruddin, M. K.; De Angelis, F.; Fantacci, S.; Selloni, A.; Viscardi, G.; Liska, P.; Ito, S.; Bessho, T.; Gratzel, M. *J. Am. Chem. Soc.* **2005**, *127*, 16835–16847.
- [123] Jacquemin, D.; Perpète, E. A.; Scalmani, G.; Frisch, M. J.; Assfeld, X.; Ciofini, I.; Adamo, C. *J. Chem. Phys.* **2006**, *125*, 164324–164335.
- [124] Frisch, M. J.; Trucks, G. W.; Schlegel, H. B.; Scuseria, G. E.; Robb, M. A.; Cheeseman, J. R.; Montgomery Jr., J. A.; Vreven, T.; Kudin, K. N.; Burant, J. C.; Millam, J. M.; Iyengar, S. S.; Tomasi, J.; Barone, V.; Mennucci, B.; Cossi, M.; Scalmani, G.; Rega, N.; Petersson, G. A.; Nakatsuji, H.; Hada, M.; Ehara, M.; Toyota, K.; Fukuda, R.; Hasegawa, J.; Ishida, M.; Nakajima, T.; Honda, Y.; Kitao, O.; Nakai, H.; Klene, M.; Li, X.; Knox, J. E.; Hratchian, H. P.; Cross, J. B.; Bakken, V.; Adamo, C.; Jaramillo, J.; Gomperts, R.; Stratmann, R. E.; Yazyev, O.; Austin, A. J.; Cammi, R.; Pomelli, C.; Ochterski, J. W.; Ayala, P. Y.; Morokuma, K.; Voth, G. A.; Salvador, P.; Dannenberg, J. J.; Zakrzewski, V. G.; Dapprich, S.; Daniels, A. D.; Strain, M. C.; Farkas, O.; Malick, D. K.; Rabuck, A. D.; Raghavachari, K.; Foresman, J. B.; Ortiz, J. V.; Cui, Q.; Baboul, A. G.; Clifford, S.; Cioslowski, J.; Stefanov, B. B.; Liu, G.; Liashenko, A.; Piskorz, P.; Komaromi, I.; Martin, R. L.; Fox, D. J.; Keith, T.; Al-Laham, M. A.; Peng, C. Y.; Nanayakkara, A.; Challacombe, M.; Gill, P. M. W.; Johnson, B.; Chen, W.; Wong, M. W.; Gonzalez, C.; Pople, J. A. *Gaussian 03*, Revision C.02.
- [125] Takano, Y.; Houk, K. N. *J. Chem. Theory Comput.* **2004**, *1*, 70–77.
- [126] Marcus, R. A. *J. Chem. Phys.* **1965**, *43*, 679–701.
- [127] Scholes, G. D.; Ghiggino, K. P. *J. Chem. Phys.* **1994**, *101*, 1251–1261.
- [128] Li, X.-Y.; Tong, J.; He, F.-C. *Chem. Phys.* **2000**, *260*, 283–294.
- [129] Jagoda-Cwiklik, B.; Slaviček, P.; Cwiklik, L.; Nolting, D.; Winter, B.; Jungwirth, P. *J. Phys. Chem. A* **2008**, *112*, 3499–3505.

- [130] Vaissier, V.; Barnes, P.; Kirkpatrick, J.; Nelson, J. *Phys. Chem. Chem. Phys.* **2013**, *15*, 4804–14.
- [131] Venkataraman, C.; Soudackov, A. V.; Hammes-Schiffer, S. *J. Phys. Chem. C* **2008**, *112*, 12386–12397.
- [132] Gratzel, M. *Nature* **2001**, *414*, 338–344.
- [133] Peter, L. M. *J. Phys. Chem. C* **2007**, *111*, 6601–6612.
- [134] Torsi, L.; Sabbatini, L.; Zambonin, P. G. *Adv. Mater.* **1995**, *7*, 417–420.
- [135] Lobato, K.; Peter, L. M.; Würfel, U. *J. Phys. Chem. B* **2006**, *110*, 16201–16204.
- [136] Fabregat-Santiago, F.; Garcia-Belmonte, G.; Mora-Sero, I.; Bisquert, J. *Phys. Chem. Chem. Phys.* **2011**, *13*, 9083–9118.
- [137] Ooyama, Y.; Shimada, Y.; Inoue, S.; Nagano, T.; Fujikawa, Y.; Komaguchi, K.; Imae, I.; Harima, Y. *New J. Chem.* **2011**, *35*, 111–118.
- [138] Katoh, R.; Furube, A.; Mori, S.; Miyashita, M.; Sunahara, K.; Koumura, N.; Hara, K. *Energy Environ. Sci.* **2009**, *2*, 542–546.
- [139] Koops, S. E.; Barnes, P. R. F.; O'Regan, B. C.; Durrant, J. R. *J. Phys. Chem. C* **2010**, *114*, 8054–8061.
- [140] Hara, K.; Kurashige, M.; Dan-oh, Y.; Kasada, C.; Shinpo, A.; Suga, S.; Sayama, K.; Arakawa, H. *New J. Chem.* **2003**, *27*, 783–785.
- [141] Rühle, S.; Greenshtein, M.; Chen, S.-G.; Merson, A.; Pizem, H.; Sukenik, C. S.; Cahen, D.; Zaban, A. *J. Phys. Chem. B* **2005**, *109*, 18907–18913.
- [142] Kuciauskas, D.; Freund, M. S.; Gray, H. B.; Winkler, J. R.; Lewis, N. S. *J. Phys. Chem. B* **2000**, *105*, 392–403.
- [143] Ondersma, J. W.; Hamann, T. W. *J. Am. Chem. Soc.* **2011**, *133*, 8264–8271.
- [144] Boschloo, G.; Hagfeldt, A. *Acc. Chem. Res.* **2009**, *42*, 1819–1826.
- [145] Nakade, S.; Kanzaki, T.; Kubo, W.; Kitamura, T.; Wada, Y.; Yanagida, S. *J. Phys. Chem. B* **2005**, *109*, 3480–3487.
- [146] Treinin, A.; Hayon, E. *Int. J. Rad. Phys. Chem.* **1975**, *7*, 387–393.
- [147] Asaduzzaman, A. M.; Schreckenbach, G. *Phys. Chem. Chem. Phys.* **2010**, *12*, 14609–14618.
- [148] Asaduzzaman, A.; Schreckenbach, G. *Theor. Chem. Accounts Theor. Comput. Model. Theor. Chim. Acta* **2011**, *129*, 199–208.
- [149] Marcus, R. A. *J. Phys. Chem.* **1990**, *94*, 1050–1055.
- [150] Khimenko, M. T.; Gritsenko, N. N. *Zh. Fiz. Khim.* **1980**, *54*, 198–199.
- [151] Moreau, C.; Douhéret, G. *J. Chem. Thermodyn.* **1976**, *8*, 403–410.
- [152] Kawakita, M.; Kawakita, J.; Sakka, Y.; Shinohara, T. *J. Electrochem. Soc.* **2010**, *157*, H65–H68.
- [153] Spirina, O. B.; Cukier, R. I. *J. Chem. Phys.* **1996**, *104*, 538–550.
- [154] Datta, S. *Quantum transport: atom to transistor*; Cambridge University Press: Cambridge, UK; New York, 2005; pp. xiv, 404.
- [155] Maggio, E.; Martsinovich, N.; Troisi, A. *J. Phys. Chem. C* **2012**, *116*, 7638–7649.
- [156] Nelson, I. V.; Iwamoto, R. T. *J. Electroanal. Chem.* **1964**, *7*, 218–221.
- [157] Datta, J.; Bhattacharya, A.; Kundu, K. K. *Bull. Chem. Soc. Jpn.* **1988**, *61*, 1735–1742.
- [158] Dor, S.; Grinis, L.; Rühle, S.; Zaban, A. *J. Phys. Chem. C* **2009**, *113*, 2022–2027.

- [159] Boys, S. F.; Bernardi, F. *Mol. Phys.* **1970**, *19*, 553–566.
- [160] Santos, E.; Schmickler, W. *J. Electroanal. Chem.* **2007**, *607*, 101–106.
- [161] Peiró, A. M.; Colombo, C.; Doyle, G.; Nelson, J.; Mills, A.; Durrant, J. R. *J. Phys. Chem. B* **2006**, *110*, 23255–23263.
- [162] Boschloo, G.; Häggman, L.; Hagfeldt, A. *J. Phys. Chem. B* **2006**, *110*, 13144–13150.
- [163] Deskins, N. A.; Rousseau, R.; Dupuis, M. *J. Phys. Chem. C* **2010**, *114*, 5891–5897.
- [164] Martinez, U.; Hammer, B. *J. Chem. Phys.* **2011**, *134*, 194703–194707.
- [165] Miyashita, M.; Sunahara, K.; Nishikawa, T.; Uemura, Y.; Koumura, N.; Hara, K.; Mori, A.; Abe, T.; Suzuki, E.; Mori, S. *J. Am. Chem. Soc.* **2008**, *130*, 17874–17881.
- [166] Kavan, L.; Grätzel, M.; Gilbert, S. E.; Klenenz, C.; Scheel, H. J. *J. Am. Chem. Soc.* **1996**, *118*, 6716–6723.
- [167] O'Regan, B. C.; Durrant, J. R. *Acc. Chem. Res.* **2009**, *42*, 1799–1808.
- [168] Roy, J. C.; Hamill, W. H.; Williams, R. R. *J. Am. Chem. Soc.* **1955**, *77*, 2953–2957.
- [169] Boschloo, G.; Fitzmaurice, D. *J. Phys. Chem. B* **1999**, *103*, 2228–2231.
- [170] Fisher, A. C.; Peter, L. M.; Ponomarev, E. A.; Walker, A. B.; Wijayantha, K. G. U. *J. Phys. Chem. B* **2000**, *104*, 949–958.
- [171] Van de Lagemaat, J.; Frank, A. J. *J. Phys. Chem. B* **2000**, *104*, 4292–4294.
- [172] Papageorgiou, A. C.; Beglitis, N. S.; Pang, C. L.; Teobaldi, G.; Cabailh, G.; Chen, Q.; Fisher, A. J.; Hofer, W. A.; Thornton, G. *Proc. Natl. Acad. Sci.* **2010**, *107*, 2391–2396.
- [173] Yamamoto, T.; Ohno, T. *Phys. Chem. Chem. Phys.* **2012**, *14*, 589–598.
- [174] Aschauer, U.; He, Y.; Cheng, H.; Li, S.-C.; Diebold, U.; Selloni, A. *J. Phys. Chem. C* **2009**, *114*, 1278–1284.
- [175] Fabregat-Santiago, F.; Mora-Seró, I.; Garcia-Belmonte, G.; Bisquert, J. *J. Phys. Chem. B* **2002**, *107*, 758–768.
- [176] Minato, T.; Sainoo, Y.; Kim, Y.; Kato, H. S.; Aika, K.; Kawai, M.; Zhao, J.; Petek, H.; Huang, T.; He, W.; Wang, B.; Wang, Z.; Zhao, Y.; Yang, J.; Hou, J. G. *J. Chem. Phys.* **2009**, *130*, 124502–124511.
- [177] Cheng, H.; Selloni, A. *J. Chem. Phys.* **2009**, *131*, 54703–54710.
- [178] Stamate, M. D. *Appl. Surf. Sci.* **2003**, *205*, 353–357.
- [179] Jennings, J. R.; Liu, Y.; Wang, Q.; Zakeeruddin, S. M.; Gratzel, M. *Phys. Chem. Chem. Phys.* **2011**, *13*, 6637–6648.
- [180] Asbury, J. B.; Anderson, N. A.; Hao, E.; Ai, X.; Lian, T. *J. Phys. Chem. B* **2003**, *107*, 7376–7386.
- [181] Huang, W.-K.; Wu, H.-P.; Lin, P.-L.; Diau, E. W.-G. *J. Phys. Chem. C* **2013**, *117*, 2059–2065.
- [182] Myahkostupov, M.; Piotrowiak, P.; Wang, D.; Galoppini, E. *J. Phys. Chem. C* **2007**, *111*, 2827–2829.
- [183] Hartnig, C.; Koper, M. T. M. *J. Chem. Phys.* **2001**, *115*, 8540–8546.
- [184] Rosso, K. M.; Dupuis, M. *J. Chem. Phys.* **2004**, *120*, 7050–7054.
- [185] Isied, S. S.; Ogawa, M. Y.; Wishart, J. F. *Chem. Rev.* **1992**, *92*, 381–394.
- [186] Lu, H. P.; Xie, X. S. *J. Phys. Chem. B* **1997**, *101*, 2753–2757.
- [187] Cheng, H.; Selloni, A. *Phys. Rev. B* **2009**, *79*, 92101.

- [188] He, Y.; Dulub, O.; Cheng, H.; Selloni, A.; Diebold, U. *Phys. Rev. Lett.* **2009**, *102*, 106105.
- [189] Weng, Y.-X.; Wang, Y.-Q.; Asbury, J. B.; Ghosh, H. N.; Lian, T. *J. Phys. Chem. B* **1999**, *104*, 93–104.
- [190] Redmond, G.; Fitzmaurice, D. *J. Phys. Chem.* **1993**, *97*, 1426–1430.
- [191] Markussen, T.; Stadler, R.; Thygesen, K. S. *Nano Lett.* **2010**, *10*, 4260–4265.
- [192] Ricks, A. B.; Solomon, G. C.; Colvin, M. T.; Scott, A. M.; Chen, K.; Ratner, M. A.; Wasielewski, M. R. *J. Am. Chem. Soc.* **2010**, *132*, 15427–15434.
- [193] Haque, S. A.; Handa, S.; Peter, K.; Palomares, E.; Thelakkat, M.; Durrant, J. R. *Angew. Chem. Int. Ed.* **2005**, *44*, 5740–5744.
- [194] Maggio, E.; Martsinovich, N.; Troisi, A. *Angew. Chem. Int. Ed.* **2013**, *52*, 973–975.
- [195] Ardo, S.; Meyer, G. J. *Chem. Soc. Rev.* **2009**, *38*, 115–164.
- [196] Ning, Z.; Fu, Y.; Tian, H. *Energy Environ. Sci.* **2010**, *3*, 1170–1181.
- [197] Zeng, W.; Cao, Y.; Bai, Y.; Wang, Y.; Shi, Y.; Zhang, M.; Wang, F.; Pan, C.; Wang, P. *Chem. Mater.* **2010**, *22*, 1915–1925.
- [198] Albinsson, B.; Mårtensson, J. *J. Photochem. Photobiol. C* **2008**, *9*, 138–155.
- [199] Zeng, Y.; Zimmt, M. B. *J. Phys. Chem.* **1992**, *96*, 8395–8403.
- [200] Oliver, A. M.; Paddon-Row, M. N.; Kroon, J.; Verhoeven, J. W. *Chem. Phys. Lett.* **1992**, *191*, 371–377.
- [201] Baheti, A.; Lee, C.-P.; Thomas, K. R. J.; Ho, K.-C. *Phys. Chem. Chem. Phys.* **2011**, *13*, 17210–17221.
- [202] Zhang, X.-H.; Li, C.; Wang, W.-B.; Cheng, X.-X.; Wang, X.-S.; Zhang, B.-W. *J. Mater. Chem.* **2007**, *17*, 642–649.
- [203] Baheti, A.; Tyagi, P.; Thomas, K. R. J.; Hsu, Y.-C.; Lin, J. T. *J. Phys. Chem. C* **2009**, *113*, 8541–8547.
- [204] Solomon, G. C.; Herrmann, C.; Vura-Weis, J.; Wasielewski, M. R.; Ratner, M. A. *J. Am. Chem. Soc.* **2010**, *132*, 7887–7889.
- [205] Andrews, D. Q.; Solomon, G. C.; Van Duyne, R. P.; Ratner, M. A. *J. Am. Chem. Soc.* **2008**, *130*, 17309–17319.
- [206] Guedon, C. M.; Valkenier, H.; Markussen, T.; Thygesen, K. S.; Hummelen, J. C.; van der Molen, S. J. *Nat Nano* **2012**, *7*, 305–309.
- [207] Solomon, G. C.; Andrews, D. Q.; Van Duyne, R. P.; Ratner, M. A. *ChemPhysChem* **2009**, *10*, 257–264.
- [208] Kirczenow, E. G. E. and G. J. *Phys.: Condens. Matter* **1999**, *11*, 6911.
- [209] Aubry, S. *J. Phys.: Condens. Matter* **2007**, *19*, 255204.
- [210] Peter, L. *Acc. Chem. Res.* **2009**, *42*, 1839–1847.
- [211] Scholes, G. D. *ACS Nano* **2008**, *2*, 523–537.
- [212] Hendry, E.; Koeberg, M.; O'Regan, B.; Bonn, M. *Nano Lett.* **2006**, *6*, 755–759.
- [213] Galoppini, E.; Rochford, J.; Chen, H.; Saraf, G.; Lu, Y.; Hagfeldt, A.; Boschloo, G. *J. Phys. Chem. B* **2006**, *110*, 16159–16161.
- [214] Enache-Pommer, E.; Boercker, J. E.; Aydil, E. S. *Appl. Phys. Lett.* **2007**, *91*, 123113–123116.
- [215] Wang, H.; Peter, L. M. *J. Phys. Chem. C* **2009**, *113*, 18125–18133.

- [216] Zhao, J.; Pontius, N.; Winkelmann, A.; Sametoglu, V.; Kubo, A.; Borisov, A. G.; Nchez-Portal, D.; Silkin, V. M.; Chulkov, E. V.; Echenique, P. M.; Petek, H. *Phys. Rev. B* **2008**, *78*, 85419.
- [217] Rimbey, P. R. *Surf. Sci.* **1979**, *85*, 166–182.
- [218] Gippius, N. A.; Yablonskii, A. L.; Dzyubenko, A. B.; Tikhodeev, S. G.; Kulik, L. V.; Kulakovskii, V. D.; Forchel, A. *J. App. Phys.* **1998**, *83*, 5410–5417.
- [219] Dzyubenko, A. B.; Yablonskii, A. L. *Phys. Rev. B* **1996**, *53*, 16355.
- [220] Karwowski, J.; Stanke, M. *Struct. Chem.* **15**, 427–429.
- [221] Press, W. H.; Teukolsky, S. A.; Vetterling, W. T.; Flannery, B. P. *Numerical Recipes in FORTRAN 90*; second ed.; Cambridge University Press, 1997.
- [222] Kormann, C.; Bahnemann, D. W.; Hoffmann, M. R. *J. Phys. Chem.* **1988**, *92*, 5196–5201.
- [223] Enright, B.; Fitzmaurice, D. *J. Phys. Chem.* **1996**, *100*, 1027–1035.
- [224] Ritzoulis, G.; Papadopoulos, N.; Jannakoudakis, D. *J. Chem. Eng. Data* **1986**, *31*, 146–148.
- [225] Conway, B. E.; Bockris, J. O.; Ammar, I. A. *Trans. Faraday Soc.* **1951**, *47*, 756–766.
- [226] Von Hippel, A.; Kalnajs, J.; Westphal, W. B. *J. Phys. Chem. Solids* **1962**, *23*, 779–799.
- [227] Yim, C. M.; Pang, C. L.; Thornton, G. *Phys. Rev. Lett.* **2010**, *104*, 36806.
- [228] Varaganti, S.; Ramakrishna, G. *J. Phys. Chem. C* **2010**, *114*, 13917–13925.
- [229] Zhu, X. Y.; Yang, Q.; Muntwiler, M. *Acc. Chem. Res.* **2009**, *42*, 1779–1787.
- [230] Taddei, M. M.; et al. *Eur. J. Phys.* **2009**, *30*, 965.
- [231] Muljarov, E. A.; Tikhodeev, S. G.; Gippius, N. A.; Ishihara, T. *Phys. Rev. B* **1995**, *51*, 14370.
- [232] Sometani, T.; Hasebe, K. *Am. J. Phys.* **1977**, *45*, 918–921.
- [233] Sometani, T. *Eur. J. Phys.* **2000**, *21*, 549.
- [234] Yang, Q. X.; Muntwiler, M.; Zhu, X. Y. *Phys. Rev. B* **2009**, *80*, 115214.